FINITE ELEMENT METHODS AND MACHINE LEARNING FOR SOME MULTI-PHASE PROBLEMS

by
Qi Sun

A Dissertation submitted to the Department of Mathematics,

College of Natural Sciences and Mathematics

in partial fulfillment of the requirements for the degree of

Doctor of Philosophy
in Mathematics

Chair of Committee: Dr. Maxim A. Olshanskii

Committee Member: Dr. Annalisa Quaini

Committee Member: Dr. Tsorng-Whay Pan

Committee Member: Dr. Alexander Mamonov

Committee Member: Dr. Beatrice Riviere

University of Houston
May 2022

DEDICATION/EPIGRAPH

I'd like to express my deepest gratitude to my doctoral advisor Dr. Maxim Olshanskii and Dr. Annalisa Quaini. Not only did they teach me mathematics and how to approach problems, but how to be professional and work with others. They are always nice, patient, understanding, and supportive. It's an honor and pleasure to have a chance to study under them. I want to express my deepest gratitude and appreciation for their guidance, kindness, and encouragement.

I would like to express my special regards to my committee members – Dr. Tsorng-Whay Pan (UH), Dr. Alexander Mamonov(UH) and Dr. Beatrice Riviere (Rice). I would like to thank them for their time and feedback about my dissertation.

I want to thank Dr. Yuri Kuznetsov and Dr. Yuliya Gorb who taught me a lot at the beginning stage of my Ph.D. I want to thank Dr. Ilya Timofeyev, who gave me lots of wisdom and guidance for my personal life and my last research project.

I also want to thank my dear friend Dr. Vladimir Yushutin who shared his experiences and provided me with very useful advice and pranks. I want to thank my dear friends and colleagues Alexander Zhiliakov, Yan He, Kyle Williams, Yerbol Palzhanov, Ang Li, and many others who helped me and we had lots of fun for the past five wonderful years.

Qi Sun

January 19, 2022

ABSTRACT

This dissertation studies novel computational methodologies for multi-phase problems. The first part of the thesis focus on computational models for complex interface coupled flow problems. The problem is studied both numerically and analytically. More specifically, an unfitted finite element approach for the simulation of a two-phase flow with an immersed material viscous interface is studied in the first and second chapters. The interaction between the bulk and surface flows is characterized by no-penetration and slip with friction interface conditions. The system is shown to be dissipative and a model stationary problem is proved to be well-posed. The finite element method applied in this thesis belongs to a family of unfitted discretization. For the unfitted generalized Taylor–Hood finite element pair, an inf-sup stability property is shown with a stability constant that is independent of the viscosity ratio, slip coefficient, the position of the interface with respect to the background mesh and, of course, mesh size. In addition, we prove stability and optimal error estimates that follow from this inf-sup property. To study numerically the coupled problem, we introduce an iterative procedure based on the splitting of the system into bulk and surface problems. Numerical results in two and three dimensions to corroborate the theoretical findings and demonstrate the robustness of our approach.

Solving strongly-coupled nonlinear partial differential equations which characterize multi-scale, multi-physics processes with high dimensional chaotic dynamics is computationally expensive for many practical reasons. The necessity for developing a simulation and prediction strategy with high fidelity by only utilizing observational data highly increased over the last decades. In the second part of the thesis, the performance of two deep learning methods for reproducing short-term and long-term statistics of spatio-temporal data from the surface Cahn–Hilliard phase-field model is examined. The deep learning methods are echo state network (ESN) and long short-term memory (LSTM). The numerical discretization scheme of the Cahn-Hilliard system is briefly discussed. Then we present architectures of the ESN and the LSTM. We show that LSTM substantially outperforms ESN in short-term and long-term prediction, and give accurate forecasting trajectories for numerical solver's time steps.

This dissertation is based in part on the previously published articles listed below. I have permission from my co-authors/publishers to use the works listed below in my dissertation. Olshanskii, Maxim, Quaini, Annalisa and Sun, Qi. "An unfitted finite element method for two-phase Stokes problems with slip between phases" [75], Journal of Scientific Computing, V. 89 (2021), Article 41; Olshanskii, Maxim, Quaini, Annalisa and Sun, Qi. "A Finite Element Method for Two-Phase Flow with Material Viscous Interface" [76], Computational Methods in Applied Mathematics, vol. 22, no. 2, 2022, pp. 443-464.

TABLE OF CONTENTS

LIST OF FIGURES

1 Introduction

1.1 Motivation

Interfacial interactions between different gas, liquid, and solid phases are omnipresent phenomena in nature. Over the past decades, the necessity for a profound understanding of complex coupled flow problems has greatly increased. Nowadays, applications of fluid dynamics are everywhere in modern scientific fields such as geophysics, astrophysics, biology, and medicine.

For a long period of time, analysis of complex coupled flow problems largely based on laboratory experiments or prototyping. Thanks to rapid development of computer technology and increase in computing capacity over the years, developing computational models for complex physical phenomena has become an important topic in science and industry. The main advantage of computational simulation is allowing a rapid and convenient way for developing engineering products or scientific research. Due to the increasing complexity of multi-physics model, lab experiments on mutual interactions are often limited or even fail because of budget and lab constraints. Therefore computational approaches are in general regarded as superior and more effective.

Most of these complex physical phenomena can be characterized by coupled non-linear partial differential equations (PDEs) defined on complex geometries. Over the last century, numerical approximations to the solutions of coupled PDEs system have been proposed such as finite difference method, spectral method, finite volume method, finite elements method, or even machine learning, among which finite elements method (FEM) is one of the most powerful and popular approach. Its ability to simulate single-phase and multi-phase problems has been demonstrated by researchers. Nowadays due to the need from industrial development, the complexity of configurations of multi-physics model has been rapidly increasing, gradually pushing to the limit of FEM's capabilities. One of the limitations of FEMs is to deal with large deformations and topological changes of domains. Several approaches have been proposed in the last decades to address this shortcoming of FEM. One of them is so-called geometrically unfitted finite element methods, a class of powerful

discretization techniques that chooses computational domains unfitted to physical domains. Popular unfitted methods are XFEM [71] and CutFEM [15]. XFEM enriches the finite element shape functions by the Partition-of-Unity method. To learn more about XFEM applied to two-phase flow problems, we refer the reader to [21, 29, 36, 55, 91]. CutFEM is a variation of XFEM, also called Nitsche-XFEM [41]. CutFEM uses overlapping fictitious domains in combination with ghost penalty stabilization [14] to enrich and stabilize the solution. The name of the method "Cut Finite Element Method" (CutFEM) is given by the fact that finite elements are cut by the physical boundary.

Another challenge for FEMs is to generate a computationally efficient and accurate numerical approximation to solutions of surface PDEs defined on a complex evolving surface. The computational cost of triangulation or another type of fitting mesh for complex evolving surfaces can be high. To overcome this limitation, TraceFEM [79] was proposed that uses a surface-independent background mesh on a fixed bulk domain, such that the fixed bulk domain contains the evolving surface. The main idea of the method is to introduce a finite element space base on a volume triangulation and consider traces of finite element function from the finite element space. This trace space is used to formulate the finite element discretization for the PDE system.

The application of CutFEM and TraceFEM discretization for a coupled flow model constitutes the major part of the thesis. In the last chpater, we explore the applicability of artificial neural networks in prediction of the pattern formation driven by the Cahn-Hilliard model of phase separation.

1.2 Basic equations of fluid dynamics

1.2.1 Governing equations for one phase flow

In this section, we derive the governing equations for the motion of a laminar flow of incompressible fluid. Let $\Omega \in \mathbb{R}^d, d \in \{2, 3\}$ be a region occupied by fluid. The derivation of the equations is based on several fundamental assumptions:

- For all times $t > 0$, there exists a well-defined mass density function $\rho(\mathbf{x}, t)$ such that the total mass is defined as $m(t) := \int_\Omega \rho(\mathbf{x}, t)\ dV$ (Hypothesis of continuum).
- For all times $t > 0$, mass is neither produced nor disappears (Conservation of mass).
- For all times $t > 0$, energy is neither produced nor disappears (Conservation of energy).
- The rate of change of momentum of an object is directly proportional to the force applied (Conservation of momentum).

To derive the governing equations, we consider $\mathbf{x} \in \Omega$, where $\mathbf{x} = (x_1, x_2, x_3)$ is a point in Ω represented in Eulerian coordinates. Let X denote a fluid particle (material point) moving through $\mathbf{x}$ at time t. We describe the change of the particle position as a function $\phi : \Omega \times \mathbb{R}^+ \to \mathbb{R}^3$, where $\phi(X, t)$ can be interpreted as position of particle X at given time t.
We define the velocity of fluid particle X at time t,

$$\mathbf{u}(\mathbf{x}, t) := \frac{\partial \phi}{\partial t}(X, t) \qquad \textit{where } \mathbf{x} := \phi(X, t). \tag{1}$$

The acceleration can be derived as

$$\begin{aligned}
\mathbf{a}(\mathbf{x}, t) := \frac{d}{dt}\mathbf{u}(x, t) &= \frac{d}{dt}\mathbf{u}(\phi(X, t), t) && (2)\\
&= \frac{\partial}{\partial t}\mathbf{u}(\phi(X, t), t) + \sum_{i=1}^{3} \frac{\partial \mathbf{u}}{\partial x_i}(\phi(X, t), t)\frac{\partial \phi_i}{\partial t}(X, t) && (3)\\
&= \frac{\partial}{\partial t}\mathbf{u}(\phi(X, t), t) + \sum_{i=1}^{3} u_i(X, t)\frac{\partial \mathbf{u}}{\partial x_i}(\phi(X, t), t) && (4)\\
&= \frac{\partial \mathbf{u}}{\partial t} + (\mathbf{u} \cdot \nabla)\mathbf{u}. && (5)
\end{aligned}$$

Now we are ready to derive the governing equations for one phase flow from our assumptions. We start with conservation of mass and hypothesis of continuum.
Consider a subdomain $W \subset \Omega$, denote the boundary of W as ∂W and $\mathbf{n}$ as the unit outer normal. For the sake of simplicity, we assumed that $\rho(\mathbf{x}, t) \in C^1(\Omega)$, and W is a Lipschitz domain. The

change of mass in W can be derived as,

$$\frac{d}{dt}m(W,t) = \frac{d}{dt}\int_W \rho(\mathbf{x},t)\ dV \tag{6}$$

$$= \int_W \frac{\partial}{\partial t}\rho(\mathbf{x},t)\ dV. \tag{7}$$

The total flow of mass through boundary ∂W can be characterized by,

$$\int_{\partial W} \rho\mathbf{u}\cdot\mathbf{n}\ dA. \tag{8}$$

Following from the principle of conservation of mass, the change of mass in domain W is equals to the flow of mass over boundary ∂W into W, i.e.,

$$\int_W \frac{\partial}{\partial t}\rho(\mathbf{x},t)\ dV = -\int_{\partial W} \rho\mathbf{u}\cdot\mathbf{n}\ dA. \tag{9}$$

We rewrite (9) as,

$$\int_\Omega (\frac{\partial}{\partial t}\rho(\mathbf{x},t) + div(\rho\mathbf{u}))\mathbf{1}_W\ dV = 0 \qquad \text{for every } W \subset \Omega, \tag{10}$$

where $\mathbf{1}_W$ denotes an indicator function for the set W and since (10) holds for arbitrary t, we obtain the following equality,

$$\frac{\partial}{\partial t}\rho(\mathbf{x},t) + div(\rho\mathbf{u}) = 0 \text{ in } \Omega\times(0,T). \tag{11}$$

In fluid mechanics, compressibility is defined as a measure of the relative volume change of a fluid as a response to mean stress change. Here we give a definition of an incompressible fluid: a fluid is

incompressible if the following conditions hold,

$$div\ \mathbf{u} = 0 \tag{12}$$

$$\dot{\rho} = 0. \tag{13}$$

To derive equalities from the conservation of momentum assumption, we need the Reynold's transport theorem.

We derive the theorem in Eulerian coordinates. Consider a small subdomain $W_0 \subset \Omega$ (the so-called material volume). We define $W_t := \{\phi(X,t) : X \in W_0\}$. Let $\mathbf{f} : W_t \times (0,T) \to \mathbb{R}^3$ be a sufficiently smooth function. The following equality holds,

$$\frac{d}{dt}\int_{W_t} \mathbf{f}(\mathbf{x},t)\ dV = \int_{W_t} (\dot{\mathbf{f}} + \mathbf{f} div\ \mathbf{u})\ dV = \int_{W_t} \frac{\partial \mathbf{f}}{\partial t} dV + \int_{\partial W_t} (\mathbf{u}\cdot\mathbf{n})\mathbf{f}\ dA \tag{14}$$

where $\dot{\mathbf{f}} := \frac{\partial \mathbf{f}}{\partial t} + \mathbf{u}\cdot\nabla\mathbf{f}$ is so-called material derivative.

Now we are ready to derive equalities from the assumption of conservation of momentum. Recall Newton's second law: "The rate of change in momentum of an object is directly proportional to the applied force".

We first distinguish the force applied to the fluid into two categories:

Volume forces:

$$\int_{W_t} \rho(\mathbf{x},t)\mathbf{f}(\mathbf{x},t)\ dV, \tag{15}$$

with a given force density $\mathbf{f} = (f_1, f_2, f_3)$.

Surface forces:

$$\int_{\partial W_t} \mathbf{n}\cdot\boldsymbol{\sigma}(\mathbf{x},t)\ dA \tag{16}$$

where $\boldsymbol{\sigma} \in \mathbb{R}^{3\times 3}$ is the stress tensor describing internal friction and pressure. $\mathbf{n}\cdot\boldsymbol{\sigma}$ is a vector field which characterize stress vector on hyper-surface ∂W_t. Hence we could rephrase the conservation of momentum,

$$\frac{d}{dt}\int_{W_t}\rho\mathbf{u}\ dV = \int_{W_t}\rho\mathbf{f}\ dV + \int_{\partial W_t}\mathbf{n}\cdot\boldsymbol{\sigma}\ dA \tag{17}$$

$$= \int_{W_t}\rho\mathbf{f}\ dV + \int_{W_t} div\ \boldsymbol{\sigma}\ dV. \tag{18}$$

Combining (14) and (18) we have,

$$\int_{W_t}\rho\dot{\mathbf{u}} - \rho\mathbf{f} - div\boldsymbol{\sigma}\ dV = 0 \text{ for every } W_t \subset \Omega. \tag{19}$$

Since (19) is true for all $W_t \subset \Omega$, one has

$$\rho\dot{\mathbf{u}} = \rho\mathbf{f} + div\boldsymbol{\sigma} \tag{20}$$

or in a equivalent form,

$$\rho\frac{\partial\mathbf{u}}{\partial t} + \rho(\mathbf{u}\cdot\nabla)\mathbf{u} = \rho\mathbf{f} + div\boldsymbol{\sigma}. \tag{21}$$

We get the so-called Cauchy momentum equation.

1.2.2 Constitutive law between stress tensor and the rate of deformation tensor

In the section we give detailed definition of the stress tensor $\boldsymbol{\sigma}$. The stress tensor in Eulerian coordinates can be represented as matrix form at each position:

$$\boldsymbol{\sigma}(\mathbf{x},t) = \begin{bmatrix} \sigma_{xx} & \sigma_{xy} & \sigma_{xz} \\ \sigma_{yx} & \sigma_{yy} & \sigma_{yz} \\ \sigma_{zx} & \sigma_{zy} & \sigma_{zz} \end{bmatrix} \in \mathbb{R}^{3\times 3} \qquad \text{for } \mathbf{x}\in\Omega, t\in(0,T). \tag{22}$$

For viscous Newtonian fluid, one makes the following assumptions:

- $\boldsymbol{\sigma} = -p\mathbf{I} + \tau$, where p denotes a scalar field on Ω characterizing pressure.
- $\boldsymbol{\sigma}$ linearly dependends on $\nabla\mathbf{u}$.
- $\boldsymbol{\sigma}$ is invariant with respect to translation and rotation.
- $\boldsymbol{\sigma}$ is symmetirc.

From the previous assumptions, one can conclude that the stress tensor of the Newtonian fluid takes the following form,

$$\boldsymbol{\sigma} = -p\mathbf{I} + \lambda(\nabla \cdot \mathbf{u})\mathbf{I} + 2\mu\mathbf{D}(\mathbf{u}) \tag{23}$$

where $\mathbf{D}(\mathbf{u}) := \frac{1}{2}(\nabla\mathbf{u} + \nabla\mathbf{u}^T)$ denotes the deformation tensor. In the case of incompressible fluid, one can further simplify,

$$\boldsymbol{\sigma} = -p\mathbf{I} + 2\mu\mathbf{D}(\mathbf{u}) \tag{24}$$

Combining (12) (21), and (24), we get the well-known Navier-Stokes equations for incompressible flow:

$$\begin{cases} \frac{\partial\rho\mathbf{u}}{\partial t} + \rho(\mathbf{u}\cdot\nabla)\mathbf{u} = \rho\mathbf{f} + \nabla\cdot\boldsymbol{\sigma} \\ \nabla\cdot\mathbf{u} = 0 \end{cases} \tag{25}$$

1.2.3 Navier-Stokes equations for two phase flow

Now we introduce the Navier-Stokes equations for two phase flow. Let $\Omega \subset \mathbb{R}^d$ be a given domain, $d = 2$ or $d = 3$, $\partial\Omega$ at least Lipschitz smooth. Consider a time dependent at least C^2 smooth closed hyper-surface $(\Gamma(t))_{t\in[0,T]}$ separating $\Omega = \Omega_\pm$ into two subdomains, $\Omega_+(t)$ and $\Omega_-(t) := \Omega \setminus \overline{\Omega}_+(t)$. It is assumed that $(\Gamma(t))_{t\in[0,T]}$ is a C^2 smooth hypersurface without boundary that evolves with a time-dependent vector field $\mathcal{V}(t)$. Let $\mathbf{n}$ denote the unit normal on $\Gamma(t)$ pointing towards $\Omega_+(t)$, see Fig.1.

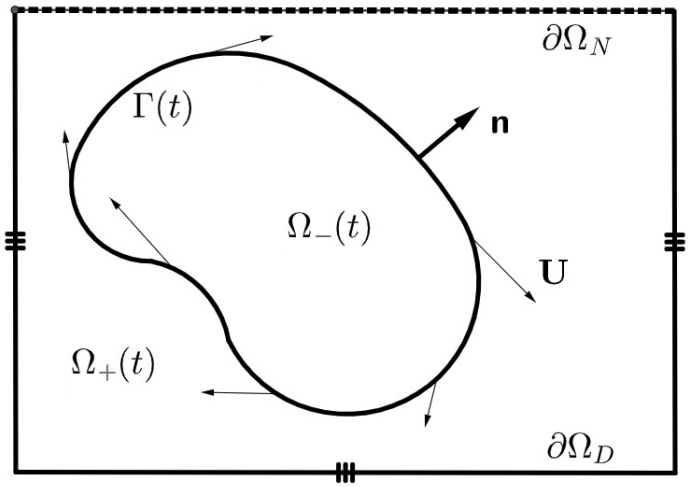

Figure 1: An illustration for the geometrical setup of the 2D problem.

For any vector field $\mathbf{u}$ on Γ we define the normal and tangential components, correspondingly:

$$u_N := \mathbf{u} \cdot \mathbf{n}\,, \qquad \mathbf{u}_T := \mathbf{P}\mathbf{u} = \mathbf{u} - u_N \mathbf{n} \tag{26}$$

where $\mathbf{P} = \mathbf{I} - \mathbf{n}^T\mathbf{n}$ is the projector on the tangent space $T\Gamma(t)$. Let $\mathbf{u} : \Omega_\pm \times [0,T] \to \mathbb{R}^d$ and $p : \Omega_\pm \times [0,T] \to \mathbb{R}$ be the bulk fluid velocity and the pressure. The restrictions $\mathbf{u}^+, p^+$ and $\mathbf{u}^-, p^-$ are assumed to be C^1 and define bulk flows of separate phases correspondingly in Ω_+ and Ω_-. We let

$$[\mathbf{u}]_+^- := \mathbf{u}^- - \mathbf{u}^+$$

denote the jump of bulk velocity; similar notation is used for jumps of other quantities.

The incompressible Navier-Stokes system for both phases with a prescribed velocity on $\partial\Omega_D$

and presribed stresses on $\partial\Omega_N$ such that $\partial\Omega_+ = \partial\Omega_D \cup \partial\Omega_N \cup \Gamma(t)$ reads

$$\rho\,\dot{\mathbf{u}} = \operatorname{div}\boldsymbol{\sigma} \qquad \text{in } \Omega_\pm(t) \tag{27}$$

$$\nabla\cdot\mathbf{u} = 0 \qquad \text{in } \Omega_\pm(t) \tag{28}$$

$$\mathbf{u} = \mathbf{g} \qquad \text{on } \partial\Omega_D \tag{29}$$

$$\mathbf{t} = \mathbf{f} \qquad \text{on } \partial\Omega_N \tag{30}$$

where $\dot{\mathbf{u}} = \mathbf{u}_t + (\nabla\mathbf{u})\mathbf{u}$ is the material derivative, $\boldsymbol{\sigma} = -p\,I + \mu(\nabla\mathbf{u} + \nabla^T\mathbf{u})$ is the Newtonian stress tensor, $\rho := \rho^- H + \rho^+(1-H)$ with H the indicator function of Ω_-; the constant densities $\rho^\pm$ and the dynamic viscosity $\mu = \mu^\pm$ are material parameters of the phases, and $\mathbf{t} = \mathbf{t}(\mathbf{u}) = \boldsymbol{\sigma}\tilde{\mathbf{n}}$ is the stress vector on $\partial\Omega$ oriented by outward pointing $\tilde{\mathbf{n}}$. The classical interface conditions on a moving interface:

AI *Continuous coupling*

$$[\mathbf{u}]_+^- = 0 \qquad \text{on } \Gamma(t) \tag{31}$$

$$[\boldsymbol{\sigma}]_+^-\mathbf{n} = 0 \qquad \text{on } \Gamma(t) \tag{32}$$

AII *Friction with slip*

$$[\mathbf{u}]_+^-\cdot\mathbf{n} = 0 \qquad \text{on } \Gamma(t) \tag{33}$$

$$\mathbf{P}\boldsymbol{\sigma}^-\mathbf{n} = -f(\mathbf{P}\mathbf{u}^- - \mathbf{P}\mathbf{u}^+) \qquad \text{on } \Gamma(t) \tag{34}$$

$$\mathbf{P}\boldsymbol{\sigma}^+\mathbf{n} = f(\mathbf{P}\mathbf{u}^+ - \mathbf{P}\mathbf{u}^-) \qquad \text{on } \Gamma(t) \tag{35}$$

$$\mathbf{n}\cdot[\boldsymbol{\sigma}]_+^-\mathbf{n} = 0 \qquad \text{on } \Gamma(t) \tag{36}$$

where f is the friction coefficient. Note that in both cases the stress vector is continuous across the interface $\Gamma(t)$, $[\boldsymbol{\sigma}]_+^-\mathbf{n} = 0$, which is the well-known in continuum mechanics condition of local conservation of the momentum flux. The geometrical evolution of the interface $\Gamma(t)$ between domains

is coupled with the material velocities on $\Omega_+(t)$ and $\Omega_-(t)$:

$$\mathcal{V} \cdot \mathbf{n} = \mathbf{u}^+ \cdot \mathbf{n} = \mathbf{u}^- \cdot \mathbf{n} \qquad \text{on } \Gamma(t) \tag{37}$$

1.2.4 Surface Navier-Stokes equations

To formulate the surface Navier-Stokes equations, we need to define additional notations. The evolution of the material interface can be described in terms of the velocity of this surface fluid denoted by $\mathbf{U}$. Later, we will need the decomposition of $\mathbf{U}$ into tangential and normal components: $\mathbf{U} = \mathbf{U}_T + U_N\mathbf{n}$, with $\mathbf{U}_T \cdot \mathbf{n} = 0$, $U_N = \mathbf{n} \cdot \mathbf{U}$. The surface Navier-Stokes equations governing the motion of a fluidic deformable layer appear in several works [90, 51, 68]. Here, we adopt the formulation in terms of tangential differential operators from [51], where the equations have been derived from conservation principles. Let $\mathbf{P}(\mathbf{x}) := \mathbf{I} - \mathbf{n}(\mathbf{x})\mathbf{n}(\mathbf{x})^T$ for $\mathbf{x} \in \Gamma$ be the orthogonal projection onto the tangent plane. For a scalar function $\pi : \Gamma \to \mathbb{R}$ or a vector function $\mathbf{U} : \Gamma \to \mathbb{R}^3$ we define $\pi^e : \mathcal{O}(\Gamma) \to \mathbb{R}$, $\mathbf{U}^e : \mathcal{O}(\Gamma) \to \mathbb{R}^3$, smooth extensions of π and $\mathbf{U}$ from Γ to its neighborhood $\mathcal{O}(\Gamma)$. The surface gradient and covariant derivatives on Γ are then defined as $\nabla_\Gamma \pi = \mathbf{P}\nabla\pi^e$ and $\nabla_\Gamma \mathbf{U} := \mathbf{P}\nabla\mathbf{U}^e\mathbf{P}$. The definitions of $\nabla_\Gamma\pi$ and $\nabla_\Gamma\mathbf{U}$ are independent of the particular smooth extension of π and $\mathbf{U}$ off Γ. On Γ, we consider the surface rate-of-strain tensor [38] given by

$$\mathbf{D}_\Gamma(\mathbf{U}) := \frac{1}{2}\mathbf{P}(\nabla\mathbf{U} + (\nabla\mathbf{U})^T)\mathbf{P} = \frac{1}{2}(\nabla_\Gamma\mathbf{U} + (\nabla_\Gamma\mathbf{U})^T). \tag{38}$$

The surface divergence for a vector $\mathbf{g} : \Gamma \to \mathbb{R}^3$ and a tensor $\mathbf{A} : \Gamma \to \mathbb{R}^{3\times 3}$ are defined as: $\operatorname{div}_\Gamma \mathbf{g} := \operatorname{tr}(\nabla_\Gamma \mathbf{g})$, $\operatorname{div}_\Gamma \mathbf{A} := \left(\operatorname{div}_\Gamma(\mathbf{e}_1^T\mathbf{A}),\ \operatorname{div}_\Gamma(\mathbf{e}_2^T\mathbf{A}),\ \operatorname{div}_\Gamma(\mathbf{e}_3^T\mathbf{A})\right)^T$,where $\mathbf{e}_i$ is the ith standard basis vector.

Before deriving the surface Navier-Stokes equations, let us recall the surface integration by parts identity, and surface analogue of the Reynolds transport theorem.

Consider $f \in H^1(\Gamma(t))$ with $t \in [0, T]$ and vector field $\mathbf{v}$. For arbitrary $\gamma(t) \subset \Gamma(t)$, the following

integration by parts identity holds:

$$\int_{\gamma(t)} f \operatorname{div}_\Gamma \mathbf{v} \; ds = \int_{\partial\gamma(t)} f\mathbf{v}\cdot\mathbf{m} \; d\gamma - \int_{\gamma(t)} \mathbf{v}\cdot\nabla_\Gamma f \; ds + \int_{\gamma(t)} \kappa f \mathbf{v}\cdot\mathbf{n} \; ds \tag{39}$$

where κ is the sum of principle curvatures, and $\mathbf{m} \in T\Gamma(t)$ is the outward normal defined on $\partial\gamma(t)$. Let $\gamma(t) \subset \Gamma(t)$ be a subdomain follows the evolving principle (37), then the following analogue of Reynold transport theorem on $\gamma(t)$ holds,

$$\frac{d}{dt}\int_{\gamma(t)} f \; ds = \int_{\gamma(t)} (\dot{f} + f \operatorname{div}_\Gamma \mathbf{u}) \; ds \tag{40}$$

with $\dot{f}$ is the material derivative of f. Now we are ready to derive the surface Navier-Stokes equations. The derivation is based on conservation laws of mass and momentum.

We assume that the surface $\Gamma(t)$ is inextensible i.e. for arbitrary material subdomain $\gamma(t) \subset \Gamma(t)$, the following equality holds,

$$\frac{d}{dt}\int_{\gamma(t)} dA = 0 \qquad \text{for all } t \in [0,T] \tag{41}$$

The surface Reynolds transport theorem and the arbitrariness of $\gamma(t)$ yields,

$$\operatorname{div}_\Gamma \mathbf{U} = 0 \tag{42}$$

Conservation of mass yields,

$$0 = \frac{d}{dt}\int_{\gamma(t)} \rho_\Gamma \; dA = \int_{\gamma(t)} \dot{\rho}_\Gamma \; dA \tag{43}$$

The second equality follows from (40), and $\operatorname{div}_\Gamma \mathbf{U} = 0$. The arbitrariness of $\gamma(t)$ and (43) imply $\dot{\rho}_\Gamma = 0$. We further assume ρ_Γ is constant on evolving surface $\Gamma(t)$.

From conservation of surface momentum, we have the equation,

$$\frac{d}{dt}\int_{\gamma(t)} \rho_\Gamma \mathbf{U}\ dA = \int_{\gamma(t)} \mathbf{b}\ dA + \int_{\partial\gamma(t)} \mathbf{b_m}\ ds \tag{44}$$

with an area force $\mathbf{b}$, and a contact force $\mathbf{b_m}$. We use Cauchy ansatz and Boussinesq-Scriven ansatz for the contact force term, i.e.

$$\mathbf{b_m} = \boldsymbol{\sigma}_\Gamma \mathbf{m}, \qquad \boldsymbol{\sigma}_\Gamma = -\pi \mathbf{P} + 2\mu_\Gamma D_\Gamma(\mathbf{U}) \tag{45}$$

with a stress tensor $\boldsymbol{\sigma}_\Gamma$ and $\mathbf{m}$ the in-plane unit normal on $\partial\gamma(t)$. Using the Stokes theorem, we obtain the momentum balance,

$$\frac{d}{dt}\int_{\gamma(t)} \rho_\Gamma \mathbf{U}\ dA = \int_{\gamma(t)} \mathrm{div}_\Gamma \boldsymbol{\sigma}_\Gamma + \mathbf{b}\ dA \tag{46}$$

Combining (42), (46), (40), and arbitrariness. One obtains the surface Navier-Stokes system:

$$\rho_\Gamma \dot{\mathbf{U}} = \mathrm{div}_\Gamma \boldsymbol{\sigma}_\Gamma + \mathbf{b} \qquad \text{on } \Gamma(t) \tag{47}$$

$$\mathrm{div}_\Gamma \mathbf{U} = 0 \qquad \text{on } \Gamma(t) \tag{48}$$

$$\boldsymbol{\sigma}_\Gamma = -\pi \mathbf{P} + 2\mu_\Gamma D_\Gamma(\mathbf{U}) \qquad \text{on } \Gamma(t) \tag{49}$$

It is natural to link the geometrical evolution of the bulk interface with the velocity $\mathbf{U}$ of the surface system that occupies it:

$$\mathcal{V} \cdot \mathbf{n} = U_N \qquad \text{on } \Gamma(t) \tag{50}$$

To derive the surface energy balance laws, we need the following lemma,

Lemma 1.1 *For a vector* $\mathbf{g} \in (C^1(\Gamma))^d$ *and a matrix* $\mathbf{G} \in (C^1(\Gamma))^{d\times d}$ *such that* $\mathbf{G} = \mathbf{PG}$ *we have*

$$\int_\Gamma \mathbf{g} \cdot \operatorname{div}_\Gamma \mathbf{GP}\, dS = -\int_\Gamma \mathbf{G} : \nabla_\Gamma \mathbf{g}\, dS \tag{51}$$

Proof:

In order to prove the lemma we need 3 steps.

Step 1:

For an arbitrary $g \in C^1(\Gamma)$ and for all $i \in [1, d]$ consider

$$\int_\Gamma (\nabla_\Gamma^T g)_i\, dS = \int_\Gamma (\mathbf{P}\nabla_\Gamma^T g)_i\, dS = \int_\Gamma \nabla_\Gamma(\mathbf{id}_i) \cdot \nabla_\Gamma^T g\, dS = -\int_\Gamma g \triangle_\Gamma \mathbf{id}_i\, dS = \int_\Gamma g\kappa \mathbf{n}_i\, dS$$

where we used the integration by parts for scalar functions on a surface without boundary.

Step 2:

For an arbitrary $\mathbf{f} \in C^1(\Gamma)^d$ such that $\mathbf{f} = \mathbf{Pf}$ we replace g with $\mathbf{f}_i\, g$ and sum for all $i \in [1, d]$:

$$\int_\Gamma g \operatorname{div}_\Gamma \mathbf{f} + \mathbf{f} \cdot (\nabla_\Gamma^T g)\, dS = \int_\Gamma \kappa g \mathbf{f} \cdot \mathbf{n}\, dS$$

which implies

$$\int_\Gamma g \operatorname{div}_\Gamma \mathbf{f}\, dS = -\int_\Gamma \mathbf{f} \cdot \nabla_\Gamma^T g dS \tag{52}$$

Step 3:

We let $\mathbf{G}_i$ denote the i-th row of matrix $\mathbf{G}$ and

$$\int_\Gamma \mathbf{g} \cdot \operatorname{div}_\Gamma \mathbf{GP}\, dS = \sum_{i=1}^3 \int_\Gamma g_i \operatorname{div}_\Gamma (\mathbf{e}_i^T \mathbf{GP})^T\, dS = \sum_{i=1}^3 \int_\Gamma g_i \operatorname{div}_\Gamma (\mathbf{PG}_i^T)\, dS = -\sum_{i=1}^3 \int_\Gamma \mathbf{PG}_i^T \cdot \nabla_\Gamma^T g_i\, dS$$
$$= -\sum_{i=1}^3 \int_\Gamma \nabla_\Gamma g_i \mathbf{PG}_i^T\, dS = -\sum_{i=1}^3 \int_\Gamma \nabla g_i \mathbf{PG}_i^T\, dS = -\int_\Gamma \operatorname{tr}(\nabla \mathbf{g} \mathbf{PG}^T)\, dS$$
$$= -\int_\Gamma \operatorname{tr}(\nabla \mathbf{g} \mathbf{PG}^T \mathbf{P})\, dS = -\int_\Gamma \operatorname{tr}(\mathbf{P}\nabla \mathbf{g} \mathbf{PG}^T)\, dS = -\int_\Gamma \operatorname{tr}(\nabla_\Gamma \mathbf{g} \mathbf{G}^T)\, dS = -\int_\Gamma \mathbf{G} : \nabla_\Gamma \mathbf{g}\, dS$$

Now we are ready to show the balance laws for the kinetic energy E_Γ of a fluidic interface with the help of (51):

$$\frac{d}{dt}E_\Gamma = \frac{1}{2}\frac{d}{dt}\int_{\Gamma(t)}\rho_\Gamma(\mathbf{U}\cdot\mathbf{U})\,dS = \frac{1}{2}\int_{\Gamma(t)}\left(2\rho_\Gamma\mathbf{U}\cdot\dot{\mathbf{U}} + \rho_\Gamma(\mathbf{U}\cdot\mathbf{U})\,\mathrm{div}_\Gamma\mathbf{U}\right)\,dS$$
$$= \int_{\Gamma(t)}\rho_\Gamma\mathbf{U}\cdot\dot{\mathbf{U}}\,dS = \int_{\Gamma(t)}\mathbf{U}\cdot(\,\mathrm{div}_\Gamma\boldsymbol{\sigma}_\Gamma + \mathbf{b})\,dS = \int_{\Gamma(t)}\mathbf{U}\cdot\mathbf{b}\,dS - \int_{\Gamma(t)}\mathrm{tr}(\boldsymbol{\sigma}_\Gamma\nabla_\Gamma\mathbf{U})\,dS$$
$$= \int_{\Gamma(t)}\mathbf{U}\cdot\mathbf{b}\,dS - 2\mu_\Gamma\int_{\Gamma(t)}\|D_\Gamma\mathbf{U}\|^2\,dS \tag{53}$$

where we clearly see the total external force, the total viscous dissipation of the fluidic interface.

1.2.5 Surface Navier-Stokes on a stationary interface

Here we would like to understand under which conditions the Bousinesque-Scriven model (47)-(49) can be used to model a stationary in space fluidic interface. We start by splitting the surface Navier-Stokes system into normal and tangential parts (see e.g. in [51]):

$$\rho_\Gamma\mathbf{P}\dot{\mathbf{U}}_T = -\nabla_\Gamma^T\pi + 2\mu_\Gamma P\,\mathrm{div}_\Gamma D_\Gamma(\mathbf{U}) + b_T - \rho_\Gamma U_N\dot{\mathbf{n}} \qquad \text{on } \Gamma(t) \tag{54}$$

$$\rho_\Gamma\dot{U}_N = 2\mu_\Gamma\mathbf{n}\cdot\,\mathrm{div}_\Gamma D_\Gamma(\mathbf{U}) + \pi\kappa + b_N + \rho_\Gamma\dot{\mathbf{n}}\cdot\mathbf{U}_T \qquad \text{on } \Gamma(t) \tag{55}$$

$$\mathrm{div}_\Gamma\mathbf{U} = 0 \qquad \text{on } \Gamma(t) \tag{56}$$

Let us consider surface Euler equations assuming $\mu_\Gamma = 0$ and demonstrate how momentum and energy split in the normal and tangential directions. Taking inner product of the first (54) and the second (55) equations with $\mathbf{U}_T$ and U_N correspondingly we arrive at the energy law:

$$\int_{\Gamma(t)}\rho_\Gamma\left(\dot{\mathbf{U}}_T\cdot\mathbf{U}_T + \dot{U}_N U_N\right)\,dS = \int_{\Gamma(t)}(\mathbf{U}\cdot\mathbf{b} + U_N\pi\kappa - \mathbf{U}_T\cdot\nabla_\Gamma^T\pi)\,dS$$
$$= \int_{\Gamma(t)}\mathbf{U}\cdot\mathbf{b}\,dS + \int_{\Gamma(t)}\pi(U_N\kappa + \,\mathrm{div}_\Gamma\mathbf{U}_T)\,dS = \int_{\Gamma(t)}\mathbf{U}\cdot\mathbf{b}\,dS$$

Since

$$\dot{\mathbf{U}} \cdot \mathbf{U} = (\dot{\mathbf{U}}_T + \dot{U}_N \mathbf{n} + U_N \dot{\mathbf{n}}) \cdot (\mathbf{U}_T + U_N \mathbf{n}) = \dot{\mathbf{U}}_T \cdot \mathbf{U}_T + \dot{U}_N \cdot U_N$$
$$+ U_N (\dot{\mathbf{U}}_T \cdot \mathbf{n} + \mathbf{U}_T \cdot \dot{\mathbf{n}}) = \dot{\mathbf{U}}_T \cdot \mathbf{U}_T + \dot{U}_N \cdot U_N$$

we obtain the splitting of the surface energy balance law

$$\frac{dE_\Gamma}{dt} = \frac{1}{2}\frac{d}{dt}\int_{\Gamma(t)} \rho_\Gamma \mathbf{U}^2 \, dS = \frac{1}{2}\frac{d}{dt}\int_{\Gamma(t)} \rho_\Gamma \left(\mathbf{U}_T^2 + U_N^2\right) \, dS = \int_{\Gamma(t)} \mathbf{U} \cdot \mathbf{b} \, dS$$

Now we integrate the first and the second equations assuming $\mu_\Gamma = 0$ to obtain the directional split of the momentum law:

$$\int_{\Gamma(t)} \rho_\Gamma \left(\mathbf{P}\dot{\mathbf{U}}_T + \dot{U}_N \mathbf{n}\right) \, dS = \int_{\Gamma(t)} (\mathbf{b} + \pi\kappa\mathbf{n} - \nabla_\Gamma^T \pi - \rho_\Gamma U_N \dot{\mathbf{n}} + \rho_\Gamma (\dot{\mathbf{n}} \cdot \mathbf{U}_T)\mathbf{n}) \, dS$$
$$= \int_{\Gamma(t)} \mathbf{b} \, dS - \int_{\Gamma(t)} \rho_\Gamma (U_N \dot{\mathbf{n}} + (\mathbf{n} \cdot \dot{\mathbf{U}}_T)\mathbf{n}) \, dS$$

where $\dot{\mathbf{n}} \cdot \mathbf{U}_T = -\mathbf{n} \cdot \dot{\mathbf{U}}_T$ is used. Noticing $\dot{\mathbf{P}}\mathbf{U}_T + \mathbf{P}\dot{\mathbf{U}}_T = \dot{\mathbf{U}}_T$ and using

$$\dot{\mathbf{U}} = \dot{\mathbf{U}}_T + \dot{U}_N \mathbf{n} + U_N \dot{\mathbf{n}} = \mathbf{P}\dot{\mathbf{U}}_T + \dot{\mathbf{P}}\mathbf{U}_T + \dot{U}_N \mathbf{n} + U_N \dot{\mathbf{n}} \tag{57}$$

we conclude that a part of the momentum balance is the change of velocity on the surface and another part is due to the geometrical evolution:

$$\frac{dQ_\Gamma}{dt} = \int_{\Gamma(t)} \rho_\Gamma \left(\mathbf{P}\dot{\mathbf{U}}_T + \dot{U}_N \mathbf{n}\right) \, dS + \int_{\Gamma(t)} \rho_\Gamma (U_N \dot{\mathbf{n}} + \dot{\mathbf{P}}\mathbf{U}_T) \, dS = \int_{\Gamma(t)} \mathbf{b} \, dS \tag{58}$$

It is easy to see that the last statement also holds in case of $\mu_\Gamma \neq 0$.

Now we derive a model of a fluidic interface that corresponds to a stationary surface in space, i.e. $U_N = 0$. Unfortunately, a naive insertion of this condition into the surface Navier-Stokes does

not lead to a consistent system. Indeed, set $U_N = 0$ and have

$$\rho_\Gamma \mathbf{P}\dot{\mathbf{U}}_T = -\nabla_\Gamma^T \pi + 2\mu_\Gamma \mathbf{P}\,\mathrm{div}_\Gamma D_\Gamma(\mathbf{U}_T) + \mathbf{b}_T \qquad \text{on } \Gamma(t) \tag{59}$$

$$0 = -2\mu \mathrm{tr}(H\nabla_\Gamma \mathbf{U}_T) + \pi\kappa + b_N + \rho_\Gamma \mathbf{U}_T \cdot \mathbf{H}\mathbf{U}_T \qquad \text{on } \Gamma(t) \tag{60}$$

$$\mathrm{div}_\Gamma \mathbf{U}_T = 0 \qquad \text{on } \Gamma(t) \tag{61}$$

where we used the identity $\dot{\mathbf{n}} = \mathbf{H}\mathbf{U}_T - \nabla_\Gamma^T U_N$. It is clear that the first and the third equation define a geometric PDE (with the covariant material derivative $\mathbf{P}\dot{\mathbf{U}}_T$) on a stationary surface with a solution $\mathbf{U}_T$ and π. However, the second equation will be satisfied if only there is an external force b_N that balances other normal forces:

$$b_N = -\pi\kappa + (2\mu \mathrm{tr}(H\nabla_\Gamma \mathbf{U}_T) - \rho_\Gamma \mathbf{U}_T \cdot \mathbf{H}\mathbf{U}_T) \tag{62}$$

We are assuming that this normal force is always applied to keep the position of the surface, and is composed of a Laplace force, $-\pi\kappa$, and a normal force $N(\mathbf{U}_T)$ that depends on the tangential motion:

$$N(\mathbf{U}_T) = 2\mu \mathrm{tr}(H\nabla_\Gamma \mathbf{U}_T) - \rho_\Gamma \mathbf{U}_T \cdot \mathbf{H}\mathbf{U}_T \tag{63}$$

where the first term is a normal viscous traction caused by the curvatures and the second term is so-called centripetal force.

The tangential system, which we denote as $\mathcal{NS}^*(\mathbf{U}_T) = \mathbf{b}_T$, is coupled with the external to the surface tangent force as follows:

$$\rho_\Gamma \mathbf{P}\dot{\mathbf{U}}_T = -\nabla_\Gamma^T \pi + 2\mu_\Gamma P\,\mathrm{div}_\Gamma D_\Gamma(\mathbf{U}_T) + \mathbf{b}_T \qquad \text{on } \Gamma(t) \tag{64}$$

$$\mathrm{div}_\Gamma \mathbf{U}_T = 0 \qquad \text{on } \Gamma(t) \tag{65}$$

Let us summarize the suggested model of a stationary fluidic interface:

$$U_N = 0 \tag{66}$$

$$\mathcal{NS}^*(\mathbf{U}_T) = \mathbf{b}_T \tag{67}$$

$$b_N = -\pi\kappa + N(\mathbf{U}_T) \tag{68}$$

The momentum and the energy balance laws of a stationary fluidic interface can be derived similarly to the general case. We consider the equation (67) solely and compute the following:

$$\begin{aligned}
&\int_{\Gamma(t)} \rho_\Gamma \dot{\mathbf{U}}_T \, dS = \frac{\delta Q^p_\Gamma}{\delta t} + \frac{\delta Q^c_\Gamma}{\delta t} = \int_{\Gamma(t)} \rho_\Gamma \mathbf{P}\dot{\mathbf{U}}_T \, dS + \int_{\Gamma(t)} \rho_\Gamma \dot{\mathbf{P}}\mathbf{U}_T \, dS \\
&= \int_{\Gamma(t)} (-\nabla^T_\Gamma \pi + 2\mu_\Gamma \mathbf{P} \operatorname{div}_\Gamma D_\Gamma(\mathbf{U}_T) + \mathbf{b}_T) \, dS + \int_{\Gamma(t)} \rho_\Gamma (\dot{\mathbf{U}}_T \cdot \mathbf{n})\mathbf{n} \, dS \\
&= \int_{\Gamma(t)} \mathbf{b}_T \, dS + \int_{\Gamma(t)} (-\pi\kappa\mathbf{n} + 2\mu_\Gamma \mathbf{P} \operatorname{div}_\Gamma D_\Gamma(\mathbf{U}_T) - \rho_\Gamma (\mathbf{U}_T \cdot \mathbf{H}\mathbf{U}_T)\mathbf{n} \, dS \\
&= \int_{\Gamma(t)} \mathbf{b}_T \, dS + \int_{\Gamma(t)} (-\pi\kappa\mathbf{n} + 2\mu \operatorname{tr}(H\nabla_\Gamma \mathbf{U}_T) - \rho_\Gamma (\mathbf{U}_T \cdot \mathbf{H}\mathbf{U}_T)\mathbf{n} \, dS \\
&= \int_{\Gamma(t)} \mathbf{b}_T \, dS + \int_{\Gamma(t)} (-\pi\kappa + N(\mathbf{U}_T))\mathbf{n} \, dS \\
&= \frac{\delta Q^*_\Gamma}{\delta t} + \int_{\Gamma(t)} \rho_\Gamma (\mathbf{U}_T \cdot \mathbf{H}\mathbf{U}_T)\mathbf{n} \, dS = \frac{dQ^*_\Gamma}{dt}
\end{aligned}$$

Similarly,

$$\begin{aligned}
&\frac{d}{dt} E^*_\Gamma = \frac{1}{2}\frac{d}{dt} \int_{\Gamma(t)} \rho_\Gamma \mathbf{U}^2_T \, dS = \int_{\Gamma(t)} \rho_\Gamma \mathbf{U}_T \cdot \dot{\mathbf{U}}_T \, dS = \int_{\Gamma(t)} \rho_\Gamma \mathbf{U}_T \cdot \mathbf{P}\dot{\mathbf{U}}_T \, dS \\
&= \int_{\Gamma(t)} \mathbf{U}_T \cdot \mathbf{b}_T \, dS + \int_{\Gamma(t)} (-\mathbf{U}_T \cdot \nabla^T_\Gamma \pi + 2\mu_\Gamma \mathbf{U}_T \cdot \mathbf{P} \operatorname{div}_\Gamma D_\Gamma(\mathbf{U}_T)) \, dS \\
&= \int_{\Gamma(t)} \mathbf{U}_T \cdot \mathbf{b}_T \, dS + \int_\Gamma \pi \operatorname{div}_\Gamma \mathbf{U}_T \, dS - 2\mu_\Gamma \int_\Gamma D_\Gamma(\mathbf{U}_T) : \nabla_\Gamma \mathbf{U}_T \, dS
\end{aligned}$$

Finally, the following a priori estimates hold:

$$\frac{dQ^*_\Gamma}{dt} = \int_{\Gamma(t)} \mathbf{b}_T \, dS + \int_{\Gamma(t)} (-\pi\kappa + N(\mathbf{U}_T))\mathbf{n} \, dS \tag{69}$$

$$\frac{dE^*_\Gamma}{dt} = \int_{\Gamma(t)} \mathbf{U}_T \cdot \mathbf{b}_T \, dS - 2\mu_\Gamma \int_{\Gamma(t)} \|D_\Gamma \mathbf{U}_T\|^2 \, dS \tag{70}$$

Remark 1.2 *The suggested above momentum and energy laws are due to the structure of* $\mathcal{NS}^*(\mathbf{U}_T) = \mathbf{b}_T$ *equations. If one takes into account* $U_N = 0$ *and* $b_N = -\pi\kappa + N(\mathbf{U}_T)$ *then the non-split momentum law of surface Navier-Stokes can be recovered.*

1.2.6 Mathematical models of two-phase flow with a fluidic interface

Our goal is to investigate proper coupling conditions for the surface flow and the bulk flow such that momentum and energy balance laws are kept valid. We can couple these systems kinematically via velocities, dynamically via forces or any combination of them. The kinematic coupling can be continuous and discontinuous, however the local conservation of the mass guarantees that the normal bulk velocity should be continuous across the interface. Assuming there are no external forces like gravity, the dynamical coupling should be performed through an unknown force $\mathbf{b}$ that, from one hand, enters the surface flow momentum equation, and from another hand balances the jump of stress vector across the interface to guarantee local conservation of the momentum flux:

$$[\boldsymbol{\sigma}]^-_+ \mathbf{n} + \mathbf{b} = 0$$

This coupling technique results in the following two models.

BI *Continuous coupling with fluidic interface*

$$[\mathbf{u}]_+^- = 0 \qquad \text{on } \Gamma(t) \tag{71}$$

$$[\boldsymbol{\sigma}]_+^- \mathbf{n} + \mathbf{b} = 0 \qquad \text{on } \Gamma(t) \tag{72}$$

$$\mathbf{U} = \mathbf{u} \qquad \text{on } \Gamma(t) \tag{73}$$

$$\mathcal{NS}_\Gamma(\mathbf{U}) = \mathbf{b} \qquad \text{on } \Gamma(t) \tag{74}$$

The total bulk momentum and energy can be expressed as follows:

$$\frac{dQ}{dt} = -\int_\Gamma \mathbf{b}\, dS + r \tag{75}$$

$$\frac{dE}{dt} = -\int_{\Omega_\pm} 2\mu \left\|D\mathbf{u}\right\|^2 dV - \int_{\Gamma(t)} \mathbf{U}\cdot\mathbf{b}\, dS + R \tag{76}$$

or, with the help of the balance of surface momentum and energy:

$$\frac{d}{dt}(Q + Q_\Gamma) = r \tag{77}$$

$$\frac{d}{dt}(E + E_\Gamma) = -\int_{\Omega_\pm(t)} 2\mu \left\|D\mathbf{u}\right\|^2 dV - 2\mu_\Gamma \int_{\Gamma(t)} \left\|D_\Gamma \mathbf{U}\right\|^2 dS + R \tag{78}$$

where

$$r = \int_{\partial\Omega_D} \mathbf{t}\, dS + \int_{\partial\Omega_N} \mathbf{f}\, dS \tag{79}$$

$$R = \int_{\partial\Omega} \mathbf{u}\cdot\mathbf{t}\, dS = \int_{\partial\Omega_D} \mathbf{g}\cdot\mathbf{t}\, dS + \int_{\partial\Omega_N} \mathbf{u}\cdot\mathbf{f}\, dS \tag{80}$$

is the total force and the total mechanical power imposed on the outer boundary $\partial\Omega$.

BII *Friction slip on fluidic interface*

$$[\mathbf{u}]_+^- \cdot \mathbf{n} = 0 \qquad \text{on } \Gamma(t) \tag{81}$$

$$u_N = U_N \qquad \text{on } \Gamma(t) \tag{82}$$

$$\mathbf{P}\boldsymbol{\sigma}^- \mathbf{n} = -f_-(\mathbf{P}\mathbf{u}^- - \mathbf{U}_T) \qquad \text{on } \Gamma(t) \tag{83}$$

$$\mathbf{P}\boldsymbol{\sigma}^+ \mathbf{n} = f_+(\mathbf{P}\mathbf{u}^+ - \mathbf{U}_T) \qquad \text{on } \Gamma(t) \tag{84}$$

$$[\boldsymbol{\sigma}]_+^- \mathbf{n} + \mathbf{b} = 0 \qquad \text{on } \Gamma(t) \tag{85}$$

$$\mathcal{NS}_\Gamma(\mathbf{U}) = \mathbf{b} \qquad \text{on } \Gamma(t) \tag{86}$$

and the total bulk momentum and energy can be expressed as follows:

$$\frac{dQ}{dt} = -\int_\Gamma \mathbf{b}\, dS + r \tag{87}$$

$$\frac{dE}{dt} = -\int_{\Omega_\pm} 2\mu \left\|D\mathbf{u}\right\|^2 dV - \int_{\Gamma(t)} \mathbf{U}\cdot\mathbf{b}\, dS - F_\pm + R \tag{88}$$

with the term for the friction dissipation

$$F_\pm = \int_\Gamma f_-(\mathbf{P}\mathbf{u}^- - \mathbf{U}_T)^2 + f_+(\mathbf{P}\mathbf{u}^+ - \mathbf{U}_T)^2\, dS \tag{89}$$

or, with the help of the balance of surface momentum and energy:

$$\frac{d}{dt}(Q + Q_\Gamma) = r \tag{90}$$

$$\frac{d}{dt}(E + E_\Gamma) = -\int_{\Omega_\pm(t)} 2\mu \left\|D\mathbf{u}\right\|^2 dV - 2\mu_\Gamma \int_{\Gamma(t)} \left\|D_\Gamma \mathbf{U}\right\|^2 dS - F_\pm + R \tag{91}$$

Both presented models have correct total mass, momentum and energy balance laws.

Then we would like to consider models of coupling the stationary fluidic interface with bulk flows.

SI *Continuous coupling on stationary fluidic interface*

$$[\mathbf{u}]_+^- = 0 \qquad \text{on } \Gamma(t) \tag{92}$$

$$[\boldsymbol{\sigma}]_+^- \mathbf{n} + \mathbf{b} = 0 \qquad \text{on } \Gamma(t) \tag{93}$$

$$\mathbf{U} = \mathbf{u} \qquad \text{on } \Gamma(t) \tag{94}$$

$$U_N = 0 \qquad \text{on } \Gamma(t) \tag{95}$$

$$\mathcal{NS}^*(\mathbf{U}_T) = \mathbf{b}_T \qquad \text{on } \Gamma(t) \tag{96}$$

Here we choose to relax the normal force equation, $b_N = -\pi\kappa + N(\mathbf{U}_T)$, of the surface Navier-Stokes equation. Indeed, the total bulk momentum and energy laws can be expressed as follows:

$$\frac{d}{dt}(Q + Q_\Gamma) = \frac{d}{dt}(Q + Q_\Gamma^*) = \int_\Gamma (b_N + \pi\kappa - N(\mathbf{U}_T))\mathbf{n}\, dS + r \tag{97}$$

$$\frac{d}{dt}(E + E_\Gamma) = \frac{d}{dt}(E + E_\Gamma^*) = -\int_{\Omega_\pm(t)} 2\mu \left\|D\mathbf{u}\right\|^2 dV - 2\mu_\Gamma \int_{\Gamma(t)} \left\|D_\Gamma \mathbf{U}\right\|^2 dS + R \tag{98}$$

qSI *Continuous coupling on quasi stationary fluidic interface*

$$[\mathbf{u}]_+^- = 0 \qquad \text{on } \Gamma(t) \tag{99}$$

$$[\boldsymbol{\sigma}]_+^- \mathbf{n} + \mathbf{b} = 0 \qquad \text{on } \Gamma(t) \tag{100}$$

$$\mathbf{U} = \mathbf{u} \qquad \text{on } \Gamma(t) \tag{101}$$

$$\mathcal{NS}^*(\mathbf{U}_T) = \mathbf{b}_T \qquad \text{on } \Gamma(t) \tag{102}$$

$$b_N = -\pi\kappa + N(\mathbf{U}_T) \qquad \text{on } \Gamma(t) \tag{103}$$

Here we choose to relax the condition of a stationary surface, $U_N = 0$. This means that

while we use the equilibrium force $b_N$to balance the bulk stress jump, we cannot expect the surface to be at the same position. The total bulk momentum and energy can be expressed as follows:

$$\frac{d}{dt}(Q+Q_\Gamma)-\int_{\Gamma(t)}\rho_\Gamma(\dot{U}_N\mathbf{n}+U_N\dot{\mathbf{n}})\,dS=\frac{d}{dt}(Q+Q_\Gamma^*)=r \tag{104}$$

$$\frac{d}{dt}(E+E_\Gamma)-\int_{\Gamma(t)}\rho_\Gamma U_N\dot{U}_N\,dS=\frac{d}{dt}(E+E_\Gamma^*) \tag{105}$$

$$=-\int_{\Gamma(t)}U_N(-\pi\kappa+N(\mathbf{U}_T))\,dS-\int_{\Omega_\pm(t)}2\mu\left\|D\mathbf{u}\right\|^2dV-2\mu_\Gamma\int_{\Gamma(t)}\left\|D_\Gamma\mathbf{U}_T\right\|^2dS+R \tag{106}$$

SII *Friction slip on stationary fluidic interface with external force*

$$[\mathbf{u}]_+^-\cdot\mathbf{n}=0 \qquad \text{on } \Gamma(t) \tag{107}$$

$$u_N=U_N \qquad \text{on } \Gamma(t) \tag{108}$$

$$\mathbf{P}\boldsymbol{\sigma}^-\mathbf{n}=-f_-(\mathbf{P}\mathbf{u}^--\mathbf{U}_T) \qquad \text{on } \Gamma(t) \tag{109}$$

$$\mathbf{P}\boldsymbol{\sigma}^+\mathbf{n}=f_+(\mathbf{P}\mathbf{u}^+-\mathbf{U}_T) \qquad \text{on } \Gamma(t) \tag{110}$$

$$[\boldsymbol{\sigma}]_+^-\mathbf{n}+\mathbf{b}=0 \qquad \text{on } \Gamma(t) \tag{111}$$

$$U_N=0 \qquad \text{on } \Gamma(t) \tag{112}$$

$$\mathcal{NS}^*(\mathbf{U}_T)=\mathbf{b}_T+\mathbf{b}_T^e \qquad \text{on } \Gamma(t) \tag{113}$$

Here we choose to relax the normal force equation, $b_N=-\pi\kappa+N(\mathbf{U}_T)$, of the surface Navier-Stokes equation. And the total bulk momentum can be expressed as follows:

$$\frac{d}{dt}(Q+Q_\Gamma)=\int_\Gamma\mathbf{b}_N\,dS+r \tag{114}$$

The total energy balance law for the interface above can be derived similarly to the BII

interface:

$$\frac{dE}{dt} + \frac{dE_\Gamma}{dt} = -\int_{\Omega_\pm} 2\mu \left\|D\mathbf{u}\right\|^2 dV - 2\mu_\Gamma \int_{\Gamma(t)} \left\|D_\Gamma \mathbf{U}_T\right\|^2 dS + F^e - F_\pm + R \tag{115}$$

where

$$F^e = \int_\Gamma \mathbf{U}_T \cdot \mathbf{b}_T^e \, dS \tag{116}$$

qSII *Friction slip on quasi stationary fluidic interface with external force*

$$[\mathbf{u}]_+^- \cdot \mathbf{n} = 0 \qquad \text{on } \Gamma(t) \tag{117}$$

$$u_N = U_N \qquad \text{on } \Gamma(t) \tag{118}$$

$$\mathbf{P}\boldsymbol{\sigma}^- \mathbf{n} = -f_-(\mathbf{P}\mathbf{u}^- - \mathbf{U}_T) \qquad \text{on } \Gamma(t) \tag{119}$$

$$\mathbf{P}\boldsymbol{\sigma}^+ \mathbf{n} = f_+(\mathbf{P}\mathbf{u}^+ - \mathbf{U}_T) \qquad \text{on } \Gamma(t) \tag{120}$$

$$[\boldsymbol{\sigma}]_+^- \mathbf{n} + \mathbf{b} = 0 \qquad \text{on } \Gamma(t) \tag{121}$$

$$\mathcal{NS}^*(\mathbf{U}_T) = \mathbf{b}_T + \mathbf{b}_T^e \qquad \text{on } \Gamma(t) \tag{122}$$

$$b_N = -\pi\kappa + N(\mathbf{U}_T) \qquad \text{on } \Gamma(t) \tag{123}$$

Here we choose to relax $U_N = 0$, the condition of a purely tangential interface motion. As a consequence, while we use the equilibrium force b_N to balance the bulk stress jump, we cannot expect surface to be at the same position. Since the $U_N \neq 0$ it may be more consistent to keep the κU_N term in the incompressibility condition (65) of $\mathcal{NS}^*(\mathbf{U}_T) = \mathbf{b}_T + \mathbf{b}^e$. The total bulk momentum can be expressed as follows:

$$\frac{d}{dt}(Q + Q_\Gamma) = r \tag{124}$$

The energy balance law for the interface above can be derived similarly to the BII interface:

$$\frac{dE}{dt} + \frac{dE_\Gamma^*}{dt} = -\int_\Gamma U_N b_N \, dS - \int_{\Omega_\pm} 2\mu \left\| D\mathbf{u} \right\|^2 dV - 2\mu_\Gamma \int_{\Gamma(t)} \left\| D_\Gamma \mathbf{U}_T \right\|^2 dS + F^e - F_\pm + R \quad (125)$$

1.3 Initial and boundary conditions

For the models discussed in the previous sections, one needs suitable initial and boundary conditions for velocity fields $\mathbf{u}$ and $\mathbf{U}$. The initial condition is $\mathbf{u}(\mathbf{x}, 0) = \mathbf{u}_o(x)$ and $\mathbf{U}(\mathbf{x}, 0) = \mathbf{U}_o(x)$ with given vector fields $\mathbf{u}_0, \mathbf{U}_0$, which usually come from the underlying physical problems. For boundary conditions, one can distinguish between essential and natural boundary conditions. Recall the previous settings $\partial\Omega = \partial\Omega_D \cup \partial\Omega_N$ and $\partial\Omega_D \cap \partial\Omega_N = \emptyset$, one uses the essential boundary conditions on $\partial\Omega_D$ which are Dirichlet type. The essential boundary conditions usually describe inflow conditions or conditions at wall in applications. Dirichlet conditions have the form,

$$\mathbf{u}(\mathbf{x}, t) = \mathbf{u}_D(\mathbf{x}, t) \qquad \text{on } \partial\Omega_D \quad (126)$$

with a given vector field $\mathbf{u}_D$. For example if $\partial\Omega_D$ corresponds to a fixed wall, the no-slip condition can be described by setting $\mathbf{u}_D = 0$ for all t *and* $\mathbf{x} \in \partial\Omega_D$. The natural boundary condition are given in the form of,

$$\boldsymbol{\sigma}\mathbf{n} = p_{ext}\mathbf{n} \text{ on } \partial\Omega_N \quad (127)$$

with the outward normal $\mathbf{n}$ and given function p_{ext} which prescribed stresses on $\partial\Omega_N$. An example would be $p_{ext} = 0$, we obtain a homogeneous natural boundary conditions.

1.4 Numerical challenges

The finite element approximation of multi-phase problems involving immiscible fluids features several challenging aspects. The first challenge is the presence of a sharp interface between the two

phases, that might move and undergo topological changes. The second critical aspect is the presence of surface tension forces that create a jump in the pressure field at the interface. In addition, if one accounts for slip between phases [45], a jump in the velocity field at the interface needs to be captured as well. Finally, a lack of robustness may arise when there is high contrast in fluid densities and viscosities. Tackling all of these challenges motivated a large body of literature. One possible way to categorize numerical methods proposed in the literature is to distinguish between *diffusive interface* and *sharp interface* approaches. Phase field methods (e.g., [2, 50]) belong to the first category, while level set methods (e.g., [97]), and conservative level set methods (e.g., [81]) belong to the second. Diffusive interface methods introduce a smoothing region around the interface between the two phases to vary smoothly, instead of sharply, from one phase to the other and usually apply the surface tension forces over the entire smoothing region. The major limitation of diffusive interface methods lies in the need to resolve the smoothing region with an adequate number of elements, which results in high computational costs. Sharp interface methods require fewer elements to resolve the interface between phases. Thus, we will restrict our attention to sharp interface approaches, which can be further divided into *geometrically fitted* and *unfitted* methods.

In fitted methods, the discretization mesh is fitted to the computational interface. Perhaps, Arbitrary Lagrangian Eulerian (ALE) methods [24] are the best known fitted methods. In case of a moving interface, ALE methods deform the mesh to track the interface. While ALE methods are known to be very robust for small interface displacement, complex re-meshing procedures are needed for large deformations and topological changes. Certain variations of the method, like the extended ALE [4, 3], successfully deal with large interface displacement while keeping the same mesh connectivity. The price to pay for such improvement is a higher computational cost. Unfitted methods allow the sharp interface to cut through the elements of a fixed background grid. Their main advantage is the relative ease of handling time-dependent domains, implicitly defined interfaces, and problems with strong geometric deformations [11]. The immersed finite element method (e.g., [1]) and front-tracking methods (e.g., [100]) are examples of unfitted approaches. Applied in the finite element framework, these methods require an enrichment of the elements

intersected by the interface in order to capture jumps and kinks in the solution. One complex aspect of these methods is the need for tailored stabilization. CutFEM uses overlapping fictitious domains in combination with ghost penalty stabilization [14] to enrich and stabilize the solution. See [22, 28, 44, 47, 65, 105] for the application of CutFEM or Nitsche-XFEM to approximate two-phase flows. Finally, recently proposed unfitted methods are a hybrid high-order method [16] and an enriched finite element/level-set method [46].

In this thesis, we study an isoparametric unfitted finite element approach of the CutFEM or Nitsche-XFEM family for the simulation of multi-phase Stokes problems. For more details on the isoparametric unfitted finite element, we refer to [58, 59, 61].

Two-phase flow problems with high contrast for the viscosity are known to be especially challenging. While some authors test different viscosity ratios but do not comment on the effects of high contrast on the numerics [22, 46, 106], others show or prove that their method is robust for all viscosity ratios [47, 16, 55, 78, 105]. In other cases, numerical parameters, like the penalty parameters, are adjusted to take into account large differences in the viscosity [28]. Through analysis and a series of numerical tests in two and three dimensions, we demonstrate in Sec. 2.4 and Sec. 2.5 that our approach is robust not only with respect to the contrast in viscosity, but also with respect to the slip coefficient value and the position of the interface relative to the fixed computational mesh.

1.5 The Cahn–Hilliard equation and phase separation

The Cahn-Hilliard equation on a stationary, flat domain was introduced in the late 50s to model segregation of two components in a mixture. In the section, we will derive the Cahn-Hilliard equations on an evolving surface from conservation laws.

Let $(\Gamma(t))_{t\in[0,T]}$ be a time dependent at least C^2 smooth closed hyper-surface in $\mathbb{R}^3$. Assume there is a domain Ω such that $\Gamma(t) \subset \Omega$ for all t. Let $\mathbf{n}$ denote the outward normal vector on Γ.

The evolution of the material surface can be characterized by the Lagrangian mapping $\Phi(t,\cdot)$:

$\Gamma(0) \to \Gamma(t)$ with the following definitions:

$$\Phi(0, \mathbf{x}) = \mathbf{x}, \ \frac{\partial \Phi(t, \mathbf{x})}{\partial t} = \mathbf{u}(t, \Phi(t, \mathbf{x})), \ t \in [0, T] \tag{128}$$

Consider a heterogeneous mixture of two species with densities ρ_i, $i \in \{1, 2\}$, and denote $\rho := \rho_1 + \rho_2$ characterizing the total density. On every $S(t) \subset \Omega(t)$, the conservation of mass can be expressed as,

$$0 = \frac{d}{dt} \int_{S(t)} \rho ds = \int_{S(t)} (\dot{\rho} + \rho \operatorname{div}_\Gamma \mathbf{u}) \ ds. \tag{129}$$

which implies,

$$\dot{\rho} + \rho \operatorname{div}_\Gamma \mathbf{u} = 0 \qquad \text{on } \Gamma(t) \tag{130}$$

We introduce scalar fields $c_i = m_i/m \in L^2(\Omega(t)), \ i \in \{1, 2\}$ for specific mass concentrations to describe the dynamics of phases, with m_i are the masses of the components and $m = m_1 + m_2$ represents the total mass. Without lost of generality, we consider c_1 as representative concentration c. Clearly, $c \in [0, 1], c_2 = 1 - c$. The mass conservation for arbitrary subdomain $\gamma(t) \subset \Gamma(t)$ can be described as,

$$\frac{d}{dt} \int_{\gamma(t)} \rho c \ ds = - \int_{\partial \gamma(t)} \mathbf{j} \cdot \mathbf{m} \ d\gamma \tag{131}$$

where $\mathbf{j}$ denotes the flux.

Following from (40), we attain the following equation,

$$\int_{\gamma(t)} (\dot{\rho} c + \dot{c} \rho + c \rho \operatorname{div}_\Gamma \mathbf{u}) \ ds = - \int_{\gamma(t)} \operatorname{div}_\Gamma \mathbf{j} \ ds \tag{132}$$

Thanks to (130), one could further simplify the above equality to,

$$\int_{\gamma(t)} \dot{c}\rho \; ds = -\int_{\gamma(t)} \mathrm{div}_\Gamma \mathbf{j} \; ds \tag{133}$$

Since the equality holds for arbitrary $\gamma(t)$, the following holds,

$$\dot{c} + \frac{1}{\rho}\,\mathrm{div}_\Gamma \mathbf{j} = 0 \tag{134}$$

Following from Fick's law, we assume,

$$\mathbf{j} := -M\nabla_\Gamma \mu, \;\; \mu = \frac{\delta f}{\delta c} \tag{135}$$

where M denotes mobility coefficient and μ denotes chemical potential which defined as functional derivative of free energy f with respect to concentration c. Assume f has following form,

$$f(c) := \frac{1}{\epsilon} f_0(c) + \frac{\epsilon}{2}|\nabla_\Gamma c|^2 \tag{136}$$

where $f_0(c)$ represents the free energy per unit surface which needs to be non-convex. The second term describes the interfacial free energy. ϵ is a parameter for the size of interface layer between two components.

Combining (130), (133) and (136), we obtain the Cahn-Hilliard equation on evolving surface $\Gamma(t)$,

$$\dot{\rho} + \rho\,\mathrm{div}_\Gamma \mathbf{u} = 0 \qquad \text{on } \Gamma(t), t \in [0,T] \tag{137}$$

$$\dot{c} + \frac{1}{\rho}\,\mathrm{div}_\Gamma(M\nabla_\Gamma(\frac{1}{\epsilon} f_0^{'}(c) - \epsilon\,\triangle_\Gamma c)) = 0 \qquad \text{on } \Gamma(t), t \in [0,T] \tag{138}$$

with initial conditions,

$$\rho(\cdot,t) = \rho_0, \;\; c(\cdot,t) = c_0 \text{ on } \Gamma(0) \tag{139}$$

1.6 Machine learning for predicting nonlinear dynamics

Solving strongly-coupled nonlinear partial differential equations characterizing multi-scale, multi-physics process is computationally expensive for many practical reasons. Therefore, the necessity for developing a prediction strategy with high fidelity by only utilizing observational data highly increased over the last decades [93, 56, 70, 107, 99, 32, 26, 13]. One of the most appealing advantages of data-driven models that are trained on data from high fidelity numerical simulations is that they can be used to accelerate the prediction of computationally demanding complex dynamic systems. Besides, data-driven models can be a complement to traditional numerical methods in the following ways: (a) they can efficiently integrate high-dimensional, non-linear, coupled PDE system with multi spatial-temporal scales; (b) in some cases they can efficiently generate missing data or help predict unknown parameters; (c) they can help the system to be deterministic when part of the system is not fully understood.

More recently, various machine learning methods have been investigated for complex dynamic system simulation or prediction [66, 82, 62]. Among all the sequential model approaches for predicting time series, artificial neural networks (ANNs) [86, 88, 92], recurrent neural networks(RNNs) [69, 63, 103, 109, 111, 66, 103, 57], and gated recurrent units(GRU) [107, 30] are the most popular ones. The Neural Network method was initially motivated by modeling sequence processing in mammalian brains. The human brain contains billions of neurons that are connected with each other to form a network. When the network receives signals from either eyes, ears nose, or skin, it recognizes the signals and processes them with the output. ANNs are models which directly mimic the structure of biological neural networks. ANNs usually have a network structure of neuron-processing units interconnected by weighted links. RNNs is a class of ANNs where connections between neurons form a directed graph along a temporal sequence. Unlike most feedforward neural networks, this structure allows RNN to exhibit temporal dynamic behavior. This makes RNNs applicable to tasks such as speech recognition, handwriting recognition and etc. In recent studies, several promising results have been published regarding using RNNs in weather/climate models

within machine learning communities [9, 87].

At the beginning of the 20th century, a simplified type of recurrent neural network called echo state network (ESN) has been proposed by Wolfgang Maass and his colleagues [64]. The main idea of the method is to generate a large fixed random recurrent neural network with an input signal, inducing that in each neuron within this recurrent layer a nonlinear response signal, and linearly combine the desired output signal by a trainable output layer.

Not until recently, Vlachas and Chattopadhyay published results illustrate that ESN outperform other major RNNs structures such as LSTM and ANN structure in predicting chaotic dynamical systems [102, 64] . We explore the applicability of artificial neural networks in the prediction of pattern formation for the Cahn-Hilliard model in the last chapter.

1.7 Outline of the thesis

The remainder of the thesis is organized as follows. **Chapter 2** is devoted to studying an isoparametric unfitted finite element approach of the CutFEM or Nitsche-XFEM family for the simulation of two-phase Stokes problems with slip between phases. All the numerical works consider the homogeneous model of two-phase flow, i.e. no slip is assumed between the phases. We introduce the strong and weak formulations of the model, together with the finite element discretization. We present a stability result and prove optimal order convergence for the proposed unfitted finite element approach. Numerical results in 2 and 3-dimensional simulations validate these computational approaches.

Chapter 3 demonstrates the successful application of CutFEM & TraceFEM for two immiscible, viscous, and incompressible fluids separated by a viscous inextensible material interface modeled as a Boussinesq–Scriven surface fluid. The following coupling conditions are prescribed between the bulk two-phase flow and the surface fluid: (i) the immiscibility condition, i.e. the bulk fluid does not penetrate through the interface; (ii) slip with friction between the bulk fluid and the viscous interface; and (iii) the load exerted from the bulk fluid onto the surface fluid defined by the jump of the normal stress across the interface. We introduce the strong formulation of the coupled

problem and the associated energy balance. Then we present the strong and weak formulations of the simplified problem, together with the finite element discretization. A partitioned algorithm for the numerical solution of the coupled problem was proposed. Numerical results in 3 dimensions are reported.

In **Chapter 4**, the performance of two deep learning methods for reproducing short-term and long-term statistics of multi-scale spatio-temporal data from the Cahn-Hilliard system is examined. The applicability of two recurrent neural networks specifically echo state network (ESN) and long short-term memory (LSTM) is explored. The numerical discretization scheme of the Cahn-Hilliard system is briefly discussed. Then we present two RNNs (ESN and LSTM) architectures. And prediction results are reported later in this chapter.

2 A two-phase fluid with slip between phases

2.1 Problem description

We consider a fixed domain $\Omega \subset \mathbb{R}^d$, with $d = 2, 3$, filled with two immiscible, viscous, and incompressible fluids separated by an interface Γ. In this study, we assume Γ does not evolve with time although our approach is designed to handle interface evolution. We assume that Γ is closed and sufficiently smooth. Interface Γ separates Ω into two subdomains (phases) Ω^+ and $\Omega^- = \Omega \setminus \overline{\Omega^+}$. We assume Ω^- to be completely internal, i.e. $\partial\Omega^- \cap \partial\Omega = \emptyset$. See Fig. 2. Let $\mathbf{n}^\pm$ be the outward unit normal for $\Omega^\pm$ and $\mathbf{n}$ the outward pointing unit normal on Γ. It holds that $\mathbf{n}^- = \mathbf{n}$ and $\mathbf{n}^+ = -\mathbf{n}$ at Γ.

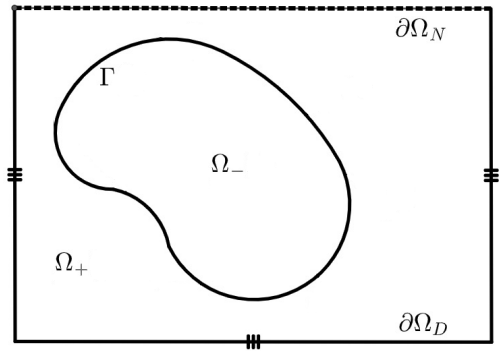

Figure 2: Illustration of a domain Ω in $\mathbb{R}^2$. On part of the boundary (dashed line) a Neumann boundary condition is imposed, while on the remaining part of the boundary (solid line with three bars) a Dirichlet boundary condition is enforced.

Let $\mathbf{u}^\pm : \Omega^\pm \to \mathbb{R}^d$ and $p^\pm : \Omega^\pm \to \mathbb{R}$ denote the fluid velocity and pressure, respectively. We model the motion of the fluids occupying subdomains $\Omega^\pm$ by the Stokes equations as in Sec. 1.2.3

$$-\nabla \cdot \boldsymbol{\sigma}^\pm = \mathbf{f}^\pm \qquad \text{in } \Omega^\pm, \tag{140}$$

$$\nabla \cdot \mathbf{u}^\pm = 0 \qquad \text{in } \Omega^\pm, \tag{141}$$

endowed with boundary conditions

$$\mathbf{u}^+ = \mathbf{g}, \qquad \text{on } \partial\Omega_D, \tag{142}$$

$$\boldsymbol{\sigma}^+\mathbf{n}^+ = \mathbf{g}_N \qquad \text{on } \partial\Omega_N. \tag{143}$$

Here, $\overline{\partial\Omega_D} \cup \overline{\partial\Omega_N} = \overline{\partial\Omega}$ and $\partial\Omega_D \cap \partial\Omega_N = \emptyset$. See Fig. 2. In (140), $\mathbf{f}^\pm$ are external the body forces and $\boldsymbol{\sigma}^\pm$ are the Cauchy stress tensors. For Newtonian fluids, the Cauchy stress tensor has the following expression:

$$\boldsymbol{\sigma}^\pm = -p^\pm\mathbf{I} + 2\mu^\pm\mathbf{D}(\mathbf{u}^\pm), \quad \mathbf{D}(\mathbf{u}^\pm) = \frac{1}{2}(\nabla\mathbf{u}^\pm + (\nabla\mathbf{u}^\pm)^T) \text{ in } \Omega^\pm,$$

where constants $\mu^\pm$ represent the fluid dynamic viscosities. Finally, $\mathbf{g}$ and $\mathbf{g}_N$ in (142) and (143) are given.

Subproblems (140)-(141) are coupled at the interface Γ. Recall the AII model in 1.2.3, the conservation of mass requires the balance of normal fluxes on Γ:

$$\mathbf{u}^+ \cdot \mathbf{n} = \mathbf{u}^- \cdot \mathbf{n} \qquad \text{on } \Gamma. \tag{144}$$

This is the first coupling condition. We are interested in modeling slip with friction between the two phases. Thus, we consider the following additional coupling conditions:

$$\mathbf{P}\boldsymbol{\sigma}^+\mathbf{n} = f(\mathbf{P}\mathbf{u}^+ - \mathbf{P}\mathbf{u}^-) \qquad \text{on } \Gamma, \tag{145}$$

$$\mathbf{P}\boldsymbol{\sigma}^-\mathbf{n} = -f(\mathbf{P}\mathbf{u}^- - \mathbf{P}\mathbf{u}^+) \qquad \text{on } \Gamma, \tag{146}$$

where f is a constant that can be seen as a slip coefficient and $\mathbf{P} = \mathbf{P}(\mathbf{x}) = I - \mathbf{n}(\mathbf{x})\mathbf{n}(\mathbf{x})^T$ for $\mathbf{x} \in \Gamma$ is the orthogonal projection onto the tangent plane. Finally, the jump of the normal stress

across Γ is given by:

$$[\mathbf{n}^T \boldsymbol{\sigma} \mathbf{n}]_+^- = \sigma\kappa \qquad \text{on } \Gamma, \tag{147}$$

where σ is the surface tension coefficient and κ is the double mean curvature of the interface.

Since the boundary conditions on $\partial\Omega$ do not affect the subsequent discussion, from now on we will consider that a Dirichlet condition (142) is imposed on the entire boundary. This will simplify the presentation of the fully discrete problem.

2.1.1 Variational formulation

The purpose of this section is to derive the variational formulation of coupled problem (140)–(147). Let us introduce some standard notation. The space of functions whose square is integrable in a domain ω is denoted by $L^2(\omega)$. With $L_0^2(\omega)$, we denote the space of functions in $L^2(\omega)$ with zero mean value over ω. The space of functions whose distributional derivatives of order up to $m \geq 0$ (integer) belong to $L^2(\omega)$ is denoted by $H^m(\omega)$. The space of vector-valued functions with components in $L^2(\omega)$ is denoted with $L^2(\omega)^d$. $H^1(\mathrm{div}\,, \omega)$ is the space of functions in $L^2(\omega)$ with divergence in $L^2(\omega)$. Moreover, we introduce the following functional spaces:

$$V^- = H^1(\Omega^-)^d,\ V^+ = \{\mathbf{u} \in H^1(\Omega^+)^d, \mathbf{u}\big|_{\partial\Omega_D} = \mathbf{g}\},\ V_0^+ = \{\mathbf{u} \in H^1(\Omega^+)^d, \mathbf{u}\big|_{\partial\Omega_D} = \mathbf{0}\},$$
$$V^{\pm} = \{\mathbf{u} = (\mathbf{u}^-, \mathbf{u}^+) \in V^- \times V^+, \mathbf{u}^- \cdot \mathbf{n} = \mathbf{u}^+ \cdot \mathbf{n} \text{ on } \Gamma\},$$
$$V_0^{\pm} = \{\mathbf{u} = (\mathbf{u}^-, \mathbf{u}^+) \in V^- \times V_0^+, \mathbf{u}^- \cdot \mathbf{n} = \mathbf{u}^+ \cdot \mathbf{n} \text{ on } \Gamma\},$$
$$Q^{\pm} = \{p = (p^-, p^+) \in L^2(\Omega^-) \times L^2(\Omega^+)\}.$$

Notice that space $V^{\pm}$ can be also characterized as $(V^- \times V^+) \cap H^1(\mathrm{div}\,, \Omega)$. We use $(\cdot,\cdot)_\omega$ and $\langle , \rangle_\omega$ to denote the L^2 product and the duality pairing, respectively.

The integral formulation of the problem (140)-(147) reads: Find $(\mathbf{u}, p) \in V^{\pm} \times L^2(\Omega)/\mathbb{R}$ such

that

$$
\begin{aligned}
&-(p^-,\nabla\cdot\mathbf{v}^-)_{\Omega^-}-(p^+,\nabla\cdot\mathbf{v}^+)_{\Omega^+}+2(\mu_-\mathbf{D}(\mathbf{u}^-),\mathbf{D}(\mathbf{v}^-))_{\Omega^-}+2(\mu_+\mathbf{D}(\mathbf{u}^+),\mathbf{D}(\mathbf{v}^+))_{\Omega^+}\\
&\quad+\langle f(\mathbf{P}\mathbf{u}^- -\mathbf{P}\mathbf{u}^+),\mathbf{P}\mathbf{v}^-\rangle_\Gamma+\langle f(\mathbf{P}\mathbf{u}^+ -\mathbf{P}\mathbf{u}^-),\mathbf{P}\mathbf{v}^+\rangle_\Gamma\\
&\quad=(\mathbf{f}^-,\mathbf{v}^-)_{\Omega^-}+(\mathbf{f}^+,\mathbf{v}^+)_{\Omega^+}+\langle\sigma\kappa,\mathbf{v}^-\cdot\mathbf{n}\rangle_\Gamma \qquad (148)\\
&(\nabla\cdot\mathbf{u}^-,q^-)_{\Omega^-}+(\nabla\cdot\mathbf{u}^+,q^+)_{\Omega^+}=0 \qquad (149)
\end{aligned}
$$

for all $(\mathbf{v},q)\in V_0^\pm\times Q^\pm$. The interface terms in (148) have been obtained using coupling conditions (145), (146), and (147) as follows:

$$
\begin{aligned}
-\langle\boldsymbol{\sigma}^-\mathbf{n},\mathbf{v}^-\rangle_\Gamma+\langle\boldsymbol{\sigma}^+\mathbf{n},\mathbf{v}^+\rangle_\Gamma&=-\langle\mathbf{P}\boldsymbol{\sigma}^-\mathbf{n},\mathbf{P}\mathbf{v}^-\rangle_\Gamma+\langle\mathbf{P}\boldsymbol{\sigma}^+\mathbf{n},\mathbf{P}\mathbf{v}^+\rangle_\Gamma-\langle[\mathbf{n}^T\boldsymbol{\sigma}\mathbf{n}]^-_+,\mathbf{v}^-\cdot\mathbf{n}\rangle_\Gamma\\
&=\langle f(\mathbf{P}\mathbf{u}^- -\mathbf{P}\mathbf{u}^+),\mathbf{P}\mathbf{v}^-\rangle_\Gamma+\langle f(\mathbf{P}\mathbf{u}^+ -\mathbf{P}\mathbf{u}^-),\mathbf{P}\mathbf{v}^+\rangle_\Gamma\\
&\quad-\langle\sigma\kappa,\mathbf{v}^-\cdot\mathbf{n}\rangle_\Gamma.
\end{aligned}
$$

Notice that problem (148)-(149) can be rewritten as: Find $(\mathbf{u},p)\in V^\pm\times L^2(\Omega)/\mathbb{R}$ such that

$$
\begin{cases}
a(\mathbf{u},\mathbf{v})+b(\mathbf{v},p)=r(\mathbf{v})\\
\qquad\qquad b(\mathbf{u},q)=0
\end{cases}
\qquad (150)
$$

for all $(\mathbf{v},q)\in V_0^\pm\times Q^\pm$, where

$$
\begin{aligned}
a(\mathbf{u},\mathbf{v})=&2(\mu_-\mathbf{D}(\mathbf{u}^-),\mathbf{D}(\mathbf{v}^-))_{\Omega^-}+2(\mu_+\mathbf{D}(\mathbf{u}^+),\mathbf{D}(\mathbf{v}^+))_{\Omega^+}+\langle f(\mathbf{P}\mathbf{u}^- -\mathbf{P}\mathbf{u}^+),\mathbf{P}\mathbf{v}^- -\mathbf{P}\mathbf{v}^+\rangle_\Gamma,\\
b(\mathbf{v},p)=&-(p^-,\nabla\cdot\mathbf{v}^-)_{\Omega^-}-(p^+,\nabla\cdot\mathbf{v}^+)_{\Omega^+},\\
r(\mathbf{v})=&(\mathbf{f}^-,\mathbf{v}^-)_{\Omega^-}+(\mathbf{f}^+,\mathbf{v}^+)_{\Omega^+}+\langle\sigma\kappa,\mathbf{v}^-\cdot\mathbf{n}\rangle_\Gamma.
\end{aligned}
$$

2.2 Numerical method for solving two-phase flow problem

We consider a family of shape regular triangulations $\{\mathcal{T}_h\}_{h>0}$ of Ω. We adopt the convention that the elements T and edges e are open sets and use the over-line symbol to refer to their closure. Let h_T denote the diameter of element $T \in \mathcal{T}_h$ and h_e the diameter of edge e. The set of elements intersecting $\Omega^{\pm}$ and the set of elements having a nonzero intersection with Γ are

$$\mathcal{T}_h^{\pm} = \{T \in \mathcal{T}_h : T \cap \Omega^{\pm} \neq \emptyset\}, \quad \mathcal{T}_h^{\Gamma} = \{T \in \mathcal{T}_h : \overline{T} \cap \Gamma \neq \emptyset\}, \tag{151}$$

respectively. We assume $\{\mathcal{T}_h^{\Gamma}\}$ to be quasi-uniform. However, in practice adaptive mesh refinement is possible. The domain formed by all tetrahedra in $\mathcal{T}_h^{\Gamma}$ is denoted by $\Omega_h^{\Gamma} := \text{int}(\cup_{T \in \mathcal{T}_h^{\Gamma}} \overline{T})$. We define the h-dependent domains:

$$\Omega_h^{\pm} = \text{int}\left(\cup_{T \in \mathcal{T}_h^{\pm}} \overline{T}\right) \tag{152}$$

and the set of faces of $\mathcal{T}_h^{\Gamma}$ restricted to the interior of $\Omega_h^{\pm}$:

$$\mathcal{E}_h^{\Gamma,\pm} = \{e = \text{int}(\partial T_1 \cap \partial T_2) : T_1, T_2 \in \mathcal{T}_h^{\pm} \text{ and } T_1 \cap \Gamma \neq \emptyset \text{ or } T_2 \cap \Gamma \neq \emptyset\}. \tag{153}$$

For the space discretization of the bulk fluid problems, we restrict our attention to inf-sup stable finite element pair $\mathbf{P}_{k+1} - P_k$, $k \geq 1$, i.e. Taylor-Hood elements. Specifically, we consider the spaces of continuous finite element pressures given by:

$$Q_h^- = \{p \in C(\Omega_h^-) : q|_T \in P_k(T)\ \forall T \in \mathcal{T}_h^-\}. \tag{154}$$

Space Q_h^+ is defined analogously. Our pressure space is given by:

$$Q_h^{\pm} = \{p = (p^-, p^+) \in Q_h^- \times Q_h^+ \ : \ \int_{\Omega^-} \mu_-^{-1} p^- + \int_{\Omega^+} \mu_+^{-1} p^+ = 0\}.$$

Let

$$V_h^- = \{\mathbf{u} \in C(\Omega_h^-)^d : \mathbf{u}|_T \in \mathbf{P}_{k+1}(T)\ \forall T \in \mathcal{T}_h^-\}. \tag{155}$$

with the analogous definition for V_h^+. Our velocity spaces are given by:

$$V_h^{\pm} = \{\mathbf{u} = (\mathbf{u}^-, \mathbf{u}^+) \in V_h^- \times V_h^+\}$$

and $V_{0,h}^{\pm}$, a subspace of $V_h^{\pm}$ with vector functions $\mathbf{u}^+$ vanishing on $\partial\Omega$. All above constructions and spaces readily carry over to tessellations of Ω into squares or cubes and using $\mathbf{Q}_{k+1} - Q_k$ elements.

Functions in $Q_h^{\pm}$ and $V_h^{\pm}$ and their derivatives are multivalued in Ω_h^Γ, the overlap of Ω_h^- and Ω_h^+. The jump of a multivalued function over the interface is defined as the difference of components coming from Ω_h^- and Ω_h^+, i.e. $[\mathbf{u}] = \mathbf{u}^- - \mathbf{u}^+$ on Γ. Note that this is the jump that we have previously denoted with $[\cdot]_+^-$. We are now using $[\cdot]$ to simplify the notation. Moreover, we define the following averages:

$$\{\mathbf{u}\} = \alpha\mathbf{u}^+ + \beta\mathbf{u}^-, \tag{156}$$

$$\langle\mathbf{u}\rangle = \beta\mathbf{u}^+ + \alpha\mathbf{u}^-, \tag{157}$$

where α and β are weights to be chosen such that $\alpha + \beta = 1$, $0 \leq \alpha, \beta \leq 1$. For example, in [22] the setting $\alpha = \mu_-/(\mu_+ + \mu_-)$ and $\beta = \mu_+/(\mu_+ + \mu_-)$ is suggested. In [17], the authors choose $\alpha = 0$, $\beta = 1$ if $\mu_- \leq \mu_+$ and $\alpha = 1$, $\beta = 0$ otherwise. Below, in (161) and (164) we will use relationship:

$$[ab] = [b]\{a\} + \langle b\rangle\,[a]. \tag{158}$$

A discrete variational analogue of problem (150) reads: Find $\{\mathbf{u}_h, p_h\} \in V_h^{\pm} \times Q_h^{\pm}$ such that

$$\begin{cases} a_h(\mathbf{u}_h, \mathbf{v}_h) + b_h(\mathbf{v}_h, p_h) = r_h(\mathbf{v}_h) \\ \\ b_h(\mathbf{u}_h, q_h) - b_p(p_h, q_h) = 0 \end{cases} \tag{159}$$

for all $(\mathbf{v}_h, q_h) \in V_{0,h}^{\pm} \times Q_h^{\pm}$. We define all the bilinear forms in (159) for all $\mathbf{u}_h \in V_h^{\pm}$, $\mathbf{v}_h \in V_{0,h}^{\pm}$, $p \in Q^{\pm}$. Let us start with form $a_h(\cdot, \cdot)$:

$$a_h(\mathbf{u}_h, \mathbf{v}_h) = a_i(\mathbf{u}_h, \mathbf{v}_h) + a_n(\mathbf{u}_h, \mathbf{v}_h) + a_p(\mathbf{u}_h, \mathbf{v}_h), \tag{160}$$

where we group together the terms that arise from the integration by parts of the divergence of the stress tensors:

$$\begin{aligned} a_i(\mathbf{u}_h, \mathbf{v}_h) =& 2(\mu_- \mathbf{D}(\mathbf{u}_h^-), \mathbf{D}(\mathbf{v}_h^-))_{\Omega^-} + 2(\mu_+ \mathbf{D}(\mathbf{u}_h^+), \mathbf{D}(\mathbf{v}_h^+))_{\Omega^+} + \langle f[\mathbf{P}\mathbf{u}_h], [\mathbf{P}\mathbf{v}_h] \rangle_{\Gamma} \\ & - 2\langle \{\mu \mathbf{n}^T \mathbf{D}(\mathbf{u}_h)\mathbf{n}\}, [\mathbf{v}_h \cdot \mathbf{n}] \rangle_{\Gamma}, \end{aligned} \tag{161}$$

and the terms that enforce condition (144) weakly using Nitsche's method

$$a_n(\mathbf{u}_h, \mathbf{v}_h) = \sum_{T \in \mathcal{T}_h^{\Gamma}} \frac{\gamma}{h_T} \{\mu\} \langle [\mathbf{u}_h \cdot \mathbf{n}], [\mathbf{v}_h \cdot \mathbf{n}] \rangle_{\Gamma \cap T} - 2\langle \{\mu \mathbf{n}^T \mathbf{D}(\mathbf{v}_h)\mathbf{n}\}, [\mathbf{u}_h \cdot \mathbf{n}] \rangle_{\Gamma}. \tag{162}$$

We recall that h_T is the diameter of element $T \in \mathcal{T}_h$. To define the penalty terms $a_p(\mathbf{u}_h, \mathbf{v}_h)$ we need ω_e, the facet patch for $e \in \mathcal{E}_h^{\Gamma,\pm}$ consisting of all $T \in \mathcal{T}_h$ sharing e. Then, we set

$$\begin{aligned} a_p(\mathbf{u}_h, \mathbf{v}_h) &= \mu_- \mathbf{J}_h^-(\mathbf{u}_h, \mathbf{v}_h) + \mu_+ \mathbf{J}_h^+(\mathbf{u}_h, \mathbf{v}_h), \\ \mathbf{J}_h^{\pm}(\mathbf{u}_h, \mathbf{v}_h) &= \gamma_{\mathbf{u}}^{\pm} \sum_{e \in \mathcal{E}_h^{\Gamma,\pm}} \frac{1}{h_e^2} \int_{\omega_e} (\mathbf{u}_1^e - \mathbf{u}_2^e) \cdot (\mathbf{v}_1^e - \mathbf{v}_2^e) dx, \end{aligned} \tag{163}$$

where $\mathbf{u}_1^e$ is the componentwise canonical extension of a polynomial vector function $\mathbf{u}_h^{\pm}$ from T_1 to $\mathbb{R}^d$, while $\mathbf{u}_2^e$ is the canonical extension of $\mathbf{u}_h^{\pm}$ from T_2 to $\mathbb{R}^d$(and similarly for $\mathbf{v}_1$, $\mathbf{v}_2$). We

recall that h_e is the diameter of facet $e \in \mathcal{E}_h^{\Gamma,\pm}$. This version of the ghost penalty stabilization has been proposed in [84]. In [60], it was shown to be essentially equivalent to other popular ghost penalty stabilizations such as local projection stabilization [14] and normal derivative jump stabilization [15]. In the context of the Stokes problem, this stabilization was recently used in [104]. For the analysis in Sec. 2.3 and 2.4, we also define $\mathbf{J}_h^{\pm}(\mathbf{u},\mathbf{v})$ for arbitrary smooth functions $\mathbf{u},\mathbf{v}$ in $\Omega_h^{\pm}$. In this case, we set $\mathbf{u}_1 = (\Pi_{T_1}\mathbf{u}|_{T_1})^e$, $\mathbf{u}_2 = (\Pi_{T_2}\mathbf{u}|_{T_2})^e$, where Π_{T_i} is the $L^2(T_i)$-orthogonal projection into the space of degree $k+1$ polynomial vector functions on T_i.

The remaining terms coming from the integration by parts of the divergence of the stress tensors are contained in

$$b_h(\mathbf{v}_h, p_h) = -(p_h^-, \nabla\cdot\mathbf{v}_h^-)_{\Omega^-} - (p_h^+, \nabla\cdot\mathbf{v}_h^+)_{\Omega^+} + \langle\{p_h\}, [\mathbf{v}_h\cdot\mathbf{n}]\rangle_\Gamma\,, \tag{164}$$

and the penalty terms are grouped together in

$$\begin{aligned} b_p(p_h, q_h) &= \mu_-^{-1} J_h^-(p_h, q_h) + \mu_+^{-1} J_h^+(p_h, q_h), \\ J_h^{\pm}(p_h, q_h) &= \gamma_p^{\pm} \sum_{e\in\mathcal{E}_h^{\Gamma,\pm}} \int_{\omega_e} (p_1^e - p_2^e)(q_1^e - q_2^e)dx, \end{aligned} \tag{165}$$

where $p_1^e, p_2^e, q_1^e, q_2^e$ are canonical polynomial extensions as defined above.

Finally,

$$r_h(\mathbf{v}_h) = (\mathbf{f}_h^-, \mathbf{v}_h^-)_{\Omega^-} + (\mathbf{f}_h^+, \mathbf{v}_h^+)_{\Omega^+} + \langle\sigma\kappa, \langle\mathbf{v}_h\cdot\mathbf{n}\rangle\rangle_\Gamma.$$

We recall that some of the interface terms in $a_i(\cdot,\cdot)$ and $b_h(\cdot,\cdot)$ have been obtained using relationship (158) and interface conditions.

Parameters $\gamma_{\mathbf{u}}^{\pm}$, $\gamma_p^{\pm}$ and γ are all assumed to be independent of $\mu_\pm$, h, and the position of Γ against the underlying mesh. Parameter γ in (162) needs to be large enough to provide the bilinear form $a_h(\cdot,\cdot)$ with coercivity. Parameters $\gamma_{\mathbf{u}}^{\pm}$, $\gamma_p^{\pm}$ can be tuned to improve the numerical performance of the method.

2.2.1 Numerical integration

It is not feasible to compute integrals entering the definition of the bilinear forms over cut elements and over Γ for an arbitrary smooth Γ. We face the same problem if Γ is given implicitly as a zero level of a piecewise polynomial function for polynomial degree greater than one. Piecewise linear approximation of Γ on the given mesh and polygonal approximation of subdomains lead to second order geometric consistency error, which is suboptimal for Taylor–Hood elements. To ensure a geometric error of the same order or higher than the finite element (FE) approximation error, we define numerical quadrature rules on the given mesh using the isoparametric approach proposed in [58].

In the isoparametric approach, one considers a smooth function ϕ such that $\pm\phi > 0$ in $\Omega^{\pm}$ and $|\nabla\phi| > 0$ in a sufficiently wide strip around Γ. Next, one defines polygonal auxiliary domains $\Omega_1^{\pm}$ given by $\Omega_1^{\pm} := \{\mathbf{x} \in \mathbb{R}^d : \pm I_h^1(\phi) > 0\}$, where I_h^1 is the continuous piecewise *linear* interpolation of ϕ on $\mathcal{T}_h$. Interface Γ_1 between Ω_1^+ and Ω_1^- is then $\Gamma_1 := \{\mathbf{x} \in \mathbb{R}^d : I_h^1(\phi) = 0\}$. On $\Omega_1^{\pm}$ and Γ_1 standard quadrature rules can be applied elementwise. Since using $\Omega_1^{\pm}$, Γ_1 alone limits the accuracy to second order, one further constructs a transformation of the mesh in $\mathcal{T}_h^{\Gamma}$ with the help of an explicit mapping Ψ_h parameterized by a finite element function. The mapping Ψ_h is such that Γ_1 is mapped *approximately* onto Γ; see [58] for how Ψ_h is constructed. Then, $\widetilde{\Omega}^{\pm} = \Psi_h(\Omega_1^{\pm})$, $\widetilde{\Gamma} = \Psi_h(\Gamma_1)$ are high order accurate approximations to the phases and interface which have an explicit representation so that the integration over $\widetilde{\Omega}^{\pm}$ and $\widetilde{\Gamma}$ can be done exactly. The finite element spaces have to be adapted correspondingly, using the explicit pullback mapping: $\mathbf{v}_h \circ \Psi_h^{-1}$.

2.3 Stability

For the analysis in this and the next section, we assume that the integrals over cut elements in $\Omega^{\pm}$ are computed exactly. In addition, we restrict our attention to the choice $\alpha = 0$ and $\beta = 1$ for the averages in (156)–(157), assuming $\mu_- \leq \mu_+$.

The key for the stability analysis of the two-phase Stokes problem is an inf-sup stability property of the unfitted generalized Taylor–Hood finite element pair, which extends the classical LBB stability result for the standard $\mathbf{P}_{k+1} - P_k$ Stokes element from [5]. There is no similar stability result in the literature for $\mathbf{Q}_{k+1} - Q_k$ unfitted elements. However, we expect that the extension, and so the analysis below, can be carried over to these elements as well.

One is interested in the inf-sup inequality with a stability constant that is independent of the viscosity ratio, position of Γ with respect to the background mesh and, of course, mesh size h. The result is given in the following lemma.

Lemma 2.1 *Denote by V_h the space of continuous P_{k+1} finite element vector functions on Ω, $V_h = \{\mathbf{u} \in C(\Omega)^d : \mathbf{u}|_T \in \mathbf{P}_{k+1}(T)\ \forall T \in \mathcal{T}_h\}$. There exists $h_0 > 0$ such that for all $h < h_0$ and any $q_h \in Q_h^{\pm}$ there exists $\mathbf{v}_h \in V_h$ such that it holds*

$$\begin{aligned} \mu_-^{-1}\|q_h^-\|^2_{\Omega_h^-} + \mu_+^{-1}\|q_h^+\|^2_{\Omega_h^+} &\leq (q_h^-, \nabla\cdot\mathbf{v}_h)_{\Omega^-} + (q_h^+, \nabla\cdot\mathbf{v}_h)_{\Omega^+} + c\, b_p(q_h, q_h) \\ \|\mu^{\frac{1}{2}}\nabla\mathbf{v}_h\|^2_{\Omega} &\leq C\,\left(\mu_-^{-1}\|q_h^-\|^2_{\Omega_h^-} + \mu_+^{-1}\|q_h^+\|^2_{\Omega_h^+}\right). \end{aligned} \tag{166}$$

with h_0 and two positive constants c and C independent of q_h, $\mu_\pm$, the position of Γ in the background mesh and mesh size h.

Proof: Consider subdomains $\Omega_{h,i}^{\pm} \subset \Omega^{\pm}$ built of all strictly internal simplexes in each phase:

$$\overline{\Omega}_{h,i}^{\pm} := \bigcup\{\overline{T} \,:\, T \in \mathcal{T}_h, \quad T \subset \Omega^{\pm}\}.$$

The following two results are central for the proof. First, we have the uniform inf-sup inequalities in $\Omega_{h,i}^-$ and $\Omega_{h,i}^+$ [39]: there exist constants $C_\pm$ independent of the position of Γ and h such that

$$0 < C_\pm \leq \inf_{q\in Q_h^{\pm}\cap L_0^2(\Omega_{h,i}^{\pm})} \sup_{\substack{\mathbf{v}\in V_h \\ \mathrm{supp}(\mathbf{v})\subset\Omega_{h,i}^{\pm}}} \frac{(q, \nabla\cdot\mathbf{v})_{\Omega_{h,i}^{\pm}}}{\|\mathbf{v}\|_{H^1(\Omega_{h,i}^{\pm})}\|q\|_{\Omega_{h,i}^{\pm}}}. \tag{167}$$

The above result can be equivalently formulated as follows: For any $q \in Q_h^{\pm} \cap L_0^2(\Omega_{h,i}^{\pm})$ there exist $\mathbf{v}_h^{\pm} \in V_h$ such that $\mathrm{supp}(\mathbf{v}) \subset \Omega_{h,i}^{\pm}$ and

$$\|q^{\pm}\|^2_{\Omega_{h,i}^{\pm}} = \left(q^{\pm}, \nabla \cdot \mathbf{v}_h^{\pm}\right)_{\Omega_h^{\pm}}, \quad \|\nabla \mathbf{v}_h^{\pm}\|_{\Omega} \leq C_{\pm}^{-1} \|q^{\pm}\|_{\Omega_{h,i}^{\pm}}. \tag{168}$$

The second important results is the simple observation that the L^2 norm of q_h in $\Omega_h^{\pm}$ can be controlled by the L^2 norm in $\Omega_{h,i}^{\pm}$ plus the stabilization term in (165) (see, [60, 84]):

$$\|q_h\|^2_{\Omega_h^{\pm}} \leq C\left(\|q_h\|^2_{\Omega_{h,i}^{\pm}} + J_h^{\pm}(q_h, q_h)\right), \tag{169}$$

with some constant C independent of the position of Γ and h. We note that (169) holds also for discontinuous finite elements.

Consider now

$$q_\mu = \begin{cases} \mu_- |\Omega^-|^{-1} \in Q_h^- \\ -\mu_+ |\Omega^+|^{-1} \in Q_h^+. \end{cases}$$

Note that q_μ satisfies the orthogonality condition imposed for elements from $Q_h^{\pm}$, and hence $\mathrm{span}\{q_\mu\}$ is a subspace in $Q_h^{\pm}$. Using a trick from [78], we decompose arbitrary $q_h \in Q_h^{\pm}$ into a component collinear with q_μ and the orthogonal complement in each phase:

$$q_h = q_1 + q_0, \quad \text{with } q_1 \in \mathrm{span}\{q_\mu\}, \quad \text{and } \ (q_0^-, 1)_{\Omega_{h,i}^-} = (q_0^+, 1)_{\Omega_{h,i}^+} = 0.$$

Thus, q_1 and q_0 are orthogonal with respect to L^2 product in the inner domains $\Omega_{h,i}^{\pm}$. Next, we let $q^{\pm} = \mu_{\pm}^{-\frac{1}{2}} q_0^{\pm}$ in (168) and for $\mathbf{v}_h^{\pm} \in V_h$ given by (168) consider $\mathbf{v}_h^0 = \mu_-^{\frac{1}{2}} \mathbf{v}_h^- + \mu_+^{\frac{1}{2}} \mathbf{v}_h^+ \in V_h$. Then after applying (169) and summing up, the relations in (168) become

$$\begin{gathered} \mu_-^{-1} \|q_0^-\|^2_{\Omega_h^-} + \mu_+^{-1} \|q_0^+\|^2_{\Omega_h^+} \leq C \left((q_0^-, \nabla \cdot \mathbf{v}_h^0)_{\Omega^-} + (q_0^+, \nabla \cdot \mathbf{v}_h^0)_{\Omega^+} + b_p(q_0, q_0)\right), \\ \|\mu^{\frac{1}{2}} \nabla \mathbf{v}_h^0\|_{\Omega} \leq C_0 \left(\mu_-^{-1} \|q_0^-\|^2_{\Omega_h^-} + \mu_+^{-1} \|q_0^+\|^2_{\Omega_h^+}\right)^{\frac{1}{2}}, \end{gathered} \tag{170}$$

with C from (169) and $C_0 = \max\{C_-^{-1}, C_+^{-1}\}$, both of which are independent of $\mu_{\pm}$ and how Γ

overlaps the background mesh. In (170), we also used the fact that supports of $\mathbf{v}^-$ and $\mathbf{v}^+$ do not overlap. Since $\mathrm{supp}(\mathbf{v}_h^\pm) \subset \Omega^\pm$ and $q_1^\pm$ are constant in $\Omega^\pm$, integration by parts shows that

$$(q_1^\pm, \nabla \cdot \mathbf{v}_h^0)_{\Omega_h^\pm} = 0. \tag{171}$$

Next, we need the following result from Lemma 5.1 in [55]: For all $h \le h_0$ there exists $\mathbf{v}_h^1 \in V_h$ such that

$$\begin{aligned} \mu_-^{-1}\|q_1^-\|_{\Omega_h^-}^2 + \mu_+^{-1}\|q_1^+\|_{\Omega_h^+}^2 &= (q_1, \nabla \cdot \mathbf{v}_h^1)_{\Omega^-} + (q_1, \nabla \cdot \mathbf{v}_h^1)_{\Omega^+}, \\ \|\mu^{\frac{1}{2}} \nabla \mathbf{v}_h^1\|_\Omega &\le C_1 \left(\mu_-^{-1}\|q_1^-\|_{\Omega_h^-}^2 + \mu_+^{-1}\|q_1^+\|_{\Omega_h^+}^2\right)^{\frac{1}{2}}, \end{aligned} \tag{172}$$

with $h_0 > 0$ and $C_1 > 0$ independent of $\mu_\pm$ and how Γ overlaps the background mesh. The above result follows from the classical inf-sup stability condition for $\mathbf{P}_2 - P_1$ Taylor–Hood elements and a simple scaling and interpolation argument. See [55] for details.

As the next step, set $\mathbf{v}_h = \tau \mathbf{v}_h^0 + \mathbf{v}_h^1$ with some $\tau > 0$ and proceed with calculations using (171), (170), (172), and the Cauchy-Schwartz inequality:

$$\begin{aligned} &(q_h^-, \nabla \cdot \mathbf{v}_h)_{\Omega^-} + (q_h^+, \nabla \cdot \mathbf{v}_h)_{\Omega^+} \\ &\quad = (q_1^-, \nabla \cdot \mathbf{v}_h^1)_{\Omega^-} + (q_1^+, \nabla \cdot \mathbf{v}_h^1)_{\Omega^+} + \tau (q_0^-, \nabla \cdot \mathbf{v}_h^0)_{\Omega^-} + \tau (q_0^+, \nabla \cdot \mathbf{v}_h^0)_{\Omega^+} \\ &\qquad + (q_0^-, \nabla \cdot \mathbf{v}_h^1)_{\Omega^-} + (q_0^+, \nabla \cdot \mathbf{v}_h^1)_{\Omega^+} \\ &\quad \ge \mu_-^{-1}\|q_1^-\|_{\Omega_h^-}^2 + \mu_+^{-1}\|q_1^+\|_{\Omega_h^+}^2 + \tau C^{-1}\left(\mu_-^{-1}\|q_0^-\|_{\Omega_h^-}^2 + \mu_+^{-1}\|q_0^+\|_{\Omega_h^+}^2\right) - \tau b_p(q_0, q_0) \\ &\qquad - \left(\mu_-^{-1}\|q_0^-\|_{\Omega_h^-}^2 + \mu_+^{-1}\|q_0^+\|_{\Omega_h^+}^2\right)^{\frac{1}{2}} d^{\frac{1}{2}} \|\mu^{\frac{1}{2}} \nabla \mathbf{v}_h^1\|_\Omega \\ &\quad \ge \mu_-^{-1}\|q_1^-\|_{\Omega_h^-}^2 + \mu_+^{-1}\|q_1^+\|_{\Omega_h^+}^2 + \tau C^{-1}\left(\mu_-^{-1}\|q_0^-\|_{\Omega_h^-}^2 + \mu_+^{-1}\|q_0^+\|_{\Omega_h^+}^2\right) - \tau b_p(q_0, q_0) \\ &\qquad - \left(\mu_-^{-1}\|q_0^-\|_{\Omega_h^-}^2 + \mu_+^{-1}\|q_0^+\|_{\Omega_h^+}^2\right)^{\frac{1}{2}} C_1 d^{\frac{1}{2}} \left(\mu_-^{-1}\|q_1^-\|_{\Omega_h^-}^2 + \mu_+^{-1}\|q_1^+\|_{\Omega_h^+}^2\right)^{\frac{1}{2}} \\ &\quad \ge \frac{1}{2}\left(\mu_-^{-1}\|q_1^-\|_{\Omega_h^-}^2 + \mu_+^{-1}\|q_1^+\|_{\Omega_h^+}^2\right) + \left(\frac{\tau}{C} - \frac{C_1^2 d}{2}\right)\left(\mu_-^{-1}\|q_0^-\|_{\Omega_h^-}^2 + \mu_+^{-1}\|q_0^+\|_{\Omega_h^+}^2\right) - \tau b_p(q_0, q_0). \end{aligned}$$

We set τ such that $\frac{\tau}{C} - \frac{C_1^2 d}{2} = \frac{1}{2}$ and note that $b_p(q_0, q_0) = b_p(q_h, q_h)$. Using this and the orthogonality condition for q_0, we get

$$
\begin{aligned}
&(q_h, \nabla \cdot \mathbf{v}_h)_{\Omega^-} + (q_h, \nabla \cdot \mathbf{v}_h)_{\Omega^+} \\
&\quad \geq \frac{1}{2}\left(\mu_-^{-1}\|q_1^-\|^2_{\Omega_h^-} + \mu_+^{-1}\|q_1^+\|^2_{\Omega_h^+}\right) + \frac{1}{2}\left(\mu_-^{-1}\|q_0^-\|^2_{\Omega_h^-} + \mu_+^{-1}\|q_0^+\|^2_{\Omega_h^+}\right) - \tau b_p(q_h, q_h) \\
&\quad \geq \frac{1}{2}\left(\mu_-^{-1}\|q_1^-\|^2_{\Omega_{h,i}^-} + \mu_+^{-1}\|q_1^+\|^2_{\Omega_{h,i}^+}\right) + \frac{1}{2}\left(\mu_-^{-1}\|q_0^-\|^2_{\Omega_h^-} + \mu_+^{-1}\|q_0^+\|^2_{\Omega_{h,i}^+}\right) - \tau b_p(q_h, q_h) \qquad (173) \\
&\quad = \frac{1}{2}\left(\mu_-^{-1}\|q_h^-\|^2_{\Omega_{h,i}^-} + \mu_+^{-1}\|q_h^+\|^2_{\Omega_{h,i}^+}\right) - \tau b_p(q_h, q_h) \\
&\quad \geq \frac{1}{2C}\left(\mu_-^{-1}\|q_h^-\|^2_{\Omega_h^-} + \mu_+^{-1}\|q_h^+\|^2_{\Omega_h^+}\right) - \left(\tau + \frac{1}{2}\right) b_p(q_h, q_h).
\end{aligned}
$$

Using $(q_0^\pm, q_1^\pm)_{\Omega_{h,i}^\pm} = 0$, $|\Omega_h^\pm \setminus \Omega_{h,i}^\pm| \leq c\,h$ and so $\|q_1^\pm\|_{\Omega_h^\pm \setminus \Omega_{h,i}^\pm} \leq c h^{\frac{1}{2}} \|q_1^\pm\|_{\Omega_h^\pm}$, we estimate

$$
\begin{aligned}
&|\mu_-^{-1}(q_0^-, q_1^-)_{\Omega_h^-} + \mu_+^{-1}(q_0^+, q_1^+)_{\Omega_h^+}| \\
&\qquad\qquad \leq c\,h^{\frac{1}{2}}\left(\mu_-^{-1}\|q_0^-\|^2_{\Omega_h^-} + \mu_+^{-1}\|q_0^+\|^2_{\Omega_h^+}\right)^{\frac{1}{2}}\left(\mu_-^{-1}\|q_1^-\|^2_{\Omega_h^-} + \mu_+^{-1}\|q_1^+\|^2_{\Omega_h^+}\right)^{\frac{1}{2}}. \qquad (174)
\end{aligned}
$$

From (170), (172), and (174), we also get the following upper bound for $\mathbf{v}_h$,

$$
\begin{aligned}
\|\mu^{\frac{1}{2}}\nabla \mathbf{v}_h\|^2_\Omega &\leq 2(\|\mu^{\frac{1}{2}}\tau\nabla \mathbf{v}_h^0\|^2_\Omega + \|\mu^{\frac{1}{2}}\nabla \mathbf{v}_h^1\|^2_\Omega) \\
&\leq 2\tau^2 C_0^2\left(\mu_-^{-1}\|q_0^-\|^2_{\Omega_h^-} + \mu_+^{-1}\|q_0^+\|^2_{\Omega_h^+}\right) + 2C_1^2\left(\mu_-^{-1}\|q_1^-\|^2_{\Omega_h^-} + \mu_+^{-1}\|q_1^+\|^2_{\Omega_h^+}\right) \qquad (175) \\
&\leq \frac{2\max\{\tau^2 C_0^2, C_1^2\}}{1 - c\,h^{\frac{1}{2}}}\left(\mu_-^{-1}\|q_h^-\|^2_{\Omega_h^-} + \mu_+^{-1}\|q_h^+\|^2_{\Omega_h^+}\right).
\end{aligned}
$$

The assertion of the lemma follows from (173) and (175) after simple calculations.

□

The next lemma shows the uniform coercivity of the symmetric form $a_h(\mathbf{u}_h, \mathbf{v}_h)$ in (160) on $V_h^\pm \times V_h^\pm$.

Lemma 2.2 *If $\gamma = O(1)$ in (162) is sufficiently large, then it holds*

$$
a_h(\mathbf{u}_h, \mathbf{u}_h) \geq C\left(\mu_-\|\mathbf{D}(\mathbf{u}_h^-)\|^2_{\Omega_h^-} + \mu_+\|\mathbf{D}(\mathbf{u}_h^+)\|^2_{\Omega_h^+} + h^{-1}\|\{\mu\}[\mathbf{u}_h \cdot \mathbf{n}]\|^2_\Gamma + f\|[\mathbf{P}\mathbf{u}_h]\|^2_\Gamma\right) \qquad (176)
$$

$\forall\ \mathbf{u}_h \in V_h^{\pm}$, *with* $C > 0$ *independent of* $\mu_{\pm}$, h, f, *and the position of* Γ *with respect to the background mesh.*

Proof: For the proof, we need the local trace inequality in $T \in \mathcal{T}_h^{\Gamma}$ (see, e.g. [39, 41]):

$$\|v\|_{T\cap\Gamma} \leq C(h_T^{-\frac{1}{2}}\|v\|_T + h_T^{\frac{1}{2}}\|\nabla v\|_T), \qquad \forall\ v \in H^1(T), \tag{177}$$

with a constant C independent of v, T, how Γ intersects T, and $h_T < h_0$ for some arbitrary but fixed h_0. We also need the following estimate

$$\|\mathbf{D}(\mathbf{v}_h^{\pm})\|^2_{L^2(\Omega_h^{\pm})} \leq C(\|\mathbf{D}(\mathbf{v}_h^{\pm})\|^2_{L^2(\Omega^{\pm})} + \mathbf{J}^{\pm}(\mathbf{v}_h^{\pm}, \mathbf{v}_h^{\pm})\,), \tag{178}$$

which follows from (169) by applying it componentwise and further using FE inverse inequality (note h^{-2} scaling in the definition of $\mathbf{J}^{\pm}$ in (163)). Applying (177), finite element inverse inequalities and (178), we can bound the interface term

$$\begin{aligned}
\langle\{\mu\mathbf{n}^T\mathbf{D}(\mathbf{v}_h)\mathbf{n}\},[\mathbf{u}_h\cdot\mathbf{n}]\rangle_{\Gamma} &= \langle\mu_-\mathbf{n}^T\mathbf{D}(\mathbf{v}_h^-)\mathbf{n}, [\mathbf{u}_h\cdot\mathbf{n}]\rangle_{\Gamma} \\
&\leq \sum_{T\in\mathcal{T}_h^{\Gamma}}\left[\frac{h_T\delta}{2}\|\mu_-^{\frac{1}{2}}\mathbf{n}^T\mathbf{D}(\mathbf{v}_h^-)\mathbf{n}\|^2_{T\cap\Gamma} + \frac{1}{2h_T\delta}\|\mu_-^{\frac{1}{2}}[\mathbf{u}_h\cdot\mathbf{n}]\|^2_{T\cap\Gamma}\right] \\
&\leq \frac{\delta}{2}\|\mu_-^{\frac{1}{2}}\mathbf{n}^T\mathbf{D}(\mathbf{v}_h^-)\mathbf{n}\|^2_{\Omega_h^-} + \frac{1}{h_T\delta}\{\mu\}|[\mathbf{u}_h\cdot\mathbf{n}]|^2_{\Gamma}, \quad \forall\ \delta > 0,\ \mathbf{u}_h, \mathbf{v}_h \in V_h^{\pm}.
\end{aligned}$$

This estimate with $\mathbf{v}_h = \mathbf{u}_h$ and with $\delta > 0$ sufficiently small, together with the definition of the bilinear form $a_h(\mathbf{u}_h, \mathbf{u}_h)$, allows to show its coercivity. □

We further need the continuity result for the velocity stabilization form contained in the next lemma.

Lemma 2.3 *It holds*

$$a_p(\mathbf{v}_h, \mathbf{v}_h) \leq C\left(\mu_-\|\mathbf{D}(\mathbf{v}_h^-)\|^2_{\Omega_h^-} + \mu_+\|\mathbf{D}(\mathbf{v}_h^+)\|^2_{\Omega_h^+}\right) \qquad \forall\ \mathbf{v}_h \in V_h^{\pm},$$

with $C > 0$ independent of $\mu_\pm$, h, and the position of Γ in the background mesh.

Proof: For any $\mathbf{v} = \mathbf{v}_h^- \in V_h^-$, facet $e \in \mathcal{E}_h^{\Gamma,-}$ and the corresponding patch ω_e formed by two tetrahedra T_1 and T_2, it holds

$$\|\mathbf{v}_1^e - \mathbf{v}_2^e\|_{\omega_e}^2 = \|\mathbf{v}_1 - \mathbf{v}_2^e\|_{T_1}^2 + \|\mathbf{v}_1^e - \mathbf{v}_2\|_{T_2}^2 \leq (1+c)\|\mathbf{v}_1 - \mathbf{v}_2^e\|_{T_1}^2,$$

where the constant c depends only on shape regularity of the tetrahedra, since $\mathbf{v}_1^e - \mathbf{v}_2$ on T_2 is the canonical polynomial extension of $\mathbf{v}_1 - \mathbf{v}_2^e$ from T_1.

Now, we need the following local Korn's inequality:

$$\|\nabla \mathbf{v}\|_T \leq C\|\mathbf{D}(\mathbf{v})\|_T, \quad \forall\ \mathbf{v} \in H^1(T)^d, \ \text{ s.t. } \mathbf{v} = 0 \text{ on any face of } T \in \mathcal{T}_h, \tag{179}$$

where C depends only on shape regularity of T. The result in (179) follows from eq. (3.3) in [12] and the observation that vector fields vanishing on any face T support only zero rigid motions. A simple scaling argument also proves the local Poincare inequality:

$$\|\mathbf{v}\|_T \leq Ch_T^2\|\nabla \mathbf{v}\|_T, \quad \forall\ \mathbf{v} \in H^1(T)^d, \ \text{ s.t. } \mathbf{v} = 0 \text{ on any face of } T \in \mathcal{T}_h, \tag{180}$$

where C depends only on shape regularity of T. Applying (179), (180) and triangle inequalities on T_1 for $\mathbf{v}_1 - \mathbf{v}_2^e$ which vanishes on e (a face of T_1), we obtain:

$$\begin{aligned}\|\mathbf{v}_1 - \mathbf{v}_2^e\|_{T_1}^2 &\leq C_p h^2 \|\mathbf{D}(\mathbf{v}_1 - \mathbf{v}_2^e)\|_{T_1}^2 \leq 2C_p h^2(\|\mathbf{D}\mathbf{v}_1\|_{T_1}^2 + \|\mathbf{D}\mathbf{v}_2^e\|_{T_1}^2) \\ &\leq 2C_p h^2(\|\mathbf{D}\mathbf{v}_1\|_{T_1}^2 + c\,\|\mathbf{D}\mathbf{v}_2\|_{T_2}^2),\end{aligned} \tag{181}$$

where for the last inequality we again use shape regularity and the fact that $\mathbf{D}\mathbf{v}_2^e = (\mathbf{D}\mathbf{v}_2)^e$. Thus, we see that $\|\mathbf{v}_1^e - \mathbf{v}_2^e\|_{\omega_e}^2 \leq c\,h^2\|\mathbf{D}\mathbf{v}\|_{\omega_e}^2$, with some c depending only on shape regularity. Summing up over all $e \in \mathcal{E}_h^{\Gamma,-}$ leads to the required upper bound for $\mathbf{J}_h^-(\mathbf{v},\mathbf{v})$: $\mathbf{J}_h^-(\mathbf{v},\mathbf{v}) \leq C\|\mathbf{D}(\mathbf{v})\|_{\Omega_h^-}$. Repeating the same argument for the edges in $\mathcal{E}_h^{\Gamma,+}$ and summing up the two bounds scaled by

viscosity coefficients proves the lemma.

□

The finite element problem (159) can be equivalently formulated as follows: Find $\{\mathbf{u}_h, p_h\} \in V_h^{\pm} \times Q_h^{\pm}$ such that

$$\mathcal{A}(\mathbf{u}_h, p_h; \mathbf{v}_h, q_h) = r_h(\mathbf{v}_h), \quad \forall\, \{\mathbf{v}_h, q_h\} \in V_h^{\pm} \times Q_h^{\pm} \tag{182}$$

with

$$\mathcal{A}(\mathbf{u}_h, p_h; \mathbf{v}_h, q_h) = a_h(\mathbf{u}_h, \mathbf{v}_h) + b_h(\mathbf{v}_h, p_h) - b_h(\mathbf{u}_h, q_h) + b_p(p_h, q_h).$$

Lemmas 2.1–2.3 enable us to show the inf-sup stability of the bilinear form $\mathcal{A}$. The stability result is formulated using the following composite norm:

$$\|\mathbf{v}, q\|^2 := \mu_- \|\mathbf{D}(\mathbf{v}^-)\|^2_{\Omega_h^-} + \mu_+ \|\mathbf{D}(\mathbf{v}^+)\|^2_{\Omega_h^+} + h^{-1}\|\{\mu\}[\mathbf{v}\cdot\mathbf{n}]\|^2_{\Gamma} + f\|[\mathbf{P}\mathbf{v}]\|^2_{\Gamma} + \mu_-^{-1}\|q^-\|^2_{\Omega_h^-} + \mu_+^{-1}\|q^+\|^2_{\Omega_h^+}$$

for $\mathbf{v} \in V_h^{\pm},\ q \in Q_h^{\pm}$.

Theorem 2.4 *There exists $h_0 > 0$ such that for all $h < h_0$ it holds*

$$\sup_{\{\mathbf{v}_h, q_h\} \in V_h^{\pm} \times Q_h^{\pm}} \frac{\mathcal{A}(\mathbf{u}_h, p_h; \mathbf{v}_h, q_h)}{\|\mathbf{v}_h, q_h\|} \geq C\, \|\mathbf{u}_h, p_p\|, \quad \forall\, \{\mathbf{u}_h, p_h\} \in V_h^{\pm} \times Q_h^{\pm},$$

with $h_0 > 0$ and $C > 0$ independent of $\mu_{\pm}$, h, f, and the position of Γ in the background mesh.

Proof: For a given $p_h \in Q_h^{\pm}$, Lemma 2.1 implies the existence of such $\mathbf{w}_h \in V_h$ that

$$b_h(\mathbf{w}_h, p_h) + b_p(p_h, q_h) \geq c\, \left(\mu_-^{-1}\|p_h^-\|^2_{\Omega_h^-} + \mu_+^{-1}\|p_h^+\|^2_{\Omega_h^+}\right) \tag{183}$$

and

$$\|\mu^{\frac{1}{2}} \nabla \mathbf{w}_h\|^2_{\Omega} \leq C\, \left(\mu_-^{-1}\|p_h^-\|^2_{\Omega_h^-} + \mu_+^{-1}\|p_h^+\|^2_{\Omega_h^+}\right), \tag{184}$$

with some positive c, C independent of μ and how Γ overlaps the background mesh. Next, we extend the finite element function $\mathbf{w}_h \in V_h$ to the element of the product space $\widehat{\mathbf{w}}_h \in V_h^{\pm}$ by setting $\widehat{\mathbf{w}}_h^{\pm} = \mathbf{w}_h|_{\Omega_h^{\pm}} \in V_h^{\pm}$. We let $\mathbf{v}_h = \mathbf{u}_h + \tau \widehat{\mathbf{w}}_h$ for some $\tau > 0$ and $q_h = p_h$. Using the definition of the form $\mathcal{A}$ and (183), we calculate

$$\begin{aligned}\mathcal{A}(\mathbf{u}_h, p_h; \mathbf{v}_h, q_h) &= a_h(\mathbf{u}_h, \mathbf{u}_h) + \tau a_h(\mathbf{u}_h, \widehat{\mathbf{w}}_h) + \tau b_h(\widehat{\mathbf{w}}_h, p_h) + b_p(p_h, p_h) \\ &\geq \frac{1}{2} a_h(\mathbf{u}_h, \mathbf{u}_h) - \frac{\tau^2}{2} a_h(\widehat{\mathbf{w}}_h, \widehat{\mathbf{w}}_h) + \min\{\tau, 1\}\, c \left(\mu_-^{-1} \|p_h^-\|^2_{\Omega_h^-} + \mu_+^{-1} \|p_h^+\|^2_{\Omega_h^+} \right),\end{aligned} \tag{185}$$

where we used the Cauchy-Schwartz inequality:

$$\tau a_h(\mathbf{u}_h, \widehat{\mathbf{w}}_h) \leq \tau |a_h(\mathbf{u}_h, \mathbf{u}_h)|^{\frac{1}{2}} |a_h(\widehat{\mathbf{w}}_h, \widehat{\mathbf{w}}_h)|^{\frac{1}{2}} \leq \frac{1}{2} a_h(\mathbf{u}_h, \mathbf{u}_h) + \frac{\tau^2}{2} a_h(\widehat{\mathbf{w}}_h, \widehat{\mathbf{w}}_h).$$

Note that it holds $[\widehat{\mathbf{w}}_h \cdot \mathbf{n}] = 0$ and $[\mathbf{P}\widehat{\mathbf{w}}_h] = 0$ on Γ. Since all Nitsche and 'friction' terms in $a_h(\widehat{\mathbf{w}}_h, \widehat{\mathbf{w}}_h)$ vanish, the results of the Lemma 2.3 and estimate (184) imply the upper bound

$$a_h(\widehat{\mathbf{w}}_h, \widehat{\mathbf{w}}_h) \leq C \, \|\mu^{\frac{1}{2}} \nabla \widehat{\mathbf{w}}_h\|^2_{\Omega} \leq C \left(\mu_-^{-1} \|p_h^-\|^2_{\Omega_h^-} + \mu_+^{-1} \|p_h^+\|^2_{\Omega_h^+} \right).$$

Using it in (185) and choosing $\tau > 0$ small enough, but independent of all problem parameters, leads us to the lower bound

$$\mathcal{A}(\mathbf{u}_h, p_h; \mathbf{v}_h, q_h) \geq \frac{1}{2} a_h(\mathbf{u}_h, \mathbf{u}_h) + c \left(\mu_-^{-1} \|p_h^-\|^2_{\Omega_h^-} + \mu_+^{-1} \|p_h^+\|^2_{\Omega_h^+} \right) \geq c \, \|\mathbf{u}_h, p_h\|^2, \tag{186}$$

with some $c > 0$ independent of $\mu_{\pm}$, h, and the position of Γ in the background mesh. For the last inequality, we used (176).

Finally, by the construction of $\mathbf{v}_h$ and thanks to (184) it is straightforward to see the upper bound:

$$\|\mathbf{v}_h, q_h\| \leq c \, \|\mathbf{u}_h, p_h\|.$$

This combined with (186) proves the theorem.

□

The stability of the finite element solution in the composite norm immediately follows from (182) and Theorem 2.4:

$$\|\mathbf{u}_h, p_h\| \leq C \sup_{\{\mathbf{v}_h, q_h\} \in V_h^{\pm} \times Q_h^{\pm}} \frac{|r_h(\mathbf{v}_h)|}{\|\mathbf{v}_h, q_h\|},$$

where on the right-hand side we see the dual norm of the functional r_h and constant C, which is independent of the mesh size h, the ratio of the viscosity coefficients $\mu_{\pm}$, and the position of Γ in the background mesh.

2.4 Error analysis

The stability result shown in Sec. 2.3 and interpolation properties of finite elements enable us to prove optimal order convergence with uniformly bounded constants.

We assume in this section that the solution to problem (140)–(147) is piecewise smooth in the following sense: $\mathbf{u}^{\pm} \in H^{k+2}(\Omega^{\pm})^d$ and $p^{\pm} \in H^{k+1}(\Omega^{\pm})$. For the sake of notation, we define the following semi-norm

$$\|\mathbf{u}, p\|_* = \left(\mu_- |\mathbf{u}^-|^2_{H^{k+2}(\Omega^-)} + \mu_+ |\mathbf{u}^+|^2_{H^{k+2}(\Omega^+)} + \mu_-^{-1} |p^-|^2_{H^{k+1}(\Omega^-)} + \mu_+^{-1} |p^+|^2_{H^{k+1}(\Omega^+)}\right)^{\frac{1}{2}}. \quad (187)$$

Since we assume Γ to be at least Lipschitz, there exist extensions $\mathcal{E}\mathbf{u}^{\pm}$ and $\mathcal{E}p^{\pm}$ of the solution from each phase to $\mathbb{R}^d$ such that $\mathcal{E}\mathbf{u}^{\pm} \in H^{k+2}(\mathbb{R}^d)^3$, $\mathcal{E}p^{\pm} \in H^{k+1}(\mathbb{R}^d)$. The corresponding norms are bounded as follows

$$\|\mathcal{E}\mathbf{u}^{\pm}\|_{H^{k+2}(\mathbb{R}^d)} \leq C \|\mathbf{u}^{\pm}\|_{H^{k+2}(\Omega^{\pm})}, \quad \|\mathcal{E}p^{\pm}\|_{H^{k+1}(\mathbb{R}^d)} \leq C \|p^{\pm}\|_{H^{k+1}(\Omega^{\pm})} \quad (188)$$

See [94]. Denote by $I_h\mathbf{u}^{\pm}$ the Scott-Zhang interpolants of $\mathcal{E}\mathbf{u}^{\pm}$ onto $V_h^{\pm}$ and $I_h\mathbf{u} := \{I_h\mathbf{u}^-, I_h\mathbf{u}^+\}$. Same notation $I_h p^{\pm}$ will be used for the Scott-Zhang interpolants of $\mathcal{E}p^{\pm}$ onto $Q_h^{\pm}$. For the pressure interpolants, we can always satisfy the orthogonality condition of $Q_h^{\pm}$ by choosing a suitable additive constant in the definition of p.

Applying trace inequality (177), standard approximation properties of I_h, and bounds (188), one obtains the approximation property in the product norm:

$$\|\mathbf{u} - I_h\mathbf{u}, p - I_h p\| \le C\, h^{k+1}\|\mathbf{u}, p\|_*. \tag{189}$$

The following continuity result is the immediate consequence of the Cauchy–Schwatz inequality:

$$\begin{aligned}\mathcal{A}(\mathbf{u} - I_h\mathbf{u}, p - I_h p;\, \mathbf{v}_h, q_h) &\le C\, \|\mathbf{u} - I_h\mathbf{u}, p - I_h p\|\|\mathbf{v}_h, q_h\| \\ &+ |\langle\{\mu\mathbf{n}^T\mathbf{D}(\mathbf{v}_h)\mathbf{n}\}, [(\mathbf{u} - I_h\mathbf{u})\cdot\mathbf{n}]\rangle_\Gamma + \langle\{\mu\mathbf{n}^T\mathbf{D}(\mathbf{u} - I_h\mathbf{u})\mathbf{n}\}, [\mathbf{v}_h\cdot\mathbf{n}]\rangle_\Gamma|, \end{aligned}\tag{190}$$

for all $\{\mathbf{v}_h, q_h\} \in V_h^\pm \times Q_h^\pm$. The last term on the right-hand side in (190) needs a special treatment. Applying the Cauchy–Schwatz, inequalities (177) and (178), FE inverse inequalities and approximation properties of the interpolants, we get

$$\begin{aligned}|\langle\{\mu\mathbf{n}^T\mathbf{D}(\mathbf{v}_h)\mathbf{n}\}, [(\mathbf{u} - I_h\mathbf{u})\cdot\mathbf{n}]\rangle_\Gamma| &\le C\, h^{k+1}\|\mathbf{u}, 0\|_*\|\mathbf{v}_h, 0\|, \\ |\langle\{\mu\mathbf{n}^T\mathbf{D}(\mathbf{u} - I_h\mathbf{u})\mathbf{n}\}, [\mathbf{v}_h\cdot\mathbf{n}]\rangle_\Gamma| &\le C\, h^{k+1}\|\mathbf{u}, 0\|_*\|\mathbf{v}_h, 0\|. \end{aligned}\tag{191}$$

The consistency of the stabilization term is formalized in the estimates that follow from [60, lemma 5.5]: For $p^- \in H^{k+1}(\Omega^-)$, $\mathbf{u}^- \in H^{k+2}(\Omega^-)^d$, it holds

$$J_h^-(p^-, p^-) \le C\, h^{2k+2}\|p^-\|^2_{H^{k+1}(\Omega^-)}, \quad \mathbf{J}_h^-(\mathbf{u}^-, \mathbf{u}^-) \le C\, h^{2k+2}\|\mathbf{u}^-\|^2_{H^{k+2}(\Omega^-)}. \tag{192}$$

The above estimates and the stability of the interpolants also imply

$$\begin{aligned}J_h^-(p^- - I_h p^-, p^- - I_h p^-) &\le C\, h^{2k+2}|p^-|^2_{H^{k+1}(\Omega^-)}, \\ \mathbf{J}_h^-(\mathbf{u}^- - I_h\mathbf{u}^-, \mathbf{u}^- - I_h\mathbf{u}^-) &\le C\, h^{2k+2}|\mathbf{u}^-|^2_{H^{k+2}(\Omega^-)}. \end{aligned}\tag{193}$$

Similar estimates to (192), (193) hold for J_h^+ and $\mathbf{J}_h^+$ with $p^+ \in H^{k+1}(\Omega^+)$, $\mathbf{u}^+ \in H^{k+2}(\Omega^+)^d$,

which can be combined with suitable weights to yield

$$b_p(p - I_h p, p - I_h p) + a_p(\mathbf{u} - I_h \mathbf{u}, \mathbf{u} - I_h \mathbf{u}) \leq C\, h^{2k+2} \|\mathbf{u}, p\|_*^2. \tag{194}$$

Denote the error functions by $\mathbf{e}_u = \mathcal{E}\mathbf{u} - \mathbf{u}_h$ and $e_p = \mathcal{E}p - p_h$. Galerkin orthogonality holds up to the consistency terms

$$\mathcal{A}(\mathbf{e}_u, e_p;\, \mathbf{v}_h, q_h) = b_p(p - I_h p, q_h) + a_p(\mathbf{u} - I_h \mathbf{u}, \mathbf{v}_h), \tag{195}$$

for all $\mathbf{v}_h \in V_h^{\pm}$ and $q_h \in Q_h^{\pm}$.

The result of Lemma 2.2, (194) and the trivial bound $b_p(q_h, q_h) \leq C\|\mathbf{0}, q_h\|^2$ imply the following estimate for the consistency term on the right-hand side of (195):

$$\begin{aligned} &|b_p(p - I_h p, q_h) + a_p(\mathbf{u} - I_h \mathbf{u}, \mathbf{v}_h)| \\ &\quad \leq |b_p(p - I_h p, p - I_h p)|^{\frac{1}{2}} |b_p(q_h, q_h)|^{\frac{1}{2}} + |a_p(\mathbf{u} - I_h \mathbf{u}, \mathbf{u} - I_h \mathbf{u})|^{\frac{1}{2}} |a_p(\mathbf{v}_h, \mathbf{v}_h)|^{\frac{1}{2}} \\ &\quad \leq C\, h^{k+1} \|\mathbf{u}, p\|_* \|\mathbf{v}_h, q_h\|, \end{aligned} \tag{196}$$

The optimal order error estimate in the energy norm is given in the next theorem.

Theorem 2.5 *For sufficiently regular* $\mathbf{u}, p$ *solving problem* (140)–(147) *and* $\mathbf{u}_h, p_h$ *solving problem* (159)*, the following error estimate holds:*

$$\|\mathbf{u} - \mathbf{u}_h, p - p_h\| \leq\, C h^{k+1} \|\mathbf{u}, p\|_*, \tag{197}$$

with a constant C *independent of* h*, the values of viscosities* $\mu_{\pm}$*, slip coefficient* $f \geq 0$*, and the position of* Γ *with respect to the triangulation* $\mathcal{T}_h$*.*

Proof: This result follows by standard arguments (see, for example, section 2.3 in [27]) from the inf-sup stability results of Theorem 2.4, continuity estimates (190) and (191), Galerkin orthogonality and consistency (195)–(196), and approximation properties (189). □

Remark 2.6 If we consider using isoparametric elements to handle numerical integration over cut cells (see section 2.2.1), then the Sobolev seminorms in the definition of $\|\mathbf{u}, p\|_*$ on the right-hand side in (197) should be replaced by the full Sobolev norms of the same order; see the error analysis of the isoparametric unfitted FEM in [61].

2.5 Numerical examples

The aim of the numerical results collected in this section is twofold: (i) support the theoretical results presented in Sec. 2.4 and (ii) provide evidence of the robustness of the proposed finite element approach with respect to the contrast in viscosity, slip coefficient value, and position of the interface relative to the fixed computational mesh.

For the averages in (156)-(157), we set $\alpha = 0$ and $\beta = 1$ for all the numerical experiments since we have $\mu_- \leq \mu_+$. Recall that this is the choice for the analysis carried out in Sec. 2.3 and 2.4. In addition, we set $\gamma_{\mathbf{u}}^{\pm} = 0.05$, $\gamma_p^{\pm} = 0.05$, and $\gamma = 40$. The value of all other parameters will depend on the specific test.

For all the results presented below, we will report the L^2 error and a weighted H^1 error for the velocity defined as

$$\left(2\mu_- \|D(\mathbf{u} - \mathbf{u}_h^-)\|^2_{L^2(\Omega^-)} + 2\mu_+ \|D(\mathbf{u} - \mathbf{u}_h^+)\|^2_{L^2(\Omega^+)}\right)^{\frac{1}{2}}, \tag{198}$$

and a weighted L^2 error for the pressure defined as

$$\left(\mu_-^{-1} \|p - p_h^-\|^2_{L^2(\Omega^-)} + \mu_+^{-1} \|p - p_h^+\|^2_{L^2(\Omega^+)}\right)^{\frac{1}{2}}. \tag{199}$$

2.5.1 2D tests

First, we perform a series of tests in 2D. For all the tests, the domain Ω is square $[-1, 1] \times [-1, 1]$ and interface Γ is a circle of radius $2/3$ centered at $\mathbf{c} = (c_1, c_2)$. Let $(x, y) = (\tilde{x} - c_1, \tilde{y} - c_2)$,

$(\tilde{x}, \tilde{y}) \in \Omega$. The exact solution we consider is given by:

$$p^- = (x - c_1)^3, \qquad p^+ = (x - c_1)^3 - \frac{1}{2}, \tag{200}$$

$$\mathbf{u}^- = g^-(x, y) \begin{bmatrix} -y \\ x \end{bmatrix}, \qquad \mathbf{u}^+ = g^+(x, y) \begin{bmatrix} -y \\ x \end{bmatrix}, \tag{201}$$

where

$$g^+(x, y) = \frac{3}{4\mu_+}(x^2 + y^2), \quad g^-(x, y) = \frac{3}{4\mu_-}(x^2 + y^2) + \frac{\mu_- - \mu_+}{3\mu_+\mu_-} + \frac{1}{f}.$$

The forcing terms $\mathbf{f}^-$ and $\mathbf{f}^+$ are found by plugging the above solution in (140). The surface tension coefficient σ is set to -0.5. The value of the other physical parameters will be specified for each test.

We impose a Dirichlet condition (142) on the entire boundary, where function $\mathbf{g}$ is found from $\mathbf{u}^+$ in (201).

Spatial convergence. First, we check the spatial accuracy of the finite element method described in Sec. 2.2. The aim is to validate our implementation of the method and support the theoretical findings in Sec. 2.4. For this purpose, we consider exact solution (200)-(201) with $\mathbf{c} = \mathbf{0}$ (i.e., interface Γ is a circle centered at the origin of the axes), viscosities $\mu_- = 1$ and $\mu_+ = 10$, and $f = 10$.

We consider structured meshes of quads with six levels of refinement. The initial triangulation has a mesh size $h = 1/2$ and all the other meshes are obtained by halving h till $h = 1/128$. We choose to use finite element pairs $\mathbf{Q}_2 - Q_1$. Fig. 3 shows the velocity vectors colored with the velocity magnitude and the pressure computed with mesh $h = 1/128$. Fig. 4 shows the L^2 error and weighted H^1 error (198) for the velocity and weighted L^2 error (199) for the pressure against the mesh size h. For the range of mesh sizes under consideration, we observe close to cubic convergence in the L^2 norm for the velocity and quadratic convergence in the weighted L^2 norm for the pressure and in the weighted H^1 norm for the velocity.

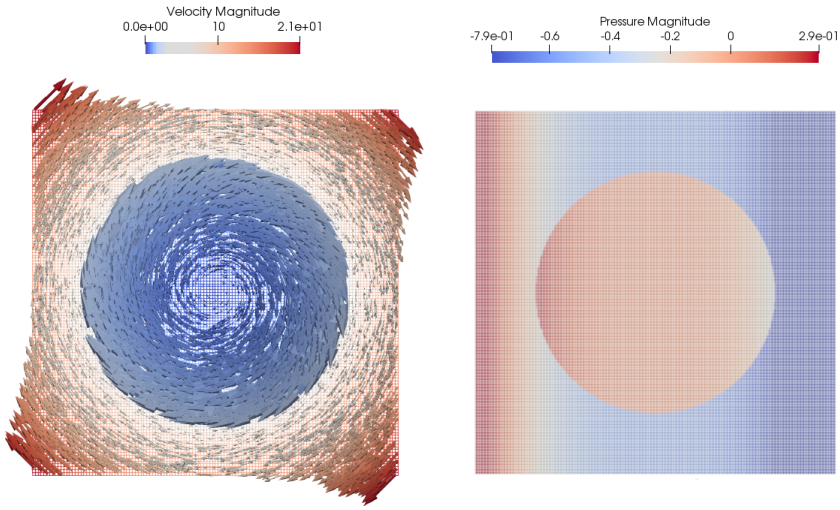

Figure 3: Approximation of exact solution (200)-(201) for $\mathbf{c} = \mathbf{0}$, $\mu_- = 1$, $\mu_+ = 10$, and $f = 10$, computed with mesh $h = 1/128$: velocity vectors colored with the velocity magnitude (left) and pressure (right).

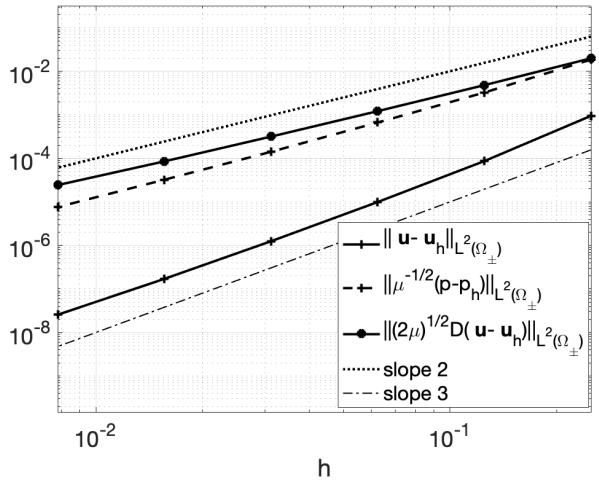

Figure 4: 2D test with $\mathbf{c} = \mathbf{0}$, $\mu_- = 1$, $\mu_+ = 10$, and $f = 10$: L^2 error and weighted H^1 error (198) for the velocity and weighted L^2 error (199) for the pressure against the mesh size h.

Robustness with respect to the viscosity contrast. The case of high contrast for the viscosities in a two-phase problem is especially challenging from the numerical point of view. To

test the robustness of our approach, we consider exact solution (200)-(201) and fix $\mu_- = 1$, while we let μ_+ vary from 1 to 10^8. We set $\mathbf{c} = \mathbf{0}$ and $f = 10$.

We consider one of the meshes adopted for the previous sets of simulations (with $h = 1/64$) and use again $\mathbf{Q}_2 - Q_1$ finite elements. Fig. 5 (left) shows the L^2 error and weighted H^1 error (198) for the velocity and weighted L^2 error (199) for the pressure against the value of μ_+. We observe that all the errors quickly reach a plateau as the μ_+/μ_- ratio increases, after initially decreasing. These results show that our approach is substantially robust with respect to the viscosity contrast μ_+/μ_-.

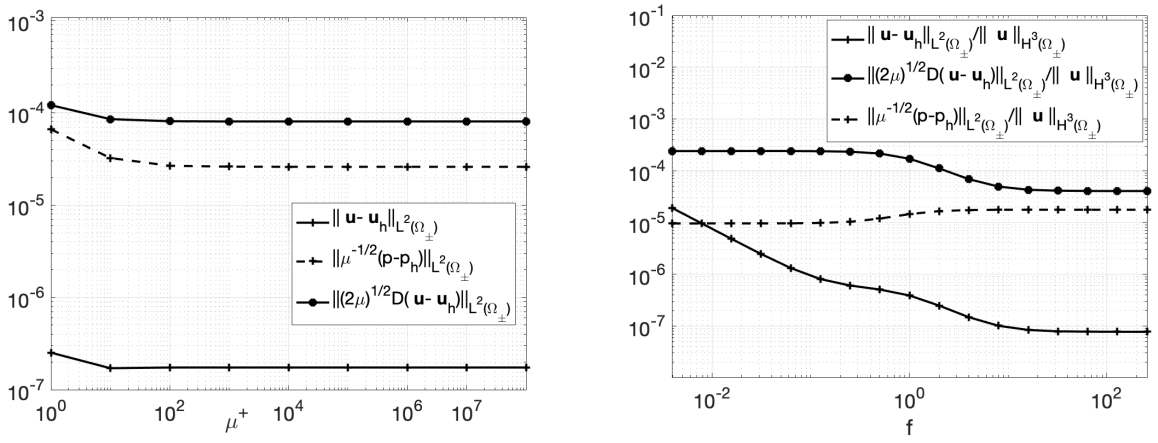

Figure 5: 2D test with $\mathbf{c} = \mathbf{0}$ and $\mu_- = 1$: L^2 error and weighted H^1 error (198) for the velocity and weighted L^2 error (199) for the pressure against the value of μ_+ (left) and corresponding scaled norms against the value of the slip coefficient f (right).

Robustness with respect to the slip coefficient. For the next set of simulations, we consider exact solution (200)-(201) and let the slip coefficient f in (145)-(146) vary from 1/256 to 256. Notice that the larger f becomes, the closer the two-phase problem gets to the homogeneous model. The other parameters are set as follows: $\mathbf{c} = \mathbf{0}$, $\mu_- = 1$, and $\mu_+ = 10$.

We consider again the structured mesh with mesh size $h = 1/64$ and $\mathbf{Q}_2 - Q_1$ finite elements. Fig. 5 (right) shows the L^2 error and weighted H^1 error (198) for the velocity scaled by the H^3 norm of $\mathbf{u}$ and weighted L^2 error (199) for the pressure, also scaled by the H^3 norm of $\mathbf{u}$, against the

value of f. We observe that the scaled weighted H^1 error for the velocity and scaled weighted L^2 error for the pressure do not vary substantially as f varies, while the scaled L^2 error for the velocity increase as f decreases. When f goes to zero, the external phase loses its control over tangential motions in the internal fluid on Γ, thus allowing for purely rigid rotations in the perfectly circular Ω^-; see the definition of $\mathbf{u}^-$ in (201). While the seminorm $\|\mathbf{u}, p\|_*$ appearing on the right-hand side in (197) remains the same, the full Sobolev norm $\|\mathbf{u}^-\|_{k+2}$ grows as $O(f^{-1})$. Since we use isoparametric unfitted FE, we indeed see the uniform error bound with respect to $f \to 0$ if we normalize the error by the full Sobolev norm of the solution. See Remark 2.6. Summarizing, the approach proves to be robust in the energy norm as the physical parameter f varies.

Robustness with respect to the position of the interface. We conclude the series of the 2D tests with a set of simulations aimed at checking that our approach is not sensitive to the position of the interface with respect to the background mesh. For this purpose, we vary the center of the circle that represents Γ:

$$\mathbf{c} = (c_1, c_2),\ c_1 = \frac{h}{20} k \cos\left(\frac{k}{10}\pi\right),\ c_2 = \frac{h}{20} k \sin\left(\frac{k}{10}\pi\right), \quad k = 1, 2, ..., 20, \tag{202}$$

where h is the mesh size. We set $\mu_- = 1$, $\mu_+ = 10$ and $f = 10$.

Just like the two previous sets of simulations, we consider the mesh with mesh size $h = 1/64$ and the $\mathbf{Q}_2 - Q_1$ pair. Fig. 6 shows the L^2 error and weighted H^1 error (198) for the velocity and weighted L^2 error (199) for the pressure against the value of k in (202). We see that all the errors are fairly insensitive to the position of Γ with respect to the background mesh, indicating robustness.

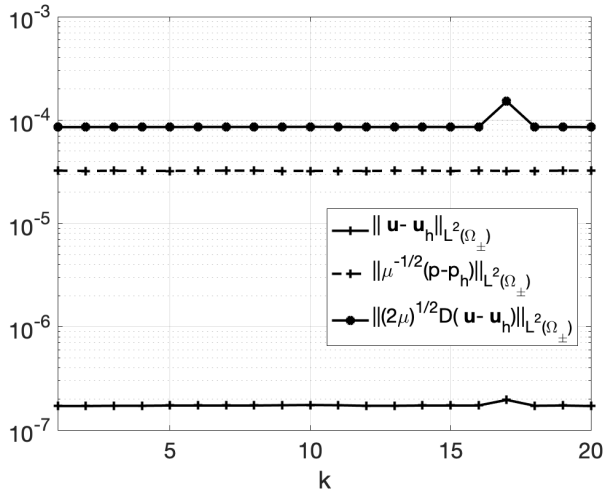

Figure 6: 2D test with $\mathbf{c} = \mathbf{0}$, $\mu_- = 1$, $\mu_+ = 10$, and $f = 10$: L^2 error and weighted H^1 error (198) for the velocity and weighted L^2 error (199) for the pressure against the value of k in (202).

2.5.2 3D tests

For the 3D tests, the domain Ω is cube $[-1.5, 1.5] \times [-1.5, 1.5] \times [-1.5, 1.5]$ and interface Γ is the unit sphere, centered at origin of the axes. We characterize Γ as the zero level set of function $\phi(\mathbf{x}) = ||\mathbf{x}||_2^2 - 1$, with $\mathbf{x} = (x, y, z)$. We consider the exact solution given by:

$$p^+ = \frac{1}{2}x, \qquad p^- = x, \tag{203}$$

$$\mathbf{u}^- = g^-(x,y)\begin{bmatrix} -y \\ x \\ 0 \end{bmatrix}, \qquad \mathbf{u}^+ = g^+(x,y)\begin{bmatrix} -y \\ x \\ 0 \end{bmatrix}, \tag{204}$$

where

$$g^+(x,y) = \frac{1}{2\mu_+}(x^2 + y^2 + z^2),$$
$$g^-(x,y) = \frac{1}{2\mu_-}(x^2 + y^2 + z^2) + \frac{\mu_- - 2\mu_+\mu_- - \mu_+}{2\mu_+\mu_-}.$$

The forcing terms $\mathbf{f}^-$ and $\mathbf{f}^+$ are found by plugging the above solution in in (140). We set $f = 1$, $\mu_- = 1$, and $\mu_+ = 100$. The surface tension coefficient is set to $\sigma = -0.5x$.

Just like for the 2D tests, we impose a Dirichlet condition (142) on the entire boundary, where function $\mathbf{g}$ is found from $\mathbf{u}^+$ in (204).

To verify our implementation of the finite element method in Sec. 2.2 in three dimensions and to further corroborate the results in Sec. 2.4, we consider structured meshes of tetrahedra with four levels of refinement. The initial triangulation has mesh size $h = 1$ and all the other meshes are obtained by halving h till $h = 0.125$. All the meshes feature a local one-level refinement near the corners of Ω. We choose to use finite element pair $\mathbf{P}_2 - P_1$. Fig. 7 shows a visualization of the solution computed with mesh $h = 0.125$. Fig. 8 shows the L^2 error and weighted H^1 error (198) for the velocity and weighted L^2 error (199) for the pressure against the mesh size h. For the small range of mesh sizes that we consider, we observe almost cubic convergence in the L^2 norm for the velocity, quadratic convergence in the weighted L^2 norm for the pressure and in the weighted H^1 norm for the velocity.

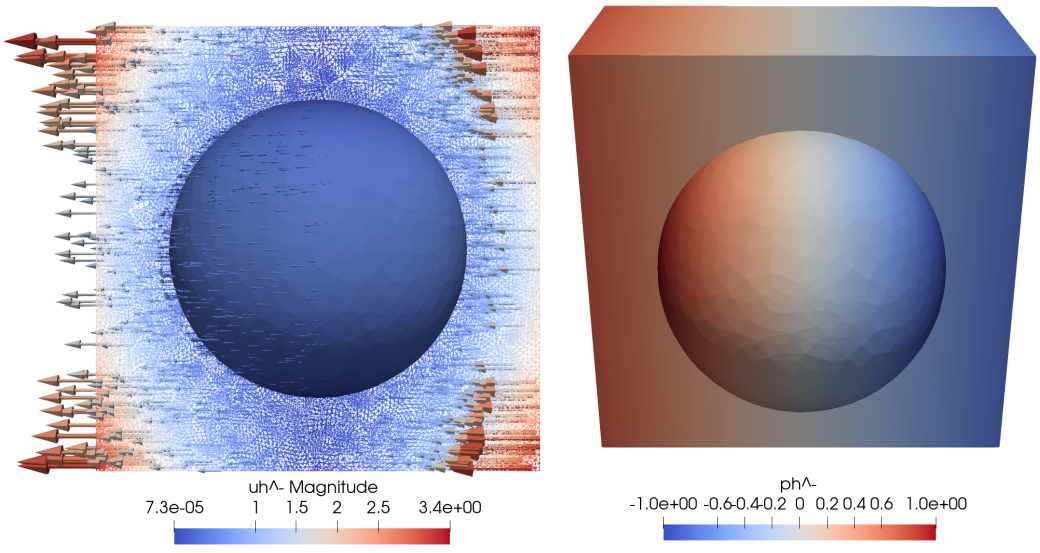

Figure 7: Approximation of exact solution (203)-(204) computed with the mesh with $h = 0.125$: velocity vectors colored with the velocity magnitude on the xz-section of Ω^+ and in Ω^- (left) and pressure in Ω^- and half Ω^+ (right).

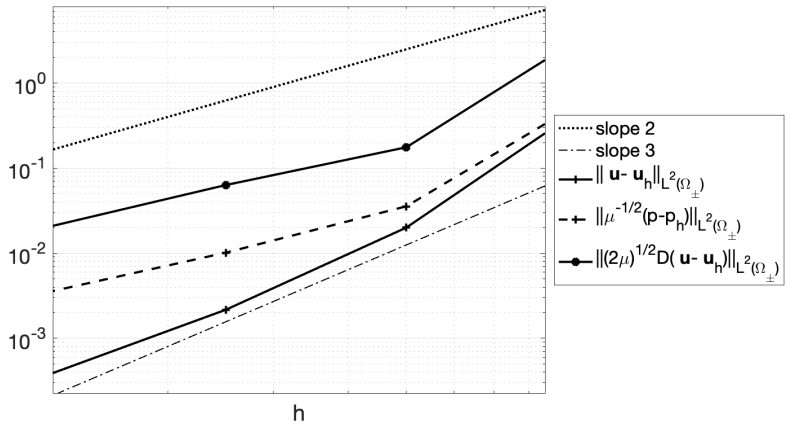

Figure 8: 3D test: L^2 error and weighted H^1 error (198) for the velocity and weighted L^2 error (199) for the pressure against the mesh size h.

2.6 Conclusions

In this section, we focused on the two-phase Stokes problem with slip between phases, which has received much less attention than its homogeneous counterpart (i.e. no slip between the phases). For the numerical approximation of this problem, we chose an isoparametric unfitted finite element approach of the CutFEM or Nitsche-XFEM family. For the unfitted generalized Taylor–Hood finite element pair $\mathbf{P}_{k+1} - P_k$, we prove stability and optimal error estimates, which follow from an inf-sup stability property. We show that the inf-sup stability constant is independent of the viscosity ratio, slip coefficient, position of the interface with respect to the background mesh and, of course, mesh size.

The 2D and 3D numerical experiments we used to test our approach feature an exact solution. They have been designed to support the theoretical findings and demonstrate the robustness of our approach for a wide range of physical parameter values. Finally, we show that our unfitted approach is insensitive to the position of the interface between the two phases with respect to the fixed computational mesh.

3 A Two-Phase Fluid with Material Viscous Interface

3.1 Problem description

Consider a fixed volume $\Omega \subset \mathbb{R}^3$ filled with two immiscible, viscous, and incompressible fluids separated by an interface $\Gamma(t)$ for all $t \in [0,T]$. We assume that $\Gamma(t)$ stays closed and sufficiently smooth (at least C^2) for all $t \in [0,T]$. Surface $\Gamma(t)$ separates Ω into two phases (subdomains) $\Omega_+(t)$ and $\Omega_-(t) := \Omega \setminus \overline{\Omega_+(t)}$. We assume $\Omega_-(t)$ to be completely internal, i.e. $\partial\Omega_-(t) \cap \partial\Omega = \emptyset$ for all times. See Fig. 1.

Denote by $\mathbf{n}^\pm$ the outward normals for $\Omega_\pm(t)$ and $\mathbf{n}$ the normal on Γ pointing from $\Omega_-(t)$ to $\Omega_+(t)$: it holds that $\mathbf{n}^- = \mathbf{n}$ and $\mathbf{n}^+ = -\mathbf{n}$ at Γ. For ease of notation, from now on we will drop the dependance on t for Γ, Ω_+, and Ω_-.

Recall model BII in Sec. 1.2.6,

$$
\begin{cases}
\rho^\pm \dot\partial_t \mathbf{u}^\pm - \mu^\pm \Delta \mathbf{u}^\pm + \nabla p^\pm = \mathbf{f}^\pm & \text{in } \Omega_\pm, \\
\operatorname{div} \mathbf{u}^\pm = 0 & \text{in } \Omega_\pm, \\
\rho_\Gamma \dot\partial_t \mathbf{U} - 2\mu_\Gamma \operatorname{div}_\Gamma \mathbf{D}_\Gamma(\mathbf{U}) + \nabla_\Gamma \pi - \pi\kappa\mathbf{n} = [\boldsymbol{\sigma}\mathbf{n}]_-^+ + \mathbf{b}^e & \text{on } \Gamma, \\
\operatorname{div}_\Gamma \mathbf{U} = 0 & \text{on } \Gamma, \\
\mathbf{u}^+ \cdot \mathbf{n} = \mathbf{u}^- \cdot \mathbf{n} = U_N & \text{on } \Gamma, \\
\mathbf{P}\boldsymbol{\sigma}^\pm \mathbf{n} = \pm f^\pm (\mathbf{P}\mathbf{u}^\pm - \mathbf{U}_T) & \text{on } \Gamma,
\end{cases}
\tag{205}
$$

The motion of the fluids occupying subdomains $\Omega_\pm$ is governed by the incompressible Navier–Stokes equations

$$
\rho^\pm \dot\partial_t \mathbf{u}^\pm = \operatorname{div} \boldsymbol{\sigma}^\pm + \mathbf{f}^\pm \qquad \text{in } \Omega_\pm, \tag{206}
$$

$$
\operatorname{div} \mathbf{u}^\pm = 0 \qquad \text{in } \Omega_\pm, \tag{207}
$$

for all $t \in (0,T)$. In (206), constants $\rho^{\pm}$ represent the fluid density, $\dot{\partial}_t$ denotes the material derivative, $\mathbf{f}^{\pm}$ are the external body forces, and $\boldsymbol{\sigma}^{\pm}$ are the Cauchy stress tensors.

We assume interface Γ to be a thin material layer with possibly different material properties from the bulk fluid. Motivated by applications in cell biology, we consider a viscous inextensible interface modeled as an "incompressible" surface fluid. The evolution of the material interface can be described in terms of the velocity of this surface fluid denoted by $\mathbf{U}$. Later, we will need the decomposition of $\mathbf{U}$ into tangential and normal components: $\mathbf{U} = \mathbf{U}_T + U_N\mathbf{n}$, with $\mathbf{U}_T \cdot \mathbf{n} = 0$, $U_N = \mathbf{n} \cdot \mathbf{U}$. The surface Navier-Stokes equations governing the motion of a fluidic deformable layer:

$$\rho_\Gamma \dot{\partial}_t \mathbf{U} = -\nabla_\Gamma \pi + 2\mu_\Gamma \operatorname{div}_\Gamma \mathbf{D}_\Gamma(\mathbf{U}) + \mathbf{f}_\Gamma + \mathbf{b}^e + \pi\kappa\mathbf{n} \qquad \text{on } \Gamma, \tag{208}$$

$$\operatorname{div}_\Gamma \mathbf{U} = 0 \qquad \text{on } \Gamma, \tag{209}$$

where ρ_Γ is the surface fluid density, μ_Γ is the surface fluid dynamic viscosity, κ denotes point-wise doubled mean curvature on Γ, and π is the surface fluid pressure. The material derivative in (208) is taken with respect to surface fluid trajectories, i.e. $\dot{\partial}_t \mathbf{U} = \frac{\partial \mathbf{U}}{\partial t} + (\mathbf{U} \cdot \nabla)\mathbf{U}$. Note that $\dot{\partial}_t \mathbf{U}$ is an intrinsic surface quantity, although both terms $\frac{\partial \mathbf{U}}{\partial t}$ and $(\mathbf{U} \cdot \nabla)\mathbf{U}$ depend on extension of $\mathbf{U}$ in the bulk. On the right hand side of (208), $\mathbf{f}_\Gamma$ denotes the external area force acting on the surface as a result of the interaction with the bulk fluids (specified below), while $\mathbf{b}^e$ denotes other possible area force (such as elastic bending forces) and not further specified.

Next, we turn to the coupling conditions between equations (206)–(207) posed in the bulk and equations (208)–(209) posed on Γ. First, the immiscibility condition means that the bulk fluid does not penetrate through Γ, which implies that

$$\mathbf{u}^+ \cdot \mathbf{n} = U_N = \mathbf{u}^- \cdot \mathbf{n} \qquad \text{on } \Gamma. \tag{210}$$

Normal velocity U_N determines radial deformations of $\Gamma(t)$ and so it governs the geometric evolution of the interface, which can be defined through the Lagrangian mapping $\Psi(t,\cdot)$ from $\Gamma(0)$ to $\Gamma(t)$:

for $\mathbf{x} \in \Gamma(0)$, $\Psi(t, \mathbf{x})$ solves the ODE system

$$\Psi(0, \mathbf{x}) = \mathbf{x}, \quad \frac{\partial \Psi(t, \mathbf{x})}{\partial t} = U_N(t, \Psi(t, \mathbf{x})), \quad t \in [0, T]. \tag{211}$$

In fluid vesicles and cells, typically a viscous and dense lipid membrane, represented by Γ, is surrounded by a less viscous and less dense liquid. We are interested in modelling slip with friction between the bulk fluid and the viscous membrane. Thus, we consider Navier-type conditions

$$\mathbf{P}\boldsymbol{\sigma}^+\mathbf{n} = f^+(\mathbf{P}\mathbf{u}^+ - \mathbf{U}_T) \qquad \text{on } \Gamma, \tag{212}$$

$$\mathbf{P}\boldsymbol{\sigma}^-\mathbf{n} = -f^-(\mathbf{P}\mathbf{u}^- - \mathbf{U}_T) \qquad \text{on } \Gamma, \tag{213}$$

where f^- and f^+ are friction coefficients at Γ on the Ω_- and Ω_+ side, respectively. Conditions (212)–(213) model an incomplete adhesion of a bulk fluid to the material surface with $1/f^\pm$ often referred to as a "slip length" [72]; see, e.g., [7, 57] for the modern description of experimental and theoretical validations. In particular, the acceptance of non-zero slip length resolves the well-known "no-collision paradox" [23, 49, 33], thus suggesting (212)–(213) to be an important modeling assumption in the simulation of a lipid vesicle – cell membrane contact (and fusion). We finally note that the Navier conditions are not an uncommon choice in numerical models, if the flow in boundary region is under-resolved [53].

The area force in (208) coming from the bulk fluid is defined by the jump of the normal stress on Γ:

$$\mathbf{f}_\Gamma = [\boldsymbol{\sigma}\mathbf{n}]_-^+ = \boldsymbol{\sigma}^+\mathbf{n} - \boldsymbol{\sigma}^-\mathbf{n} \ \text{ on } \Gamma. \tag{214}$$

On $\partial\Omega$ the system is endowed with boundary conditions either for the bulk velocity or for the bulk normal stress:

$$\mathbf{u}^+ = \mathbf{g} \quad \text{on } \partial\Omega_D, \tag{215}$$

$$\boldsymbol{\sigma}^+\mathbf{n}^+ = \mathbf{f}_N \quad \text{on } \partial\Omega_N. \tag{216}$$

Here $\overline{\partial\Omega_D} \cup \overline{\partial\Omega_N} = \overline{\partial\Omega}$ and $\partial\Omega_D \cap \partial\Omega_N = \emptyset$. See Fig. 1. At $t = 0$, initial velocity is given $\mathbf{u}^{\pm} = \mathbf{u}_0^{\pm}$ in $\Omega_{\pm}(0)$ and $\mathbf{U} = \mathbf{U}_0$ on $\Gamma(0)$.

3.1.1 Balance laws

We look for the energy balance of the coupled system (205)–(216). We make use of the following identities for time-dependent domains $\Omega_{\pm}(t)$, whose only moving part of the boundary is $\Gamma(t)$:

$$\frac{1}{2}\frac{d}{dt}\int_{\Omega_{\pm}(t)} |\mathbf{u}^{\pm}|^2 \, dV = \int_{\Omega_{\pm}(t)} \mathbf{u}^{\pm} \cdot \frac{\partial \mathbf{u}^{\pm}}{\partial t} \, dV + \frac{1}{2}\int_{\Gamma(t)} |\mathbf{u}^{\pm}|^2 \mathbf{u}^{\pm} \cdot \mathbf{n}^{\pm} \, dS, \tag{217}$$

$$\int_{\Omega_{\pm}(t)} (\mathbf{u}^{\pm} \cdot \nabla)\mathbf{u}^{\pm} \cdot \mathbf{u}^{\pm} \, dV = \frac{1}{2}\int_{\partial\Omega_{\pm}(t)} |\mathbf{u}^{\pm}|^2 \mathbf{u}^{\pm} \cdot \mathbf{n}^{\pm} \, dS. \tag{218}$$

Identity (217) is the Reynolds transport theorem, while identity (218) is obtained from integration by parts.

Let us start from the kinetic energy of the fluid in Ω_-:

$$\begin{aligned}
\frac{d}{dt}E^- &= \frac{1}{2}\frac{d}{dt}\int_{\Omega_-} \rho^- |\mathbf{u}^-|^2 \, dV = \int_{\Omega_-} \rho^- \mathbf{u}^- \cdot \frac{\partial \mathbf{u}^-}{\partial t} \, dV + \frac{1}{2}\int_{\Gamma} \rho^- |\mathbf{u}^-|^2 \mathbf{u}^- \cdot \mathbf{n} \, dS \\
&= \int_{\Omega_-} \mathbf{u}^- \cdot (\operatorname{div} \boldsymbol{\sigma}^- + \mathbf{f}^- - \rho^-(\mathbf{u}^- \cdot \nabla)\mathbf{u}^-) \, dV + \frac{1}{2}\int_{\Gamma} \rho^- |\mathbf{u}^-|^2 \mathbf{u}^- \cdot \mathbf{n} \, dS \\
&= \int_{\Omega_-} \nabla \cdot (\boldsymbol{\sigma}^- \mathbf{u}^-) \, dV - \int_{\Omega_-} \boldsymbol{\sigma}^- : \nabla \mathbf{u}^- \, dV + \int_{\Omega_-} \mathbf{u}^- \cdot \mathbf{f}^- \, dV \\
&= \int_{\Gamma} \mathbf{u}^- \cdot (\boldsymbol{\sigma}^- \mathbf{n}) \, dS - \int_{\Omega_-} \boldsymbol{\sigma}^- : \mathbf{D}(\mathbf{u}^-) dV + \int_{\Omega_-} \mathbf{u}^- \cdot \mathbf{f}^- \, dV \\
&= \int_{\Gamma} \mathbf{u}^- \cdot (\boldsymbol{\sigma}^- \mathbf{n}) \, dS - 2\mu^- \int_{\Omega_-} \|\mathbf{D}(\mathbf{u}^-)\|^2 \, dV + \int_{\Omega_-} \mathbf{u}^- \cdot \mathbf{f}^- \, dV
\end{aligned} \tag{219}$$

Above, we have used (217), (206), (207), (218), and integration by parts.

We repeat similar steps for the kinetic energy of the fluid in Ω_+, the main difference being that $\overline{\partial\Omega_+} = \overline{\Gamma} \cup \overline{\partial\Omega_D} \cup \overline{\partial\Omega_N}$ while $\overline{\partial\Omega_-} = \overline{\Gamma}$. We obtain:

$$\frac{d}{dt}E^+ = -\int_{\Gamma} \mathbf{u}^+ \cdot (\boldsymbol{\sigma}^+ \mathbf{n}) \, dS - 2\mu^+ \int_{\Omega_+} \left\|\mathbf{D}(\mathbf{u}^+)\right\|^2 dV + \int_{\Omega_+} \mathbf{u}^+ \cdot \mathbf{f}^+ \, dV + B \tag{220}$$

where

$$B = \int_{\partial\Omega_D} \left(\mathbf{g} \cdot (\boldsymbol{\sigma}^+ \mathbf{n}) - \frac{1}{2}\rho^+ |\mathbf{g}|^2 \mathbf{g} \cdot \mathbf{n}^+ \right) dS + \int_{\partial\Omega_N} \left(\mathbf{u}^+ \cdot \mathbf{f} - \frac{1}{2}\rho^+ |\mathbf{u}^+|^2 \mathbf{u}^+ \cdot \mathbf{n}^+ \right) dS. \tag{221}$$

Putting together (219) and (220), we obtain the total kinetic energy for the bulk flow:

$$\begin{aligned} \frac{dE}{dt} =& \frac{d}{dt}(E^+ + E^-) = -2\mu^- \int_{\Omega_-} \|\mathbf{D}(\mathbf{u}^-)\|^2 \, dV - 2\mu^+ \int_{\Omega_+} \left\|\mathbf{D}(\mathbf{u}^+)\right\|^2 dV - \int_\Gamma U_N [\mathbf{n}^T \sigma \mathbf{n}]_-^+ dS \\ & - \int_\Gamma f^- \mathbf{P}\mathbf{u}^- \cdot (\mathbf{P}\mathbf{u}^- - \mathbf{U}_T) dS - \int_\Gamma f^+ \mathbf{P}\mathbf{u}^+ \cdot (\mathbf{P}\mathbf{u}^+ - \mathbf{U}_T) dS \\ & + \int_{\Omega^-} \mathbf{u}^- \cdot \mathbf{f}^- \, dV + \int_{\Omega^+} \mathbf{u}^+ \cdot \mathbf{f}^+ \, dV + B \end{aligned} \tag{222}$$

where we have used (210), (212), and (213).

The energy balance on Γ is given by:

$$\begin{aligned} \frac{dE_\Gamma}{dt} &= \frac{1}{2}\frac{d}{dt} \int_\Gamma \rho_\Gamma |\mathbf{U}|^2 \, dS = \int_\Gamma \left(\rho_\Gamma \mathbf{U} \cdot \dot{\partial}_t \mathbf{U} + \frac{1}{2}\rho_\Gamma |\mathbf{U}|^2 \operatorname{div}_\Gamma \mathbf{U} \right) dS \\ &= \int_\Gamma \mathbf{U} \cdot \left(-\nabla_\Gamma \pi + 2\mu_\Gamma \operatorname{div}_\Gamma \mathbf{D}_\Gamma(\mathbf{U}) + \mathbf{f}_\Gamma + \mathbf{b}^e \right) dS \\ &= -2\mu_\Gamma \int_\Gamma \mathbf{D}_\Gamma(\mathbf{U}) : \nabla_\Gamma \mathbf{U} \, dS + \int_\Gamma \mathbf{U} \cdot [\boldsymbol{\sigma}\mathbf{n}]_-^+ \, dS + \int_\Gamma \mathbf{U}_T \cdot \mathbf{b}^e \, dS \\ &= -2\mu_\Gamma \int_\Gamma \|\mathbf{D}_\Gamma(\mathbf{U})\|^2 \, dS + \int_\Gamma U_N [\mathbf{n}^T \boldsymbol{\sigma} \mathbf{n}]_-^+ \, dS \\ &\quad + \int_\Gamma \mathbf{U}_T \cdot \left(f^+(\mathbf{P}\mathbf{u}^+ - \mathbf{U}_T) + f^-(\mathbf{P}\mathbf{u}^- - \mathbf{U}_T) \right) dS + \int_\Gamma \mathbf{U} \cdot \mathbf{b}^e \, dS, \end{aligned} \tag{223}$$

where we have applied (40) and used (51), (208)-(210), (212)-(214), and integration by parts.

Combining (222) and (223), we get the kinetic energy for the bulk and surface flows:

$$\begin{aligned}\frac{dE}{dt}+\frac{dE_\Gamma}{dt} = &\underbrace{-2\mu^-\int_{\Omega_-}\|\mathbf{D}(\mathbf{u}^-)\|^2\,dV-2\mu^+\int_{\Omega_+}\left\|\mathbf{D}(\mathbf{u}^+)\right\|^2\,dV}_{\text{Bulk fluid viscous dissipation}}\ \underbrace{-2\mu_\Gamma\int_\Gamma\|\mathbf{D}_\Gamma(\mathbf{U}_T)\|^2\,dS}_{\text{Surface fluid viscous dissipation}}\\ &\underbrace{-\int_\Gamma f^-\|\mathbf{P}\mathbf{u}^--\mathbf{U}_T\|^2dS-\int_\Gamma f^+\|\mathbf{P}\mathbf{u}^+-\mathbf{U}_T\|^2d}_{\text{Frictional energy dissipation}}\\ &\underbrace{+\int_\Gamma\mathbf{u}^-\cdot\mathbf{f}^-\,dV+\int_\Gamma\mathbf{u}^+\cdot\mathbf{f}^+\,dV+\int_\Gamma\mathbf{U}\cdot\mathbf{b}^e dS}_{\text{work of external forces}}\ \underbrace{+B}_{\text{work of b.c.}}\end{aligned}\tag{224}$$

where B, i.e. the work of the boundary conditions, is defined in (221).

From (224), we see that in the absence of external forces and with no energy inflow through the boundary the system is dissipative, i.e. thermodynamically consistent.

3.1.2 A simplified steady problem

In this section, we consider a (strongly) simplified version of the problem presented in previous section. Our main assumption is that the coupled bulk and surface fluid system has reached a steady state and inertia terms can be neglected. Since the steady state implies $\Gamma(t) = \Gamma(0)$, we have $U_N = 0$ and hence $\mathbf{U} = \mathbf{U}_T$. This simplified surface–bulk Stokes problem models a viscosity dominated two-phase flow with the viscous interface in a dynamical equilibrium; see also Remark 3.1. It is an interesting model problem for the purpose of numerical analysis. With these simplifications, the equations (206)–(207) become:

$$-\mu^\pm\Delta\mathbf{u}^\pm+\nabla p=\mathbf{f}^\pm \qquad \text{in } \Omega_\pm,\tag{225}$$

$$\operatorname{div}\mathbf{u}^\pm=0 \qquad \text{in } \Omega_\pm.\tag{226}$$

We impose a non-homogeneous Dirichlet condition on the entire outer boundary of Ω, i.e. problem (225)–(226) is supplemented with boundary condition (215) with $\mathbf{g}\in[H^{1/2}(\partial\Omega_D)]^3$ and $\partial\Omega_D=\partial\Omega$. Under our assumption, the momentum equation for the surface fluid simplifies to

$-2\mu_\Gamma \operatorname{div}_\Gamma \mathbf{D}_\Gamma(\mathbf{U}_T) + \nabla_\Gamma \pi - \pi\kappa\mathbf{n} = [\boldsymbol{\sigma}\mathbf{n}]_-^+ + \mathbf{b}^e$. The tangential part of the above momentum equation together with the inextensibility condition (209) leads to the surface Stokes problem

$$-2\mu_\Gamma \mathbf{P} \operatorname{div}_\Gamma \mathbf{D}_\Gamma(\mathbf{U}_T) + \nabla_\Gamma \pi = [\mathbf{P}\boldsymbol{\sigma}\mathbf{n}]_-^+ + \mathbf{P}\mathbf{b}^e \qquad \text{on } \Gamma, \tag{227}$$

$$\operatorname{div}_\Gamma \mathbf{U}_T = 0 \qquad \text{on } \Gamma, \tag{228}$$

while the normal part simplifies to

$$[\mathbf{n}^T \boldsymbol{\sigma}\mathbf{n}]_+^- = \pi\kappa \qquad \text{on } \Gamma. \tag{229}$$

The interface condition above is standard in many models of two-phase flows, where π has the meaning of the surface tension coefficient.

Coupling condition (210) is replaced by:

$$\mathbf{u}^+ \cdot \mathbf{n} = \mathbf{u}^- \cdot \mathbf{n} \qquad \text{on } \Gamma, \tag{230}$$

while conditions (212) and (213) still hold:

$$\mathbf{P}\boldsymbol{\sigma}^\pm \mathbf{n} = \pm f^\pm (\mathbf{P}\mathbf{u}^\pm - \mathbf{U}_T) \qquad \text{on } \Gamma. \tag{231}$$

Finally, we will see that the (weak formulation of the) problem is well-posed under two mean conditions for the bulk pressure:

$$\int_{\Omega^\pm} p^\pm \, dx = 0.$$

Remark 3.1 Since $\mathbf{U} \cdot \mathbf{n} = 0$, condition (230) allows the flow through the steady interface Γ. This is inconsistent with (210), which assumes immiscibility of fluids. For a physically consistent formulation that describes the true equilibrium one has to set $\mathbf{u}^+ \cdot \mathbf{n} = \mathbf{u}^- \cdot \mathbf{n} = 0$ on Γ, but allow the shape of Γ to be the unknown, i.e. to be determined as a part of the problem. For such equilibrium to exist, external forces and boundary conditions may have to satisfy additional

constraints. Finding such constraints and solving the resulting non-linear problem is outside the scope of this paper. We rather follow a common convention in the analysis of models for steady two-phase problems and allow (230) for the steady interface; see, e.g. [31, 78, 37, 10].

3.1.3 Variational formulation

The purpose of this section is to derive the variational formulation of coupled problem (225)–(231). Let us introduce some standard notation. The space of functions whose square is integrable in a domain ω is denoted by $L^2(\omega)$. The space of functions whose distributional derivatives of order up to $m \geq 0$ (integer) belong to $L^2(\omega)$ is denoted by $H^m(\omega)$. The space of vector-valued functions with components in $L^2(\omega)$ is denoted with $L^2(\omega)^3$. $H^1(\mathrm{div}\,,\omega)$ is the space of functions in $L^2(\omega)$ with divergence in $L^2(\omega)$. Moreover, we introduce the following functional spaces:

$$
\begin{aligned}
&V^- = H^1(\Omega_-)^3,\ V^+ = \{\mathbf{u} \in H^1(\Omega_+)^3, \mathbf{u}\big|_{\partial\Omega_D} = \mathbf{g}\},\ V_0^+ = \{\mathbf{u} \in H^1(\Omega_+)^3, \mathbf{u}\big|_{\partial\Omega_D} = \mathbf{0}\},\\
&V^{\pm} = \{\mathbf{u} = (\mathbf{u}^-, \mathbf{u}^+) \in V^- \times V^+, \mathbf{u}^- \cdot \mathbf{n} = \mathbf{u}^+ \cdot \mathbf{n} \text{ on } \Gamma\},\\
&V_0^{\pm} = \{\mathbf{u} = (\mathbf{u}^-, \mathbf{u}^+) \in V^- \times V_0^+, \mathbf{u}^- \cdot \mathbf{n} = \mathbf{u}^+ \cdot \mathbf{n} \text{ on } \Gamma\},\\
&L^2_{\pm} = \{p = (p^-, p^+) \in L^2(\Omega_-) \times L^2(\Omega_+),\ s.t.\ \int_{\Omega^{\pm}} p^{\pm}\, dx = 0\},\\
&V_\Gamma = \{\mathbf{U} \in H^1(\Gamma)^3 : \mathbf{U} \cdot \mathbf{n} = 0\}.
\end{aligned}
$$

The space $V^{\pm}$ can be also characterized as $(V^- \times V^+) \cap H^1(\mathrm{div}\,,\Omega)$. We use $(\cdot,\cdot)_\omega$ and $\langle\cdot,\cdot\rangle_\omega$ to denote the L^2 product and the duality pairing, respectively.

Multiplying (225) by $\mathbf{v} \in V_0^{\pm}$ and (226) by $q \in L^2_0(\Omega)$ and integrating over each subdomain, we

see that smooth bulk velocity and pressure satisfy integral identity:

$$
\begin{aligned}
&-(p^-, \operatorname{div}\mathbf{v}^-)_{\Omega_-} - (p^+, \operatorname{div}\mathbf{v}^+)_{\Omega_+} + 2(\mu^-\mathbf{D}(\mathbf{u}^-), \mathbf{D}(\mathbf{v}^-))_{\Omega_-} + 2(\mu^+\mathbf{D}(\mathbf{u}^+), \mathbf{D}(\mathbf{v}^+))_{\Omega_+} \\
&\quad - \langle \pi\kappa, \mathbf{v}^- \cdot \mathbf{n}\rangle_\Gamma + \langle f^-(\mathbf{P}\mathbf{u}^- - \mathbf{U}), \mathbf{P}\mathbf{v}^-\rangle_\Gamma + \langle f^+(\mathbf{P}\mathbf{u}^+ - \mathbf{U}), \mathbf{P}\mathbf{v}^+\rangle_\Gamma \\
&\quad = (\mathbf{f}^-, \mathbf{v}^-)_{\Omega_-} + (\mathbf{f}^+, \mathbf{v}^+)_{\Omega_+} \qquad (232)\\
&(\operatorname{div}\mathbf{u}^-, q^-)_{\Omega_-} + (\operatorname{div}\mathbf{u}^+, q^+)_{\Omega_+} = 0 \qquad (233)
\end{aligned}
$$

for all $(\mathbf{v}, q) \in V_0^\pm \times L_0^2(\Omega)$. The interface terms in (232) have been obtained using coupling conditions (231) and (229) as follows:

$$
\begin{aligned}
-\langle \boldsymbol{\sigma}^-\mathbf{n}, \mathbf{v}^-\rangle_\Gamma + \langle \boldsymbol{\sigma}^+\mathbf{n}, \mathbf{v}^+\rangle_\Gamma &= -\langle \mathbf{P}\boldsymbol{\sigma}^-\mathbf{n}, \mathbf{P}\mathbf{v}^-\rangle_\Gamma + \langle \mathbf{P}\boldsymbol{\sigma}^+\mathbf{n}, \mathbf{P}\mathbf{v}^+\rangle_\Gamma - \langle [\mathbf{n}^T\boldsymbol{\sigma}\mathbf{n}]_+^-, \mathbf{v}^- \cdot \mathbf{n}\rangle_\Gamma \\
&= \langle f^-(\mathbf{P}\mathbf{u}^- - \mathbf{U}), \mathbf{P}\mathbf{v}^-\rangle_\Gamma + \langle f^+(\mathbf{P}\mathbf{u}^+ - \mathbf{U}), \mathbf{P}\mathbf{v}^+\rangle_\Gamma \\
&\quad - \langle \pi\kappa, \mathbf{v}^- \cdot \mathbf{n}\rangle_\Gamma.
\end{aligned}
$$

Likewise, we find that the surface velocity and pressure satisfy the following integral identities:

$$
\begin{aligned}
&-(\pi, \operatorname{div}_\Gamma\mathbf{V})_\Gamma + 2(\mu_\Gamma\mathbf{D}_\Gamma(\mathbf{U}), \mathbf{D}_\Gamma(\mathbf{V}))_\Gamma - \langle f^-(\mathbf{P}\mathbf{u}^- - \mathbf{U}), \mathbf{V}\rangle_\Gamma \\
&\quad - \langle f^+(\mathbf{P}\mathbf{u}^+ - \mathbf{U}), \mathbf{V}\rangle_\Gamma = (\mathbf{P}\mathbf{b}^e, \mathbf{V})_\Gamma \qquad (234)\\
&(\operatorname{div}_\Gamma\mathbf{U}, \tau)_\Gamma = 0 \qquad (235)
\end{aligned}
$$

for all $(\mathbf{V}, \tau) \in V_\Gamma \times L_0^2(\Gamma)$.

The weak formulation of the coupled problem (225)–(231) follows by combining (232)–(233) and (234)–(235). In order to write it, we introduce the following forms for all $\mathbf{u} \in V^\pm$, $\mathbf{v} \in \mathbf{V}_0^\pm$,

$\mathbf{U}, \mathbf{V} \in V_\Gamma$, $p \in L^2(\Omega)$, $\pi \in L^2(\Gamma)$:

$$\begin{aligned}
a(\{\mathbf{u}, \mathbf{U}\}, \{\mathbf{v}, \mathbf{V}\}) =& 2(\mu^- \mathbf{D}(\mathbf{u}^-), \mathbf{D}(\mathbf{v}^-))_{\Omega_-} + 2(\mu^+ \mathbf{D}(\mathbf{u}^+), \mathbf{D}(\mathbf{v}^+))_{\Omega_+} \\
&+ 2(\mu_\Gamma \mathbf{D}_\Gamma(\mathbf{U}), \mathbf{D}_\Gamma(\mathbf{V}))_\Gamma + \langle f^-(\mathbf{P}\mathbf{u}^- - \mathbf{U}), \mathbf{P}\mathbf{v}^- - \mathbf{V} \rangle_\Gamma \\
&+ \langle f^+(\mathbf{P}\mathbf{u}^+ - \mathbf{U}), \mathbf{P}\mathbf{v}^+ - \mathbf{V} \rangle_\Gamma, \\
b(\{\mathbf{v}, \mathbf{V}\}, \{p, \pi\}) =& -(p^-, \operatorname{div} \mathbf{v}^-)_{\Omega_-} - (p^+, \operatorname{div} \mathbf{v}^+)_{\Omega_+} - (\pi, \operatorname{div}_\Gamma \mathbf{V})_\Gamma, \\
s(\mathbf{v}, \pi) =& -\langle \pi\kappa, \mathbf{v} \cdot \mathbf{n} \rangle_\Gamma, \\
r(\mathbf{v}, \mathbf{V}) =& (\mathbf{f}^-, \mathbf{v}^-)_{\Omega_-} + (\mathbf{f}^+, \mathbf{v}^+)_{\Omega_+} + (\mathbf{P}\mathbf{b}^e, \mathbf{V})_\Gamma.
\end{aligned}$$

Then, the weak formulation reads: *Find* $(\mathbf{u}, p) \in V^\pm \times L^2_\pm$, *and* $(\mathbf{U}, \pi) \in V_\Gamma \times L^2(\Gamma)$ *such that*

$$\begin{cases} a(\{\mathbf{u}, \mathbf{U}\}, \{\mathbf{v}, \mathbf{V}\}) + b(\{\mathbf{v}, \mathbf{V}\}, \{p, \pi\}) + s(\mathbf{v}, \pi) = r(\mathbf{v}, \mathbf{V}) \\ b(\{\mathbf{u}, \mathbf{U}\}, \{q, \tau\}) = 0 \end{cases} \tag{236}$$

for all $(\mathbf{v}, q) \in V_0^\pm \times L^2_0(\Omega)$ *and* $(\mathbf{V}, \tau) \in V_\Gamma \times L^2_0(\Gamma)$. Note that test and trial pressure spaces both involve two (different) gauge conditions.

3.1.4 Well-posedness

With the goal of proving the well-posedness of the stationary problem, we start by showing that $a(\{\cdot,\cdot\}, \{\cdot,\cdot\})$ is coercive. Let $\|\mathbf{u}\|^2_{H^1(\Omega_\pm)} = \|\mathbf{u}^+\|^2_{H^1(\Omega_+)} + \|\mathbf{u}^-\|^2_{H^1(\Omega_-)}$. Let $\|p\|^2_{L^2(\Omega_\pm)} = \|p\|^2_{\Omega_+} + \|p\|^2_{\Omega_-}$. We define the following additional norms:

$$|||\{\mathbf{v}, \mathbf{V}\}|||^2 = \|\mathbf{v}\|^2_{H^1(\Omega_\pm)} + \|\mathbf{V}\|^2_{H^1(\Gamma)}, \quad |||\{p, \pi\}|||^2 = \|p\|^2_{\Omega_\pm} + \|\pi\|^2_\Gamma$$

The coercivity result is formulated in the form of a lemma.

Lemma 3.2 *For any* $\mathbf{v} \in V_0^\pm$ *and* $\mathbf{V} \in V_\Gamma$ *it holds*

$$a(\{\mathbf{v}, \mathbf{V}\}, \{\mathbf{v}, \mathbf{V}\}) \geq C|||\{\mathbf{v}, \mathbf{V}\}|||^2 \tag{237}$$

with a positive constant C, which may depend on the viscosity values and $\Omega_\pm$.

Proof: One readily computes that

$$a(\{\mathbf{v},\mathbf{V}\},\{\mathbf{v},\mathbf{V}\}) = 2(\mu^-\mathbf{D}(\mathbf{v}^-),\mathbf{D}(\mathbf{v}^-))_{\Omega_-} + 2(\mu^+\mathbf{D}(\mathbf{v}^+),\mathbf{D}(\mathbf{v}^+))_{\Omega_+} + 2(\mu_\Gamma\mathbf{D}_\Gamma(\mathbf{V}),\mathbf{D}_\Gamma(\mathbf{V}))_\Gamma + f^-\|\mathbf{P}\mathbf{v}^- - \mathbf{V}\|_\Gamma^2 + f^+\|\mathbf{P}\mathbf{v}^+ - \mathbf{V}\|_\Gamma^2. \quad (238)$$

Since function $\mathbf{v}^+$ satisfies homogeneous Dirichlet boundary condition on $\partial\Omega_+ \setminus \Gamma$, we apply the following Korn's inequality in Ω_+:

$$\left\|\mathbf{v}^+\right\|_{H^1(\Omega_+)} \le C\|\mathbf{D}(\mathbf{v}^+)\|_{\Omega_+} \quad (239)$$

By the triangle and trace inequalities in Γ, we get

$$\|\mathbf{V}\|_\Gamma \le \|\mathbf{P}\mathbf{v}^+ - \mathbf{V}\|_\Gamma + \|\mathbf{P}\mathbf{v}^+\|_\Gamma \le \|\mathbf{P}\mathbf{v}^+ - \mathbf{V}\|_\Gamma + C\left\|\mathbf{v}^+\right\|_{H^1(\Omega_+)}. \quad (240)$$

We further apply Korn's inequality on Γ [51]:

$$\|\mathbf{V}\|_{H^1(\Gamma)} \le C\left(\|\mathbf{V}\|_\Gamma + \|\mathbf{D}_\Gamma(\mathbf{V})\|_\Gamma\right). \quad (241)$$

Next, we can estimate the trace of $\mathbf{v}^-$ on Γ through the triangle inequality:

$$\left\|\mathbf{v}^-\right\|_\Gamma \le \|\mathbf{P}\mathbf{v}^- - \mathbf{V}\|_\Gamma + \|\mathbf{V}\|_\Gamma \le \|\mathbf{P}\mathbf{v}^- - \mathbf{V}\|_\Gamma + \|\mathbf{V}\|_{H^1(\Gamma)}. \quad (242)$$

We finally apply the following Korn's inequality in Ω_-:

$$\|\mathbf{v}\|_{H^1(\Omega_-)} \le C\left(\|\mathbf{D}(\mathbf{v}^-)\|_{\Omega_-} + \left\|\mathbf{v}^-\right\|_\Gamma\right). \quad (243)$$

Identity (238) and inequalities (239)–(243) lead to (237) after easy computations.

□

The continuity of the bilinear forms $a(\{\cdot,\cdot\},\{\cdot,\cdot\})$, $b(\{\cdot,\cdot\},\{\cdot,\cdot\})$ and $s(\cdot,\cdot)$ follows from standard arguments based on the Cauchy–Schwarz and triangle inequalities:

$$\begin{aligned} a(\{\mathbf{u},\mathbf{U}\},\{\mathbf{v},\mathbf{V}\}) &\le C|||\{\mathbf{u},\mathbf{U}\}|||\,|||\{\mathbf{v},\mathbf{V}\}||| \quad \text{for all } \mathbf{u},\mathbf{v}\in V_0^{\pm},\ \mathbf{U},\mathbf{V}\in V_\Gamma,\\ b(\{\mathbf{u},\mathbf{U}\},\{p,\pi\}) &\le C|||\{\mathbf{u},\mathbf{U}\}|||\,|||\{p,\pi\}||| \quad \text{for all } \mathbf{u}\in V_0^{\pm},\ \mathbf{U}\in V_\Gamma,\ p\in L^2(\Omega),\ \pi\in L^2(\Gamma),\\ s(\mathbf{v},\pi) &\le C|||\{\mathbf{v},0\}|||\,|||\{0,\pi\}||| \quad \text{for all } \mathbf{v}\in V^{\pm},\ \pi\in L^2(\Gamma). \end{aligned} \tag{244}$$

Problem (236) falls into the class of so-called generalized saddle point problems. An abstract well-posedness result for such problems can be found, e.g. in [6, 73], which extend the Babuşka–Brezzi theory. Applied to (236), this well-posedness result requires coercivity (237), continuity (244) and two inf-sup conditions formulated in the following lemma.

Lemma 3.3 *The following inf-sup conditions hold with positive constants γ_1 and γ_2:*

$$\sup_{\mathbf{v}\in V_0^{\pm},\mathbf{V}\in V_\Gamma} \frac{b(\{\mathbf{v},\mathbf{V}\},\{p,\pi\})+s(\mathbf{v},\pi)}{|||\{\mathbf{v},\mathbf{V}\}|||} \ge \gamma_1|||\{p,\pi\}|||, \quad \forall\ p\in L^2_{\pm},\ \pi\in L^2(\Gamma), \tag{245}$$

$$\sup_{\mathbf{v}\in V_0^{\pm},\mathbf{V}\in V_\Gamma} \frac{b(\{\mathbf{v},\mathbf{V}\},\{p,\pi\})}{|||\{\mathbf{v},\mathbf{V}\}|||} \ge \gamma_2|||\{p,\pi\}|||, \quad \forall\ p\in L^2_0(\Omega),\ \pi\in L^2_0(\Gamma). \tag{246}$$

Proof: The proof follows by combining well-known results about the existence of a continuous right inverse of the divergence operator in $H^1_0(\Omega)^3$ [8] and V_Γ [51]: For arbitrary $p\in L^2_0(\Omega)$ and $\pi\in L^2_0(\Gamma)$ there exist $\mathbf{v}\in H^1_0(\Omega)^3$ and $\mathbf{V}\in V_\Gamma$ such that

$$\begin{aligned} p &= \operatorname{div}\mathbf{v} \ \text{ in } \Omega, \quad \text{and} \quad \|\mathbf{v}\|_{H^1(\Omega)} \le c_\Omega\|p\|_{L^2(\Omega)},\\ \pi &= \operatorname{div}_\Gamma\mathbf{V} \ \text{ on } \Gamma, \quad \text{and} \quad \|\mathbf{V}\|_{H^1(\Gamma)} \le c_\Gamma\|\pi\|_\Gamma. \end{aligned} \tag{247}$$

Letting $\mathbf{v}^{\pm} = \mathbf{v}|_{\Omega_{\pm}}$, $(\mathbf{v}^-, \mathbf{v}^+)^T \in V_0^{\pm}$, and adding estimates in (247) we get

$$|||\{p,\pi\}|||^2 \le b(\{\mathbf{v},\mathbf{V}\},\{p,\pi\}), \tag{248}$$

$$|||\{\mathbf{v},\mathbf{V}\}||| \le c_\Omega \|p\|_\Omega + c_\Gamma \|\pi\|_\Gamma \le (c_\Omega + c_\Gamma)|||\{p,\pi\}|||. \tag{249}$$

This proves (246) with $\gamma_2 = 1/(c_\Omega + c_\Gamma)$.

To show (245), we split $\pi = \pi_0 + \pi^\perp$ with $\pi_0 \in L_0^2(\Gamma)$ and $\pi^\perp = |\Gamma|^{-1}\int_\Gamma \pi\, ds$. For the π_0 part of π, we use again (247) as above, while for $p^{\pm} \in L_0^2(\Omega^{\pm})$ we use the existence of a continuous right inverse of div in $H_0^1(\Omega^{\pm})^3$ to claim the existence of $\mathbf{v} \in H_0^1(\Omega^-)^3 \times H_0^1(\Omega^+)^3 \subset V_0^{\pm}$ and $\mathbf{V} \in V_\Gamma$ such that

$$|||\{p,\pi_0\}||| \le b(\{\mathbf{v},\mathbf{V}\},\{p,\pi_0\}) + s(\mathbf{v},\pi), \qquad |||\{\mathbf{v},\mathbf{V}\}||| \le (c_\Omega + c_\Gamma)|||\{p,\pi_0\}|||, \tag{250}$$

with some positive c_Ω, c_Γ depending only on Γ and Ω. We also used that $\mathbf{v} = \mathbf{0}$ on Γ implies $s(\mathbf{v},\pi) = 0$.

Let $C^{\pm} = \pm|\Omega^{\pm}|^{-1}|\Gamma| \int_\Gamma \kappa\, ds$. To control $\|\pi^\perp\|_\Gamma$, we need $\mathbf{v}_1 \in V_0^{\pm}$ such that

$$\operatorname{div}\mathbf{v}_1 = -C^{\pm} \ \text{ in } \Omega^{\pm}, \ \ \mathbf{v}_1\cdot\mathbf{n} = \kappa \ \text{ on } \Gamma \ \text{ and } \ \|\mathbf{v}_1\|_{H^1(\Omega^{\pm})} \le C. \tag{251}$$

Such $\mathbf{v}_1$ can be built, for example, as follows: Let $\mathbf{v}_1^- = \nabla\psi$, where $\psi \in H^2(\Omega^-)$ solves the Neumann problem $-\Delta\psi = C^-$ in Ω^-, $\mathbf{n}\cdot\nabla\psi = \kappa$ on Γ. Since $\Gamma = \partial\Omega^-$ is smooth, by the H^2-regularity of the Neumann problem we have that $\|\mathbf{v}_1^-\|_{H^1(\Omega^-)} \le \|\psi\|_{H^2(\Omega^-)} \le C$. The boundary $\partial\Omega$ is only Lipschits and so the Neumann problem in Ω^+ is not necessarily H^2-regular. To handle this, we first extend $\mathbf{v}_1^-$ from Ω^- to a function $\tilde{\mathbf{v}}_1$ in $H_0^1(\Omega)^3$ such that $\|\tilde{\mathbf{v}}_1\|_{H^1(\Omega^+)} \le c\|\mathbf{v}_1^-\|_{H^1(\Omega^-)}$ [96]. Next, we consider $\mathbf{w} \in H_0^1(\Omega^+)^3$ such that $\operatorname{div}\mathbf{w} = C^+ - \operatorname{div}\tilde{\mathbf{v}}_1 \in L_0^2(\Omega^+)$, and $\|\mathbf{w}\|_{H^1(\Omega^+)} \le c_{\Omega^+}\|\operatorname{div}\mathbf{w}\|_{L^2(\Omega^+)} \le C$ [8]. The desired $\mathbf{v}_1^+$ is given in Ω^+ by $\mathbf{v}_1^+ = \tilde{\mathbf{v}}_1 + \mathbf{w}$. Since $\operatorname{div}\mathbf{v}_1 = -C^{\pm}$,

for $p \in L^2_{\pm}(\Omega)$ and $\pi \in L^2(\Gamma)$ we have identities

$$b(\{\mathbf{v}_1, 0\}, \{p, \pi\}) = 0 = (\operatorname{div}_\Gamma \mathbf{V}, \pi^\perp)_\Gamma. \tag{252}$$

We also note the equality $\|\pi^\perp\|^2_\Gamma = \hat{c}\, s(\mathbf{v}_1, \pi^\perp)$, with

$$\hat{c} = \pi^\perp |\Gamma| / \int_\Gamma \kappa^2 ds.$$

The denominator above is positive, since Γ is closed and so κ cannot be zero everywhere on Γ. We use (248)–(252) to estimate for some $\beta > 0$:

$$\begin{aligned}
|||\{p, \pi\}|||^2 &= |||\{p, \pi_0\}|||^2 + \beta \|\pi^\perp\|^2_\Gamma \\
&\le b(\{\mathbf{v}, \mathbf{V}\}, \{p, \pi_0\}) + s(\mathbf{v}, \pi) + s(\beta \hat{c}\, \mathbf{v}_1, \pi^\perp) \\
&= b(\{\mathbf{v} + \beta \hat{c} \mathbf{v}_1, \mathbf{V}\}, \{p, \pi\}) + s(\mathbf{v} + \beta \hat{c} \mathbf{v}_1, \pi) - (\beta \hat{c} \mathbf{v}_1, \pi_0)_\Gamma \\
&\le b(\{\mathbf{v} + \beta \hat{c} \mathbf{v}_1, \mathbf{V}\}, \{p, \pi\}) + s(\mathbf{v} + \beta \hat{c} \mathbf{v}_1, \pi) + \frac{\beta^2 \hat{c}^2}{2} \|\mathbf{v}_1\|^2_\Gamma + \frac{1}{2} \|\pi_0\|^2_\Gamma \\
&\le b(\{\mathbf{v} + \beta \hat{c} \mathbf{v}_1, \mathbf{V}\}, \{p, \pi\}) + s(\mathbf{v} + \beta \hat{c} \mathbf{v}_1, \pi) + c_3\, \beta^2 \|\pi^\perp\|^2_\Gamma + \frac{1}{2} \|\pi_0\|^2_\Gamma.
\end{aligned}$$

with some $c_3 > 0$ depending only on Γ and Ω. For $\beta > 0$ sufficiently small such that $\frac{\beta}{2} - c_3\, \beta^2 \ge 0$, we get

$$c |||\{p, \pi\}|||^2 \le b(\{\mathbf{v} + \beta \hat{c} \mathbf{v}_1, \mathbf{V}\}, \{p, \pi\}) + s(\mathbf{v} + \beta \hat{c} \mathbf{v}_1, \pi), \tag{253}$$

with $c > 0$ depending only on Γ and Ω. Thanks to the triangle inequality, the second estimate in (250) and the definition of $\hat{c}$ and $\mathbf{v}_1$, we find the bound

$$|||\mathbf{v} + \beta \hat{c} \mathbf{v}_1, \mathbf{V}||| \le |||\mathbf{v}, \mathbf{V}||| + \beta \hat{c} |||\beta \hat{c} \mathbf{v}_1, 0||| \le (c_\Omega + c_\Gamma) |||\{p, \pi_0\}||| + C \|\pi^\perp\|_\Gamma \le C\, |||\{p, \pi\}|||,$$

with $C > 0$ depending only on Γ and Ω. The combination of the above bound and (253) completes the proof of the lemma. □

3.2 Numerical method for solving coupled bulk-surface flow problem

We adopt the notations and discretization scheme for the bulk problem in Sec. 2.2. For the discretization of the surface Stokes problem, we first consider the generalized Taylor–Hood bulk spaces in the strip Ω_h^Γ:

$$V_{\Gamma,h} = \{\mathbf{U} \in C(\Omega_h^\Gamma)^3 : \mathbf{U}|_T \in \mathbf{P}_{k+1}(T)\ \forall T \in \mathcal{T}_h^\Gamma\},$$
$$Q_{\Gamma,h} = \{\pi \in C(\Omega_h^\Gamma) : \pi|_T \in P_k(T)\ \forall T \in \mathcal{T}_h^\Gamma\},$$

$Q^0_{\Gamma,h} = Q_{\Gamma,h} \cap L^2_0(\Gamma)$. In the trace finite element method, we use the traces of functions from $V_{\Gamma,h}$ and $Q_{\Gamma,h}$ on Γ. The inf-sup stability of the resulting trace FEM was analyzed in [77] for $k = 1$ and extended to higher order isoparametric trace elements in [52].

In the treatment of the surface Stokes problem, one has to enforce the tangentiality condition $\mathbf{U} \cdot \mathbf{n} = 0$ on Γ. In order to enforce it while avoiding locking, we follow [42, 43, 51, 89, 74] and add a penalty term to the weak formulation.

A discrete variational analogue of problem (236) reads: Find $(\mathbf{u}_h, p_h) \in V_h^\pm \times L^2_\pm(\Omega)_h$, and $(\mathbf{U}_h, \pi_h) \in V_{\Gamma,h} \times Q_{\Gamma,h}$ such that

$$\begin{cases} a_h(\{\mathbf{u}_h, \mathbf{U}_h\}, \{\mathbf{v}_h, \mathbf{V}_h\}) + b_h(\{\mathbf{v}_h, \mathbf{V}_h\}, \{p_h, \pi_h\}) + s_h(\mathbf{v}_h, \pi_h) = r_h(\mathbf{v}_h, \mathbf{V}_h) \\ b_h(\{\mathbf{u}_h, \mathbf{U}_h\}, \{q_h, \tau_h\}) - b_p(p_h, q_h) - b_s(\pi_h, \tau_h) = 0 \end{cases} \tag{254}$$

for all $(\mathbf{v}_h, q_h) \in V^\pm_{0,h} \times Q^\pm_h$ and $(\mathbf{V}_h, \tau_h) \in V_{\Gamma,h} \times Q^0_{\Gamma,h}$. We define all the bilinear forms in (254) for all $\mathbf{u}_h \in V_h^\pm$, $\mathbf{v}_h \in V^\pm_{0,h}$, $\mathbf{U}, \mathbf{V} \in V_{\Gamma,h}$, $p \in L^2(\Omega)$, $\pi \in L^2(\Gamma)$. Let us start from form $a_h(\{\cdot,\cdot\}, \{\cdot,\cdot\})$:

$$\begin{aligned} a_h(\{\mathbf{u}_h, \mathbf{U}_h\}, \{\mathbf{v}_h, \mathbf{V}_h\}) =& a_i(\{\mathbf{u}_h, \mathbf{U}_h\}, \{\mathbf{v}_h, \mathbf{V}_h\}) + a_n(\mathbf{u}_h, \mathbf{v}_h) \\ &+ a_p(\{\mathbf{u}_h, \mathbf{U}_h\}, \{\mathbf{v}_h, \mathbf{V}_h\}) + a_s(\mathbf{U}_h, \mathbf{V}_h), \end{aligned} \tag{255}$$

where we group together the terms that arise from the integration by parts of the divergence of the

stress tensors:

$$
\begin{aligned}
a_i(\{\mathbf{u}_h,\mathbf{U}_h\},\{\mathbf{v}_h,\mathbf{V}_h\}) = {} & 2(\mu^-\mathbf{D}(\mathbf{u}_h^-),\mathbf{D}(\mathbf{v}_h^-))_{\Omega_-} + 2(\mu^+\mathbf{D}(\mathbf{u}_h^+),\mathbf{D}(\mathbf{v}_h^+))_{\Omega_+} \\
& + \langle f^-(\mathbf{P}\mathbf{u}_h^- - \mathbf{U}_h), \mathbf{P}\mathbf{v}_h^- - \mathbf{V}_h\rangle_\Gamma + \langle f^+(\mathbf{P}\mathbf{u}_h^+ - \mathbf{U}_h), \mathbf{P}\mathbf{v}_h^+ - \mathbf{V}_h\rangle_\Gamma \\
& - 2\langle\{\mu\mathbf{n}^T\mathbf{D}(\mathbf{u}_h)\mathbf{n}\},[\mathbf{v}_h\cdot\mathbf{n}]\rangle_\Gamma + 2(\mu_\Gamma\mathbf{D}_\Gamma(\mathbf{U}_h),\mathbf{D}_\Gamma(\mathbf{V}_h))_\Gamma
\end{aligned} \tag{256}
$$

the terms that enforce condition (230) weakly using Nitsche's method

$$
a_n(\mathbf{u}_h,\mathbf{v}_h) = \sum_{T\in\mathcal{T}_h^\Gamma}\frac{\gamma}{h_T}\{\mu\}([\mathbf{u}_h\cdot\mathbf{n}],[\mathbf{v}_h\cdot\mathbf{n}])_\Gamma - 2\langle\{\mu\mathbf{n}^T\mathbf{D}(\mathbf{v})\mathbf{n}\},[\mathbf{u}_h\cdot\mathbf{n}]\rangle_\Gamma, \tag{257}
$$

and the stabilization and penalty terms:

$$
a_p(\{\mathbf{u}_h,\mathbf{U}_h\},\{\mathbf{v}_h,\mathbf{V}_h\}) = \mathbf{J}_h^-(\mathbf{u}_h,\mathbf{v}_h) + \mathbf{J}_h^+(\mathbf{u}_h,\mathbf{v}_h) + \tau_s(\mathbf{U}_h\cdot\mathbf{n},\mathbf{V}_h\cdot\mathbf{n})_\Gamma, \tag{258}
$$

$$
\mathbf{J}_h^\pm(\mathbf{u}_h,\mathbf{v}_h) = \sum_{\ell=1}^{k+1}|e|^{2\ell-1}\sum_{e\in\mathcal{E}_h^{\Gamma,\pm}}\gamma_{\mathbf{u}}^\pm\mu^\pm([\partial_n^\ell\mathbf{u}_h^\pm],[\partial_n^\ell\mathbf{u}_h^\pm])_e. \tag{259}
$$

In (259), $\partial_n^\ell\mathbf{u}_h^-$ denotes the derivative of order ℓ of $\mathbf{u}_h^-$ in the direction of $\mathbf{n}$. The $\mathbf{J}_h$ terms in (258) are so called ghost-penalty stabilization [14, 15] included to avoid poorly conditioned algebraic systems due to possible small cuts of tetrahedra from $\mathcal{T}_h^\Gamma$ by the interface. The terms in (260) and (262) have the same role for the surface bilinear forms.

The last form in (255) is related to the algebraic stability of the surface Stokes problem:

$$
a_s(\mathbf{U}_h,\mathbf{V}_h) = \rho_{\mathbf{u}}(\nabla\mathbf{u}_h\mathbf{n},\nabla\mathbf{v}_h\mathbf{n})_{\Omega_h^\Gamma}. \tag{260}
$$

Similarly, the terms coming from the integration by parts of the divergence of the stress tensors

are contained in

$$b_h(\{\mathbf{v}_h, \mathbf{V}_h\}, \{p_h, \pi_h\}) = -(p_h^-, \operatorname{div} \mathbf{v}_h^-)_{\Omega_-} - (p_h^+, \operatorname{div} \mathbf{v}_h^+)_{\Omega_+} + \langle \{p_h\}, [\mathbf{v}_h \cdot \mathbf{n}] \rangle_\Gamma + (\nabla_\Gamma \pi_h, \mathbf{V}_h)_\Gamma, \tag{261}$$

the penalty terms are grouped together in

$$b_p(p_h, q_h) = J_h^-(p_h, q_h) + J_h^+(p_h, q_h), \quad J_h^\pm(p_h, q_h) = \frac{\gamma_p^\pm}{\mu^\pm} \sum_{e \in \mathcal{E}_h^{\Gamma,\pm}} \sum_{\ell=1}^{k} |e|^{2\ell+1} ([\partial_n^\ell p_h^\pm], [\partial_n^\ell q_h^\pm])_e,$$

and we have a term related to algebraic stability of the surface Stokes problem in:

$$b_s(\pi_h, \tau_h) = \rho_p (\nabla p_h \cdot \mathbf{n}, \nabla p_h \cdot \mathbf{n})_{\Omega_h^\Gamma}. \tag{262}$$

Finally,

$$\begin{aligned} s_h(\mathbf{v}_h, \pi_h) =& -\langle \pi_h \kappa, \langle \mathbf{v}_h \cdot \mathbf{n} \rangle \rangle_\Gamma, \\ r_h(\mathbf{v}_h, \mathbf{V}_h) =& (\mathbf{f}_h^-, \mathbf{v}_h^-)_{\Omega_-} + (\mathbf{f}_h^+, \mathbf{v}_h^+)_{\Omega_+} + (\mathbf{P}\mathbf{b}_h^e, \mathbf{V}_h)_\Gamma. \end{aligned}$$

We recall that some of the interface terms in $a_i(\{\cdot,\cdot\}, \{\cdot,\cdot\})$ and $b_h(\{\cdot,\cdot\}, \{\cdot,\cdot\})$ have been obtained using relationship (158).

Parameters $\gamma_{\mathbf{u}}^\pm$, $\gamma_p^\pm$, and γ are all assumed to be independent of $\mu^\pm$, h, and the position of Γ against the underlying mesh. Parameter γ in (257) needs to be large enough to provide the bilinear form $a_h(\{\cdot,\cdot\}, \{\cdot,\cdot\})$ with coercivity. Parameters $\gamma_{\mathbf{u}}^\pm$ and $\gamma_p^\pm$ can be tuned to improve the numerical performance of the method. As for the parameters required by the discretization of the surface Stokes problem, we allow:

$$\tau_s = c_\tau h^{-2}, \quad \rho_p = c_p h, \quad \rho_{\mathbf{u}} \in [c_{\mathbf{u}} h, C_{\mathbf{u}} h^{-1}], \tag{263}$$

where c_τ, c_p, $c_{\mathbf{u}}$, and $C_{\mathbf{u}}$ are positive constants independent of h and how Γ cuts the bulk mesh.

The definition of bilinear forms requires integration over $\Gamma \cap T$ and $T \cap \Omega^{\pm}$ for T from Ω_h^Γ. In general, there are no exact quadrature formulas to accomplish this task [80]. In practice, approximations should be made which introduce geometric errors. To keep these geometric errors of the order consistent with the approximation properties of the finite element spaces, we use isoparametric variants of the above spaces introduced in [58]; see also [61, 35].

We expect that the stability of the finite element formulation can be analyzed largely following the same steps of the well-posedness analysis for the weak formulation in Sec. 3.1.4, with a special treatment of cut elements, Nitsche terms and surface elements as available in the literature for bulk Stokes interface and surface Stokes problems.

3.3 A partitioned method for the coupled bulk-surface flow

For the solution of the coupled problem described in Sec. 3.1.2 we intend to use a partitioned strategy, i.e. each sub-problem is solved separately and the coupling conditions are enforced in an iterative fashion. Partitioned method are appealing for solving coupled problems because they allow to reuse existing solvers with minimal modifications. In order to devise such a method for the simplified problem in Sec. 3.1.2, let us take a step back and look at the original problem (205).

Discretize problem (205) in time with, e.g., the Backward Euler method and consider the coupled problem at a particular time $t = t^{n+1}$. Let S_b be the map that associates the jump in the normal stress across the interface to any given surface flow velocity $\mathbf{U} = \mathbf{U}_T + U_N\mathbf{n}$:

$$S_b(\mathbf{U}) = [\boldsymbol{\sigma}\mathbf{n}]_-^+ = \boldsymbol{\sigma}^+(\mathbf{u}^+, p^+)\mathbf{n} - \boldsymbol{\sigma}^-(\mathbf{u}^-, p^-)\mathbf{n} \quad \text{on } \Gamma,$$

where $(\mathbf{u}^+, p^+)$ and $(\mathbf{u}^-, p^-)$ represent the solution of the two-phase time-discrete Navier-Stokes problem at time t associated to (206)–(207) endowed with interface conditions (210), (212), and (213). Moreover, let S_s be the operator associated to the surface flow such that to any given surface

flow velocity $\mathbf{U}$ it associates the load $\mathbf{f}_\Gamma$:

$$S_s(\mathbf{U}) = \mathbf{f}_\Gamma \quad \text{on } \Gamma,$$

through the time-discrete surface Navier-Stokes problem at time t associated to (208)–(209). Note that S_b and S_s are nonlinear and their definitions can involve also forcing terms and, in the case of the bulk fluid problem, terms due to the boundary conditions. For the surface operator, we can define S_s^{-1} as the map that associates the surface flow velocity $\mathbf{U}$ to any given load $\mathbf{f}_\Gamma$ on Γ.

With the above definitions, we can express the time discrete version of coupled problem (205) in terms of the solution $\mathbf{U}$ of a nonlinear equation defined only on Γ. This interface equation is usually presented in one of three formulations that are equivalent from the mathematical point of view, but give rise to different iterative algorithms. The first and perhaps most used formulation is the fixed-point one: Find $\mathbf{U}$ such that

$$S_s^{-1}(S_b(\mathbf{U})) = \mathbf{U} \quad \text{on } \Gamma. \tag{264}$$

The second formulation is a slight modification of (264), which lends itself to a Newton iterative method: Find $\mathbf{U}$ such that

$$S_s^{-1}(S_b(\mathbf{U})) - \mathbf{U} = \mathbf{0} \quad \text{on } \Gamma.$$

The third approach is given by the Steklov-Poincaré equation: Find $\mathbf{U}$ such that

$$S_b(\mathbf{U}) - S_s(\mathbf{U}) = \mathbf{0} \quad \text{on } \Gamma.$$

See, e.g., [85] for more details on these three formulations.

A standard algorithm for eq. (264) uses fixed-point iterations: Given $\mathbf{U}^k$, compute

$$\mathbf{U}^{k+1} = \mathbf{U}^k + \omega^k(\overline{\mathbf{U}}^k - \mathbf{U}^k) \quad \text{with } \overline{\mathbf{U}}^k = S_s^{-1}(S_b(\mathbf{U}^k)). \tag{265}$$

The choice of the relaxation parameter ω^k determines the efficiency of the algorithm or it might be crucial for convergence in certain ranges of the physical parameters. An effective strategy for setting ω^k is the Aitken's acceleration method.

For simplicity, we present algorithm (265) applied to the time discrete version of coupled problem (205) with $\omega^k = 1$ for all k (i.e., no relaxation). At time $t = t^{n+1}$, assuming that $\mathbf{U}^k$ is known, perform the following steps:

- **Step 1**: solve the two-phase time-discrete Navier-Stokes problem at time t associated to (206)–(207) for the bulk flow variables $(\mathbf{u}^-_{k+1}, p^-_{k+1})$ and $(\mathbf{u}^+_{k+1}, p^+_{k+1})$ with interface conditions

$$\begin{aligned}
&\mathbf{u}^+_{k+1} \cdot \mathbf{n} = U^k_N = \mathbf{u}^-_{k+1} \cdot \mathbf{n} && \text{on } \Gamma \\
&\mathbf{P}\boldsymbol{\sigma}^+_{k+1}\mathbf{n} = f^+(\mathbf{P}\mathbf{u}^+_{k+1} - \mathbf{U}^k_T) && \text{on } \Gamma, \\
&\mathbf{P}\boldsymbol{\sigma}^-_{k+1}\mathbf{n} = -f^-(\mathbf{P}\mathbf{u}^-_{k+1} - \mathbf{U}^k_T) && \text{on } \Gamma.
\end{aligned}$$

- **Step 2**: solve the time-discrete surface Navier-Stokes problem at time t associated to (208)–(209) for variables $(\mathbf{U}^{k+1}, \pi^{k+1})$ with interface condition

$$\mathbf{f}^{k+1}_\Gamma = [\boldsymbol{\sigma}_{k+1}\mathbf{n}]^+_- \qquad \text{on } \Gamma.$$

- **Step 3**: Check the stopping criterion

$$||\mathbf{U}^{k+1} - \mathbf{U}^k||_\Gamma < \epsilon ||\mathbf{U}^k||_\Gamma,$$

  where ϵ is a given stopping tolerance.

Notice that the bulk and surface flow problems are solved separately and sequentially. In general, this algorithm is easy to implement but convergence could be slow in certain ranges of the physical parameters and require relaxation for speed-up.

The above algorithm adapted to simplified problem (225)–(231), reads as follows. At iteration

$k+1$, assuming that $(\mathbf{U}_T^k, \pi^k)$ are known, perform the following steps:

- **Step 1**: solve two-phase problem (225)–(226) for the bulk flow variables $(\mathbf{u}_{k+1}^-, p_{k+1}^-)$ and $(\mathbf{u}_{k+1}^+, p_{k+1}^+)$ with interface conditions

$$\mathbf{u}_{k+1}^+ \cdot \mathbf{n} = \mathbf{u}_{k+1}^- \cdot \mathbf{n} \qquad \text{on } \Gamma \tag{266}$$

$$\mathbf{P}\boldsymbol{\sigma}_{k+1}^+ \mathbf{n} = f^+(\mathbf{P}\mathbf{u}_{k+1}^+ - \mathbf{U}_T^k) \qquad \text{on } \Gamma, \tag{267}$$

$$\mathbf{P}\boldsymbol{\sigma}_{k+1}^- \mathbf{n} = -f^-(\mathbf{P}\mathbf{u}_{k+1}^- - \mathbf{U}_T^k) \qquad \text{on } \Gamma, \tag{268}$$

$$\left[\mathbf{n}^T \boldsymbol{\sigma}_{k+1} \mathbf{n}\right]_+^- = \pi^k \kappa \qquad \text{on } \Gamma. \tag{269}$$

- **Step 2**: solve surface flow problem (227)–(228) for variables $(\mathbf{U}_T^{k+1}, \pi^{k+1})$ with interface condition

$$\mathbf{P}\mathbf{f}_\Gamma^{k+1} = [\mathbf{P}\boldsymbol{\sigma}_{k+1}\mathbf{n}]_-^+ \qquad \text{on } \Gamma. \tag{270}$$

- **Step 3**: Check the stopping criterion

$$||\mathbf{U}_T^{k+1} - \mathbf{U}_T^k||_\Gamma < \epsilon ||\mathbf{U}_T^k||_\Gamma. \tag{271}$$

Notice that only interface condition (267)–(270) are coupling conditions for bulk and surface flows. If one was to compute the load exerted on the surface fluid in (270) directly from the solution of the problem at Step 1, the overall accuracy of the method would be spoiled. Instead, one can compute $\mathbf{P}\mathbf{f}_\Gamma^{k+1}$ by plugging (267)–(268) into (270):

$$\mathbf{P}\mathbf{f}_\Gamma^{k+1} = f^+ \mathbf{P}\mathbf{u}_{k+1}^+ + f^- \mathbf{P}\mathbf{u}_{k+1}^- - (f^+ + f^-)\mathbf{U}_T^k \qquad \text{on } \Gamma.$$

However, we prefer to use a more implicit version of the above condition:

$$\mathbf{P}\mathbf{f}_{\Gamma}^{k+1} = f^{+}\mathbf{P}\mathbf{u}_{k+1}^{+} + f^{-}\mathbf{P}\mathbf{u}_{k+1}^{-} - (f^{+} + f^{-})\mathbf{U}_{T}^{k+1} \qquad \text{on } \Gamma.$$

since it could help have a better control of approximate rigid rotations (Killing vector fields).

3.4 Numerical examples

The aim of the numerical results collected in this section is to provide evidence of the robustness of the proposed finite element approach with respect to the contrast in viscosity in the bulk fluid, surface fluid viscosity, value of the slip coefficients, and position of the interface relative to the fixed computational mesh.

For the averages in (157), we set $\alpha = 0$ and $\beta = 1$ for all the numerical experiments since we have $\mu_{-} \leq \mu_{+}$. In addition, we set $\gamma_{\mathbf{u}}^{\pm} = 0.05$, $\gamma_{p}^{\pm} = 0.05$, and $\gamma = 80$. The value of all other parameters will depend on the specific test. The stopping tolerance for criterion (271) is set to $\epsilon = 10^{-6}$. For all the simulations, we choose to use finite element pair $\mathbf{P}_2 - P_1$ for both the bulk and surface fluid problems.

For all the results presented below, we will report the L^2 error and a weighted H^1 error for the bulk velocity defined as

$$\left(2\mu_{-}\|D(\mathbf{u} - \mathbf{u}_h^{-})\|_{\Omega^{-}}^2 + 2\mu_{+}\|D(\mathbf{u} - \mathbf{u}_h^{+})\|_{\Omega^{+}}^2\right)^{\frac{1}{2}}, \tag{272}$$

and a weighted L^2 error for the bulk pressure defined as

$$\left(\mu_{-}^{-1}\|p - p_h^{-}\|_{\Omega^{-}}^2 + \mu_{+}^{-1}\|p - p_h^{+}\|_{\Omega^{+}}^2\right)^{\frac{1}{2}}. \tag{273}$$

Such weighted norm naturally arise in the error analysis of the Stokes interface problem [78]. In addition, we will report the L^2 and H^1 errors for the surface velocity and L^2 error for the surface pressure.

3.4.1 Sphere embedded in a cube

We perform a series of tests where domain Ω is the cube $[-1.5, 1.5]^3$ and interface Γ is the unit sphere centered at the origin. Let $\mathbf{x} = (x, y, z) \in \Omega$. Surface Γ is characterized as the zero level set of function $\phi(\mathbf{x}) = ||\mathbf{x}||_2^2 - 1$. We consider the following solution for the bulk flow:

$$p^- = 3x\sqrt{x^2+y^2+z^2} - 2x(x^2+y^2+z^2), \quad \mathbf{u}^- = \frac{2f^-}{f^- - \mu^-}\mathbf{a}(x,y,z), \tag{274}$$

$$p^+ = 6x\sqrt{x^2+y^2+z^2} - 4x(x^2+y^2+z^2), \quad \mathbf{u}^+ = \frac{2f^+}{f^+ + \mu^+}\mathbf{a}(x,y,z), \tag{275}$$

where

$$\mathbf{a}(x,y,z) = \left(\frac{3}{2} - \sqrt{x^2+y^2+z^2}\right)\begin{bmatrix} (-y-z)x + y^2 + z^2 \\ (-x-z)y + x^2 + z^2 \\ (-x-y)z + y^2 + x^2 \end{bmatrix},$$

coupled to the following exact solution for the surface flow:

$$\pi = x, \quad \mathbf{U} = \begin{bmatrix} (-y-z)x + y^2 + z^2 \\ (-x-z)y + x^2 + z^2 \\ (-x-y)z + y^2 + x^2 \end{bmatrix}, \tag{276}$$

The forcing terms $\mathbf{f}^-$ and $\mathbf{f}^+$ are found by plugging the solution (274)–(275) in (140). We impose a Dirichlet condition (215) on the faces $x = 1.5$, $y = -1.5$, $z = -1.5$, where function $\mathbf{g}$ is found from $\mathbf{u}^+$ in (275). On the remaining part of the boundary, we impose a Neumann condition (216) where $\mathbf{f}_N$ is found from p^+ in (274) and $\mathbf{u}^+$ in (275).

The value of the physical parameters will be specified for each test.

Spatial convergence. To check the spatial accuracy of the finite element method described in Sec. 3.2, we consider exact solution (274)–(276) with viscosities $\mu^- = 1$, $\mu^+ = 10$ and $\mu_\Gamma = 1$, and friction coefficients $f^- = 2$ and $f^+ = 10$. Notice that the fluid outside the sphere has a larger

viscosity than the fluid inside the sphere, which has the same viscosity as the surface fluid. We consider structured meshes of tetrahedra with five levels of refinement, the coarsest mesh having mesh size $h = 0.5$ while the finest mesh has $h = 0.05$. All the meshes feature a local one-level refinement near the corners of Ω. Table 1 reports the number of DOFs for each mesh. Fig. 9 (left) shows the L^2 error and weighted H^1 error (198) for the bulk velocity, weighted L^2 error (199) for the bulk pressure, L^2 and H^1 errors for the surface velocity and L^2 error for the surface pressure against the mesh size h. We observe optimal convergence rates for all the norms under consideration. Fig. 9 (right) shows the number of bulk-surface iterations to satisfy stopping criterion (271) as h varies. As we can see, the number of iterations is fairly insensitive to a mesh refinement or coarsening.

h	0.5	0.25	0.125	0.0625	0.05
# bulk velocity DOFs	1.1e4	7.4e4	5.2e5	3.6e6	6.4e6
# bulk pressure DOFs	6.2e2	3.7e3	2.3e4	1.6e5	2.8e5
# surface velocity DOFs	2.4e3	1.0e4	4.0e4	1.5e5	2.2e5
# surface pressure DOFs	1.4e2	5.9e2	2.3e3	8.5e3	1.3e4

Table 1: Sphere: DOFs for bulk and surface variables for all the meshes under consideration in the spatial convergence test.

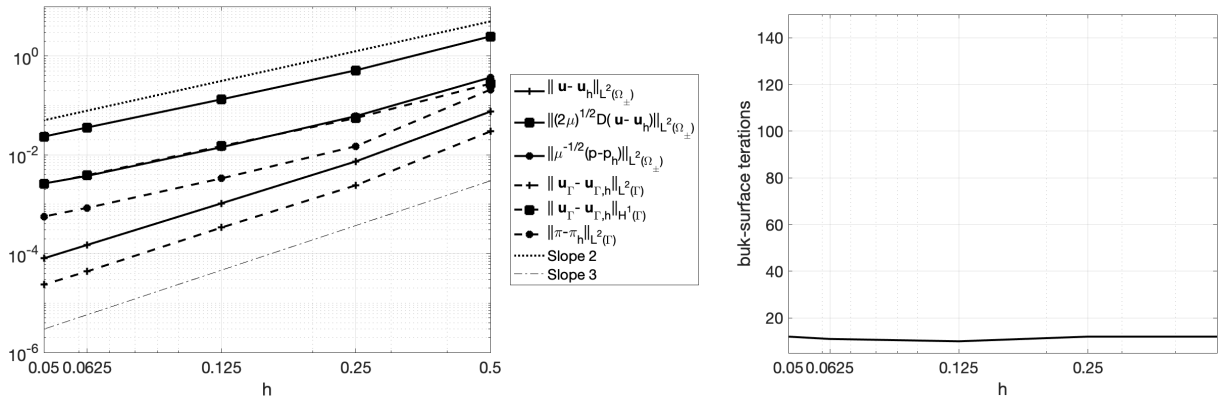

Figure 9: Sphere: (left) Bulk and surface FE errors against the mesh size h. (right) Number of bulk-surface iterations of the partitioned method as h varies.

Robustness with respect to the viscosity contrast. It is known that the case of high contrast for the viscosities in a two-phase problem is especially challenging from the numerical point of view. To test the robustness of our approach with respect to the viscosity contrast in the bulk, we consider exact solution (274)–(276) and fix $\mu^- = 1$, while we let μ^+ vary from 1 to 256. We set $\mu_\Gamma = 1$ and friction coefficients $f^- = 2$ and $f^+ = 10$.

We consider one of the meshes adopted for the previous sets of simulations (with $h = 0.125$). Fig. 10 (left) shows the L^2 error and weighted H^1 error (272) for the bulk velocity, weighted L^2 error (273) for the bulk pressure, L^2 and H^1 errors for the surface velocity and L^2 error for the surface pressure against the value of μ^+. We see that the errors remain mostly unchanged as μ^+ varies, with the exception of the weighted L^2 error for the bulk pressure, which decreases as μ^+ increases. In [75], which focuses only on two-phase bulk flow, we found that such error reaches a plateau as μ^+ is further increased. Fig. 10 (left) shows that our approach is substantially robust with respect to the viscosity contrast μ^+/μ^-.

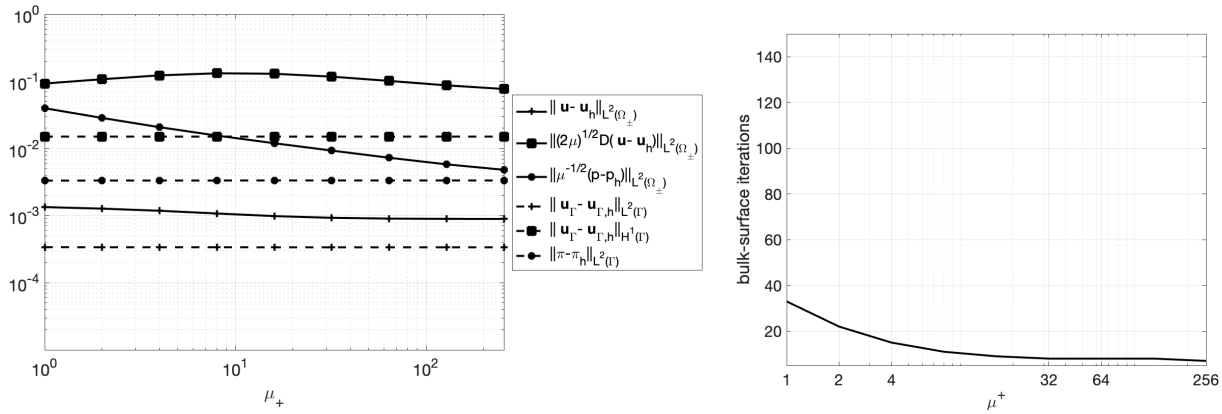

Figure 10: Sphere: (left) Bulk and surface FE errors against the value of μ^+. (right) Number of bulk-surface iterations of the partitioned method as μ^+ varies.

Fig. 10 (right) reports the number of bulk-surface iterations to satisfy stopping criterion (271) as μ^+ varies. We observe that the number of iterations increases as the μ^+/μ^- ratio decreases, indicating that the coupled bulk-surface problem becomes more stiff as μ^+ decreases to match μ^- and μ_Γ.

Robustness with respect to the value of the surface viscosity. We now let μ_Γ vary from 1 to 256 and keep all the other physical parameters fixed to the following values: $\mu^- = 1$, $\mu^+ = 10$, $f^- = 2$ and $f^+ = 10$. Again, we consider exact solution (274)–(276) and the mesh with mesh size $h = 0.125$. Fig. 11 (left) shows all the errors we have considered so far against the value of μ_Γ. We notice that all the bulk errors stay constant as μ_Γ varies. The L^2 errors for the surface velocity and pressure increase as μ_Γ increases, while the H^1 error for the surface velocity slightly decreases as μ_Γ increases. This experiment suggests that more viscous embedded layer is less controlled by the bulk fluid which effects the numerical stability of the complete system. In a water – lipid membrane system, the ratio of lateral dynamic viscosities of the embedded bi-layer and bulk water is typically 1–10 μm (depending on the temperature and composition) with the size of a vesicle being generally between 0.1 and 10 μm. Hence the observed increase of the numerical error does not look critical for this application.

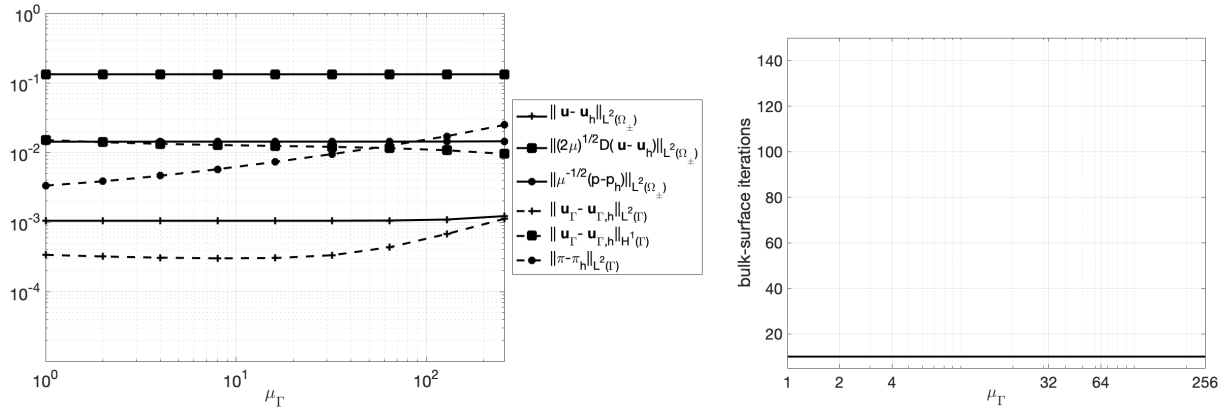

Figure 11: Sphere: (left) Bulk and surface FE errors against the value of μ_Γ. (right) Number of bulk-surface iterations of the partitioned method as μ_Γ varies.

Fig. 11 (right) shows the number of bulk-surface iterations to satisfy stopping criterion (271) as μ_Γ varies. Our partitioned method seems to be insensitive to a variation in the value of μ_Γ. In particular, for the range of μ_Γ under consideration the number of iterations stays constant and equal to 12.

Robustness with respect to the slip coefficients. To check the sensitivity of the errors

and partitioned method to the value of the slip coefficients, we run two sets of experiments, both involving exact solution (274)–(276). In the first set we fix $f^+ = 2$ and vary f^- from 1 to 256, while in the second set we take $f^+ = f^-$ and let them both vary from 1 to 256 . The viscosities are set as follows: $\mu^- = 1$, $\mu^+ = 10$, and $\mu_\Gamma = 1$. We consider again the mesh with mesh size $h = 0.125$. Fig. 12 (left) and 13 (left) show all the errors under consideration against the value of the slip coefficient(s) for both sets of tests. The only error that shows a substantial variation is the weighted H^1 error the bulk velocity, which increases as the slip coefficient(s) increase. However, such error seems to reach a plateau in both cases.

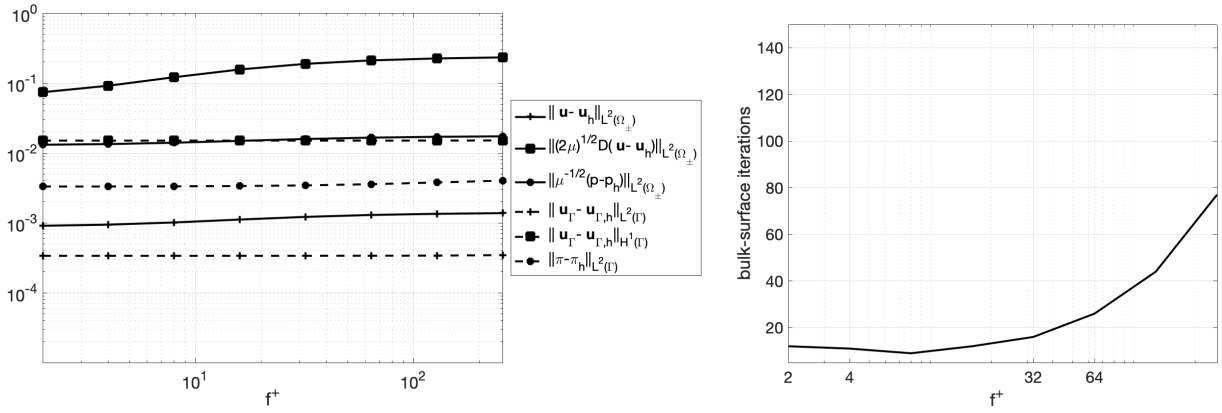

Figure 12: Sphere: (left) Bulk and surface FE errors against the value of f^+. (right) Number of bulk-surface iterations of the partitioned method as f^+ varies.

Fig. 12 (right) and 13 (right) report the number of bulk-surface iterations to satisfy stopping criterion (271) as the value of the coefficient(s) varies for both sets of tests. In Fig. 12 (right), we see a rather sharp increase in the number of iterations as f^- increases. This is even more true when both slip coefficients are increased together, as we can see from Fig. 13 (right). Fig. 14 reports the relative difference of the surface velocity between subsequent iterations in L^2 norm until stopping criterion (271) is met for $f^+ = f^- = 2^2$ and $f^+ = f^- = 2^8$. We see that such relative difference decreases regularly for $f^+ = f^- = 2^2$, while for $f^+ = f^- = 2^8$ it decreases quickly for the first few iterations and then it slows down. A heuristic explanation we have for this is that as the two friction coefficients increase interface conditions (212)–(213) become close to Dirichlet conditions,

making the surface flow more "passive". Thus, separating the surface flow from the bulk flow as in the partitioned algorithm might not make much sense.

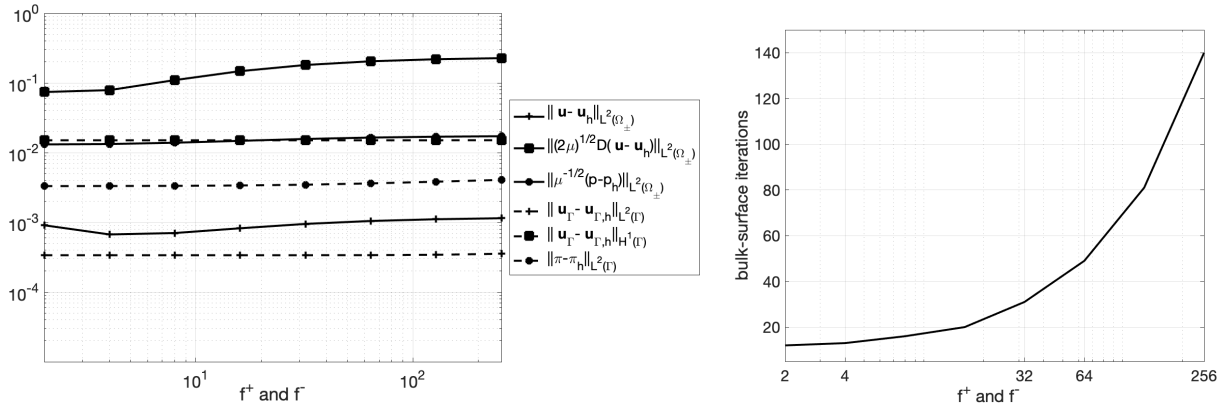

Figure 13: Sphere: (left) Bulk and surface FE errors against the value of $f^+ = f^-$. (right) Number of bulk-surface iterations of the partitioned method as the value of f^+ and f^- (with $f^+ = f^-$) varies.

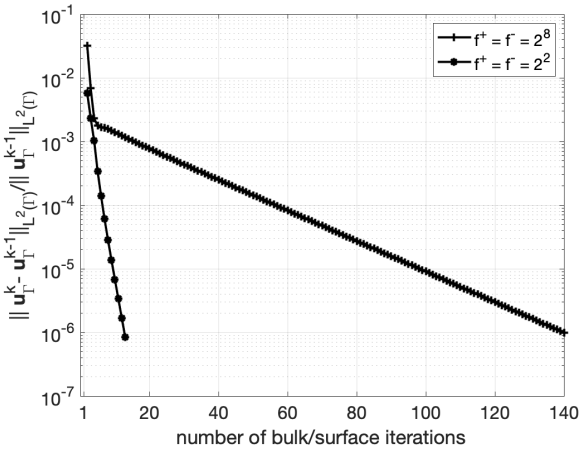

Figure 14: Sphere: relative difference of the surface velocity between subsequent iterations in L^2 norm until stopping criterion (271) is met.

3.4.2 Torus embedded in a cube

The domain Ω is cube $[-2,2]^3$ and surface Γ is a torus centered at $\mathbf{c} = (c_1, c_2, c_3)$. Let $(x, y) = (\tilde{x} - c_1, \tilde{y} - c_2, \tilde{z} - c_3)$, $(\tilde{x}, \tilde{y}, \tilde{z}) \in \Omega$. We can characterize Γ as the zero level set of function $\phi(\mathbf{x}) = \sqrt{z^2 + (\sqrt{x^2+y^2} - 1)^2} - \frac{1}{2}$. Finding an exact solution problem (225)–(229), (212), and (213) with this more complicated surface is highly non-trivial. To simplify the task, we relax interface conditions (212), (213), and (229) as follows:

$$\begin{aligned} \mathbf{P}\boldsymbol{\sigma}^{\pm}\mathbf{n} &= \pm f^{\pm}(\mathbf{P}\mathbf{u}^{\pm} - \mathbf{U}) + g^{\pm} && \text{on } \Gamma, \\ \left[\mathbf{n}^T\boldsymbol{\sigma}\mathbf{n}\right]_+^- &= \pi\kappa + g^n && \text{on } \Gamma. \end{aligned}$$

where g^+, g^-, and g^n are computed such that exact solution given below satisfy these relaxed interface conditions. The solution is given by

$$p^- = \left(\frac{1}{2} - \frac{2 - 4\sqrt{x^2+y^2}}{\sqrt{x^2+y^2}}\right)(x^3 + x),\ p^+ = \frac{1}{2}(x^3 + x),\ \mathbf{u}^- = \mathbf{u}^+ = \begin{bmatrix} x^2 y \\ 5 - xy^2 + z^2 \\ -xy \end{bmatrix}, \tag{277}$$

for the bulk and:

$$\pi = x^3 + x, \quad \mathbf{U} = \left[\frac{-zx}{\sqrt{x^2+y^2}},\ \frac{-zy}{\sqrt{x^2+y^2}},\ \sqrt{x^2+y^2} - 1\right]^T, \tag{278}$$

for the surface. The forcing terms $\mathbf{f}^-$ and $\mathbf{f}^+$ are found by plugging the solution (277)–(278) in (225). We impose a Dirichlet condition (215) on the faces $x = 2$, $y = -2$, $z = -2$, where function $\mathbf{g}$ is found from $\mathbf{u}^+$ in (277). On the remaining part of the boundary, we impose a Neumann condition (216) where $\mathbf{f}_n$ is found from p^+ and $\mathbf{u}^+$ in (277).

Spatial convergence. Once again, we start by checking spatial accuracy. To this end, we consider exact solution (277)–(278) with $\mathbf{c} = (0, 0, 0)$, viscosities $\mu^- = 1$, $\mu^+ = 10$, $\mu_\Gamma = 1$, and friction coefficients $f^- = 2$ and $f^+ = 10$. Just like in the case of the sphere, we consider structured meshes

of tetrahedra that feature a local one-level refinement near the corners of Ω. The details of the meshes under consideration are reported in Table 2. Fig. 15 shows the L^2 error and weighted H^1 error (272) for the bulk velocity, weighted L^2 error (273) for the bulk pressure, L^2 and H^1 errors for the surface velocity and L^2 error for the surface pressure against the mesh size h. Also for this second convergence test, we observe optimal convergence rates for all the norms.

h	0.25	0.125	0.0625	0.05
# bulk velocity DOFs	1.6e5	1.2e6	8.5e6	1.5e7
# bulk pressure DOFs	7.6e3	5.4e4	3.7e5	6.7e5
# surface velocity DOFs	1.6e4	6.0e4	2.3e5	3.4e5
# surface pressure DOFs	9.0e2	3.4e3	1.3e4	2.0e4

Table 2: Torus: DOFs for bulk and surface variables for all the meshes under consideration in the spatial convergence test.

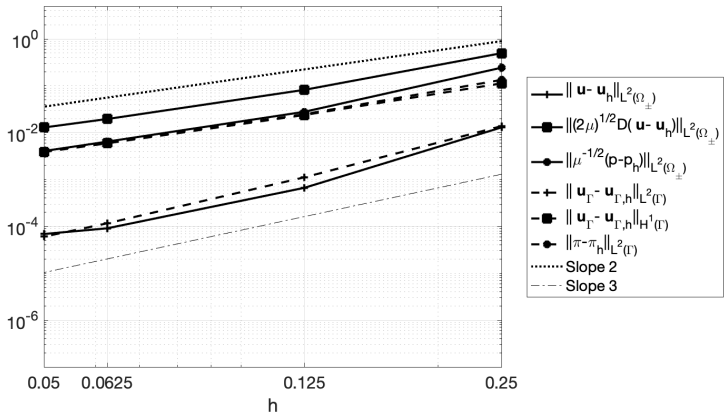

Figure 15: Torus: Bulk and surface FE errors against the mesh size h.

Robustness with respect to the position of the interface. We conclude our series of numerical results with a set of simulations aimed at checking that our approach is not sensitive to the position of the interface with respect to the background mesh. We vary the center $\mathbf{c} = (c_1, c_2, c_3)$

of the torus that represents Γ:

$$c_1 = h\frac{k}{20}\sin\left(\frac{k\pi}{10}\right),\ c_2 = h\frac{k\sqrt{2}}{40}\cos\left(\frac{k\pi}{10}\right),\ c_3 = h\frac{k\sqrt{2}}{40}\cos\left(\frac{k\pi}{10}\right), \tag{279}$$

where h is the mesh size. The physical parameters are set like in the convergence test. We consider the mesh in Table 2 with $h = 0.125$. Fig. 16 shows all the errors against the value of k in (279). We see that all the errors are fairly insensitive to the position of Γ with respect to the background mesh, indicating robustness.

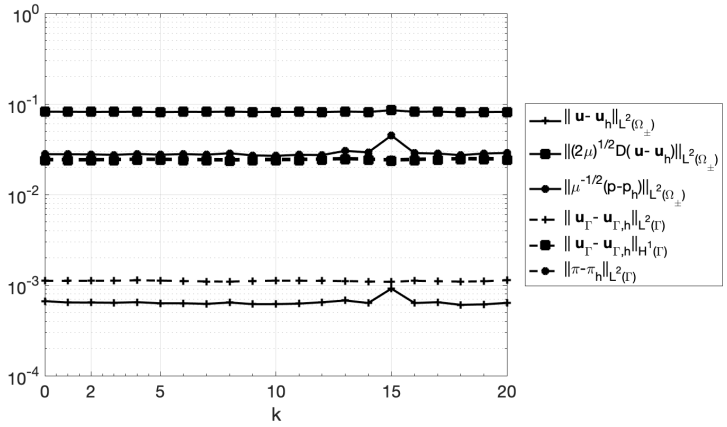

Figure 16: Torus: Bulk and surface FE errors against the value of k in (279).

4 Neural Network Prediction of the Pattern Formation Driven by the Cahn-Hilliard Model of Phase Separation

Motivated by its critical role in a variety of cellular processes, over the past decades, cell membranes phase separation has become an important research topic. In fact, lipid-driven separation of immiscible liquid phases likely plays an important role in the formation of rafts in cell membranes [95, 101]. Lipid rafts in eukaryotic cells have been related to important biological processes such as adhesion, signaling, and protein transport, see Figure 17. However, due to the frail nature of giant cell membranes, experimental investigation of dynamics of phase separation and pattern formation often proved to be challenging. Computational studies help observe and gain insights into dynamics for pattern formation. This chapter is focused on predicting statistics that characterized the dynamics of pattern formation during the lateral phase separation in multicomponent lipid bi-layer modeled by the Cahn-Hilliard equations.

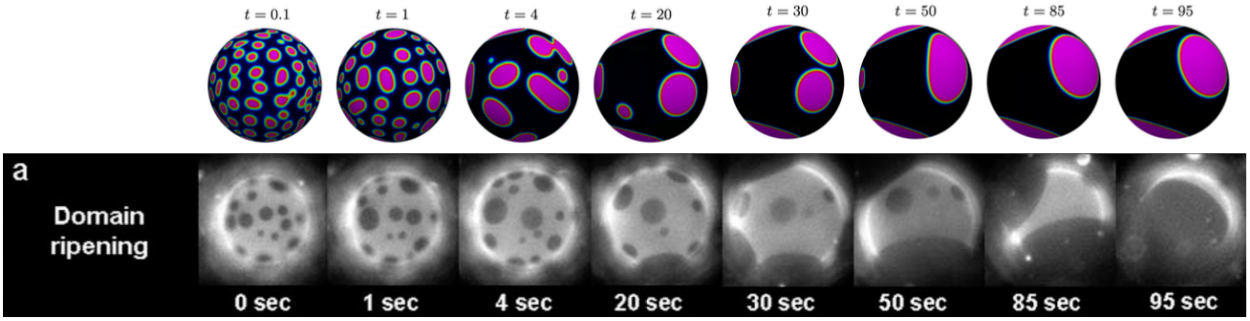

Figure 17: Upper: Simulation with a surface Cahn-Hilliard model from [110], Bottom: Phase organization in a giant unilamellar vesicle (GUV) [101].

A computationally efficient neural network is proposed in this chapter to complement numerical experimental investigations. The method relies on reservoir computing [98]. The results show that our neural network approach delivers promising quantitative predictions about the dynamics of the membrane organizations. In particular, the neural network prediction results and numerical results that are in good agreement.

4.1 Problem description

Consider a stationary domain Γ to be a unit sphere immersed in a cube Γ, representing a cell membranes. Consider the surface Cahn-Hilliard equation on Γ derived in Sec. 1.5. Recall the surface Cahn-Hilliard equation on a surface Γ, which governs the evolution of concentration $c = c(t, \mathbf{x})$ in time t, $\mathbf{x} \in \Gamma \subset \mathbb{R}^3$ [18, 19],

$$\frac{\partial c}{\partial t} + \operatorname{div}_\Gamma(M_c \nabla_\Gamma(f_0'(c) - \epsilon^2 \triangle_\Gamma c)) = 0 \qquad \text{on } \Gamma(t),\ t \in [0, T] \tag{280}$$

with initial conditions,

$$c(\cdot, t) = c_0 \text{ on } \Gamma(0) \tag{281}$$

where $c_0 = c_0(\mathbf{x})$ is an initial distribution of concentration, corresponding to a homogenous mixture and $f_0(c) = \frac{1}{4}c^2(1-c)^2$. Parameter $\epsilon > 0$ defines the width of the diffuse interface between the phases. Finally we consider the mobility coefficient M_c of the form

$$M_c = Dc(1-c) \tag{282}$$

with diffusion coefficient $D > 0$. To model an initially homogenous liposome, the initial concentration c_0 is defined as a Bernoulli random distribution with mean a_{raft}. We set:

$$c_0 := c_{rand}(\mathbf{x}) \text{ for active mesh nodes } \mathbf{x} \tag{283}$$

with $c_{rand} \sim Bernoulli(a_{raft})$, $a_{raft} = 0.1$.

We discretize the system (280) by the trace finite element method. As introduced in [110], the first step is to introduce an equivalent integral form of the surface Cahn-Hilliard system, also known as weak formulation. The weak formulation of the Cahn-Hilliard equation (280) reads: Find

concentration c and chemical potential μ such that

$$\int_\Gamma \frac{\partial c}{\partial t} v \; ds + \int_\Gamma M_c \nabla_\Gamma \mu \nabla_\Gamma v \; ds = 0 \tag{284}$$

$$\int_\Gamma \mu q \; ds - \int_\Gamma f_0'(c) q \; ds - \int_\Gamma \epsilon^2 \nabla_\Gamma c \nabla_\Gamma q \; ds = 0 \tag{285}$$

for any sufficiently regular test functions v and q on Γ. The rest of steps are specific to TraceFEM [79]. For further implementation detail, we refer to [110]. For temporal discretization, we use a semi-implicit stabilized Euler method [94] and an adaptive time stepping technique as in [40]. The finite element approximations c_h and μ_h are available at time $t_n \in [0, t^{final}]$. The time step $\delta t = t_n - t_{n-1}$ adaptively varies from $2.5 \cdot 10^{-5}$ at the initial phase of spinodal decomposition to 10^3 when the process is close to equilibrium. We apply GMRES iterative procedure with a block preconditioner to solve the discretized system.

Note that the finite element solution still satisfies mass conservation, i.e.

$$\int_\Gamma c_h(\mathbf{x}, t_n) \; ds = \int_\Gamma c_h(\mathbf{x}, t_{n-1}) \; ds \text{ for all n=1,...,N,} \tag{286}$$

which implies,

$$\frac{\int_{\Gamma_h} c_h(\mathbf{x}, t_n) \; ds}{\int_{\Gamma_h} 1 \; ds} \approx a_{raft} \text{ for all n=1,...,N.} \tag{287}$$

An important quantity about the dynamics of the membrane structure is the total perimeter of the rafts over time. We denote it as p_{raft}. A good approximation of p_{raft} is given by,

$$p_{raft}(t_n) \approx p_0 \int_{\Gamma_h} \epsilon \|\nabla_\Gamma c_h(\mathbf{x}, t_n)\|_1^2 \; ds \tag{288}$$

where p_0 is a calibration constant satisfies $p_0 \int_{\Gamma_h} \epsilon \|\nabla_\Gamma c_{ref}\|_1^2 \; ds = 2\pi$. c_{ref} is an order parameter for the reference configuration, when the north semisphere of Γ is in phase 1.

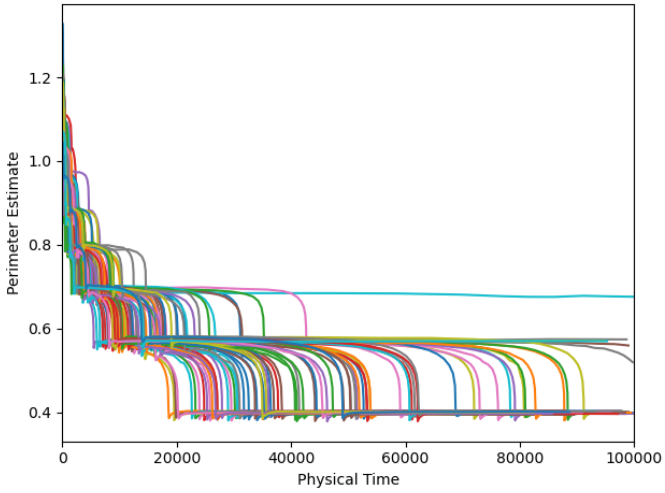

Figure 18: Results of p_{raft} over time for the initial condition (287) from 80 numerical experiments.

Since c_o is initialized randomly, this will result in different dynamics of phase separation in each numerical simulation. We can observe this in the plot of the total raft perimeter estimate over time from different numerical simulations. Figure 18 depicts up to 80 numerical simulation results of perimeter estimate p_{raft} for the initial condition (287).

4.2 Recurrent neural network

In the past few years, various machine learning methods have been investigated for complex dynamic system simulation or prediction [66, 82, 62]. Recent studies have shown promising results in using artificial neural networks to build data-driven parametrization for modeling turbulence and dynamical systems. Among all the sequential model approaches for predicting time series, the artificial neural networks (ANNs) [86, 88, 92], recurrent neural networks (RNNs) [69, 63, 103, 109, 111, 66, 103, 57], and gated recurrent units (GRU) [107, 30] are most popular ones.

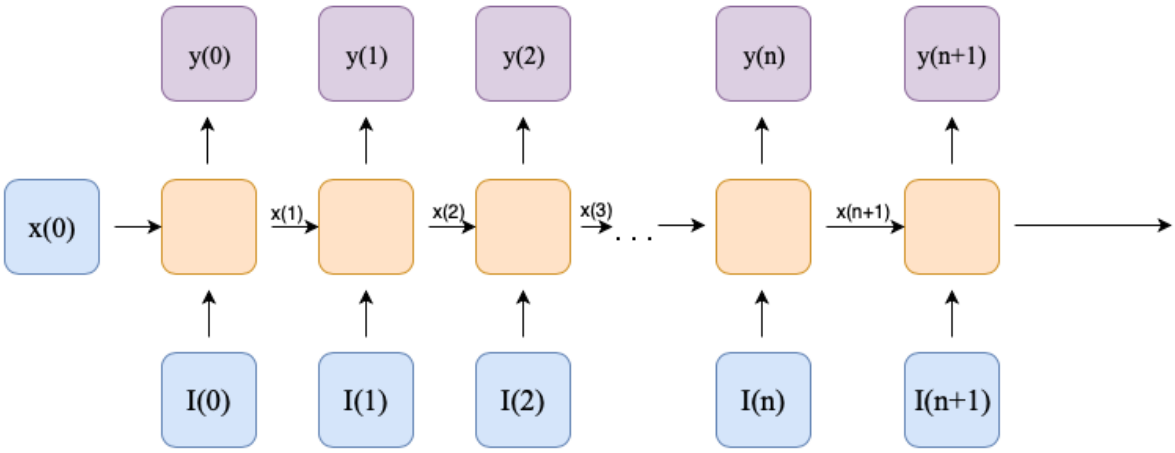

Figure 19: Architecture of a traditional RNN.

Recurrent neural networks (RNNs) [67] are a class of artificial neural networks [108]. The difference between recurrent neural network and other neural networks are its connection between nodes form a directed or undirected graph along a temporal sequence. This allows RNNs to use their internal state to process sequences of inputs, which allows RNN to exhibit temporal dynamic behavior, see Figure (19), where $\mathbf{I}(t), \mathbf{x}(t), \mathbf{y}(t)$ are input, internal state, and output for each time step t. Inspired by several recent studies [25, 103, 20], in which the authors reported their Long Short-Term Memory (RNN-LSTM) and Echo State Network (RC-ESN) have shown promising results in data-driven prediction of the spatio-temporal evolution of several chaotic models such as the Lorenz system. Our goal is to build on these pioneering studies, investigate and compare the performance of ESN, LSTM side by side in predicting several statistics that characterize the surface Cahn-Hilliard system.

4.2.1 Echo State Network Architecture

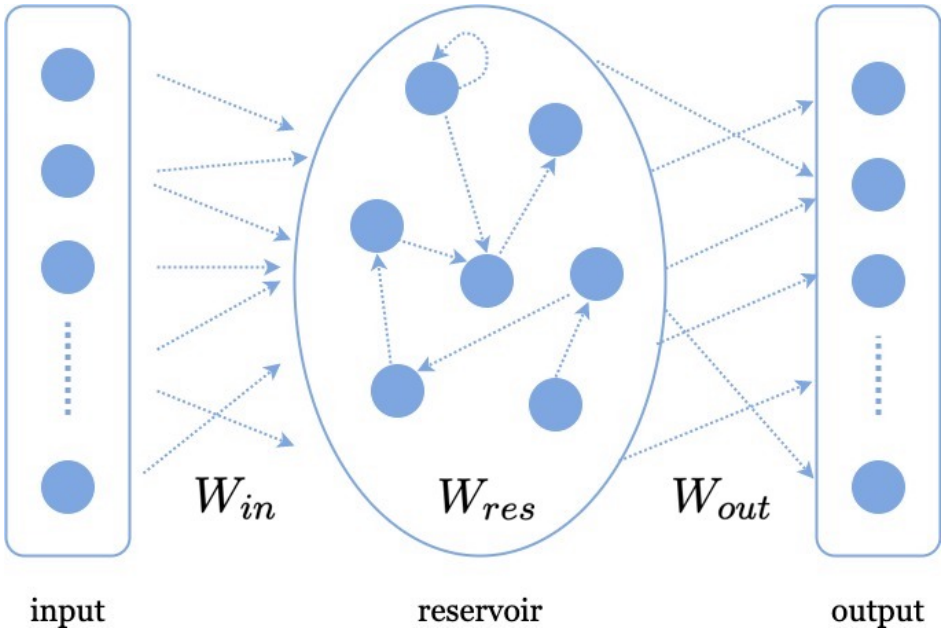

Figure 20: The architecture of an Echo State Network.

We briefly introduce the Echo State Network [64]. ESN is a simple type of RNN which consists of three layers namely, the input layer, the recurrent layer (the reservoir) which contains a large number of sparsely connected neurons, and the output layer, see Figure 20. The connection weights of the input layer W_{in} and the reservoir layer W_{res} are fixed after initialization, the output weights W_{out} are trainable and can be obtained by solving a linear regression problem.

Consider a D dimensional time series $\mathbf{I}(t) \in \mathbb{R}^D$, and $\mathbf{x}(t) \in \mathbb{R}^M$ denote the state of the reservoir at time t, where M is a given positive integer representing the size of the recurrent layer. We use $\mathbf{y}(t) \in \mathbb{R}^D$ to denote the output value of ESN. $W_{in} \in \mathbb{R}^{M \times D}$ represents the connection weights between input layer and recurrent layer, $W_{res} \in \mathbb{R}^{M \times M}$ denotes the connection weights in recurrent layer, $W_{out} \in \mathbb{R}^{D \times M}$ denotes the connection weights between recurrent layer and output layer see

Figure 20. Define the state transition equations:

$$\mathbf{x}(t) = f(W_{in}\mathbf{I}(t) + W_{res}\mathbf{x}(t-1)), \tag{289}$$

$$\mathbf{y}(t) = W_{out}\mathbf{x}(t) \tag{290}$$

where f is a nonlinear map. In this study, f is chosen as,

$$f : \begin{bmatrix} v_1 \\ v_2 \\ v_3 \\ v_4 \\ \vdots \end{bmatrix} \rightarrow \begin{bmatrix} tanh(v_1) \\ tanh^2(v_2) \\ tanh(v_3) \\ tanh^2(v_4) \\ \vdots \end{bmatrix} \tag{291}$$

We use $tanh$ for odd indices elements and $tanh^2$ for even indices elements [83, 20]. The read-out weights W_{out} can be obtained by solving the following least-squares problem,

$$\min_{W_{out} \in \mathbb{R}^{D \times M}} ||W_{out}X - Y||_2^2, \tag{292}$$

$$W_{out} = YX^{-1} \tag{293}$$

where $Y := [\hat{y}(0), \hat{y}(1), ...\hat{y}(T)]$ and $\hat{y}(t)$ denote the desire output, and $X := [\mathbf{x}(0), \mathbf{x}(1), ...\mathbf{x}(T)]$. Before the training phase, there are three main hyper-parameters that need to be initialized:

- w^{in} is an input-scaling parameter. The elements in W_{in} are commonly randomly initialized from a uniform distribution in $[-w^{in}, w^{in}]$.
- α is the sparsity parameter of W_{res} which denotes the proportion of non-zero elements.
- $\rho(W_{res})$ is the spectral radius of W_{res}

Suppose part of time series $\{\mathbf{I}(t), t \in \{0, 1, 2, ...t_0\}\}$ are given and we want to predict the next N steps of $\mathbf{I}(t)$. $\{\hat{I}(t), t \in \{t_0 + 1, ..., t_0 + N\}\}$ denote the prediction from ESN for the next N steps

of $\mathbf{I}(t)$. The prediction procedure is described below,

Algorithm 1 ESN Predicting Procedure

1: $\mathbf{x}(0) := \mathbf{0}, i = 1,$

2: Compute $\mathbf{x}(t_0)$ and $\mathbf{y}(t_0)$ from system (289) and (290),

3: **while** $i \leq N$ **do**

4: $\hat{I}(t_0 + i) := \mathbf{y}(t_0 + i - 1)$

5: Compute $\mathbf{x}(t_0 + i)$ and $\mathbf{y}(t_0 + i)$ by using $\hat{I}(t_0 + i)$ and $\mathbf{x}(t_0 + i - 1)$ as input to the system (289) and (290) .

6: i=i+1

7: **end while**

4.2.2 LSTM Network Architecture

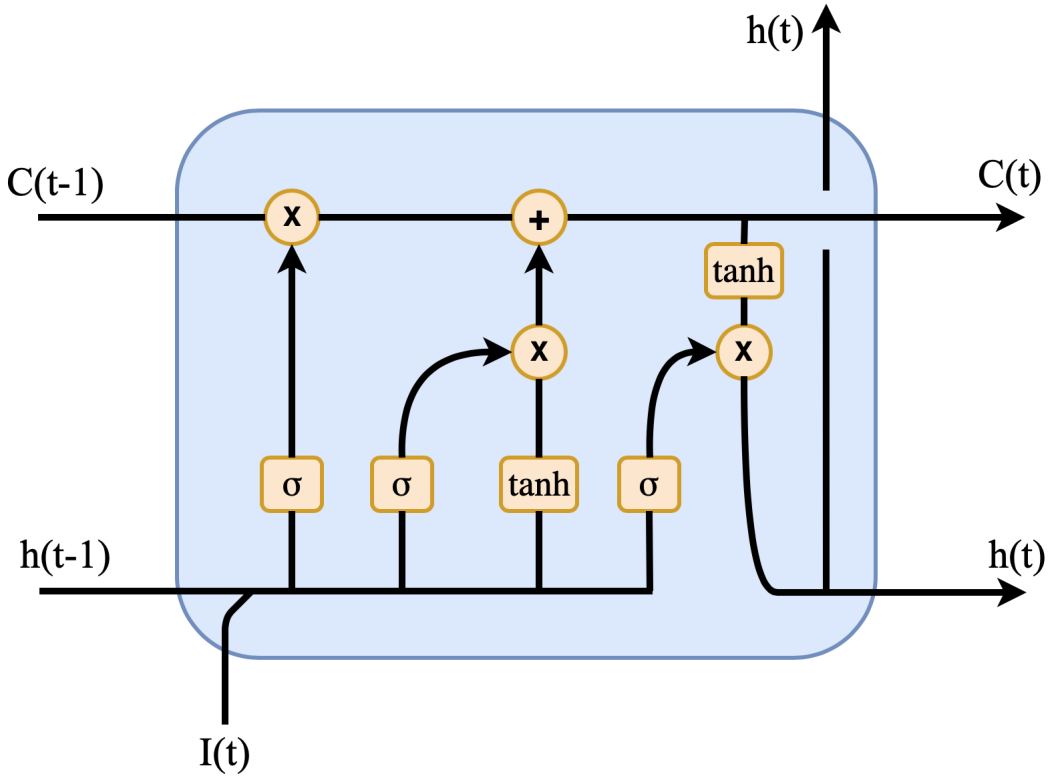

Figure 21: Architecture of LSTM.

Long-Short Term Memory networks (LSTM) [48] is another popular RNN architecture, see Figure 21. LSTM is most suited for predicting sequential data, for example, time series. In recent years, LSTM received attention due to its excellent performance and potential in time series modelings such as supply chain, stock pricing, language processing, and speech recognition. The major difference between LSTM and other RNN architectures is that LSTM networks have gates that control the information flow into the neural network from previous steps of the time series. A gate in a neural networks usually acts as a threshold for helping the neural network to distinguish between using normal stacked layers and using an identity connection. The major advantage of

adding gates to the structure is that it successfully overcomes the difficulty of vanishing and exploding gradients during the backpropagation training procedure in traditional RNN architecture. We use $D_i,\ D_f$ and D_h to denote the dimension of the input gate, the forget gate, hidden layers. $g^i(t)$, $g^i(t)$ and $g^i(t) \in \mathbb{R}^{D_h \times (D_h + D_i)}$ are the input gate, forget gate and output gate. $\mathbf{I}(t)$ is the input of multi-dimensional time series at time t. $C(t)$ is the cell state. $\mathbf{W}_i,\ \mathbf{W}_f,\ \mathbf{W}_o,\ \mathbf{W}_c$ and $\mathbf{W}_{oh}$ are trainable weights. The governing equations for LSTM networks:

$$g^f(t) = \sigma_f(\mathbf{W}_f[h(t-1), \mathbf{I}(t)] + b_f), \tag{294}$$

$$g^i(t) = \sigma_i(\mathbf{W}_i[h(t-1), \mathbf{I}(t)] + b_i), \tag{295}$$

$$\tilde{C}(t) = tanh(\mathbf{W}_c[h(t-1), \mathbf{I}(t)] + b_h), \tag{296}$$

$$C(t) = g^f(t)C(t-1) + g^i(t)\tilde{C}(t), \tag{297}$$

$$g^o(t) = \sigma_h(\mathbf{W}_h[h(t-1), \mathbf{I}(t)] + b_h), \tag{298}$$

$$h(t) = g^i(t)tanh(C(t)), \tag{299}$$

$$\phi(t) = \mathbf{W}_{oh}h(t), \tag{300}$$

$$\mathbf{X}(t + \delta t) \approx \phi(t) \tag{301}$$

where $\sigma_f, \sigma_i, \sigma_h$ are the softmax functions. The LSTM we used in this chapter has 50 hidden layers in each cell. We use BPTT algorithm [34] with ADAM optimizer to tune the parameters in our experiments.

4.3 Training and testing dataset

Three datasets are generated using the numerical simulations with the finite element method described in Sec. 4.1 with initial condition (283). We generate the total of 80 observations of total perimeter of rafts, number of rafts, Helmoholtz free energy over time with different initial distributions. We assign the results of experiment $No.1 - No.65$ to the training set, the results of experiment $No.66 - No.70$ to the validation set, the results of experiment $No.70 - No.80$ to the

testing set. Recall the definition of the Helmoholtz free energy $f(c) = \frac{1}{\epsilon} f_0(c) + \frac{\epsilon}{2} |\nabla_\Gamma c|^2$. We present 80 numerical results of number of rafts, Helmoholtz free energy, and total perimeter of rafts over time in Figures (22)-(23),

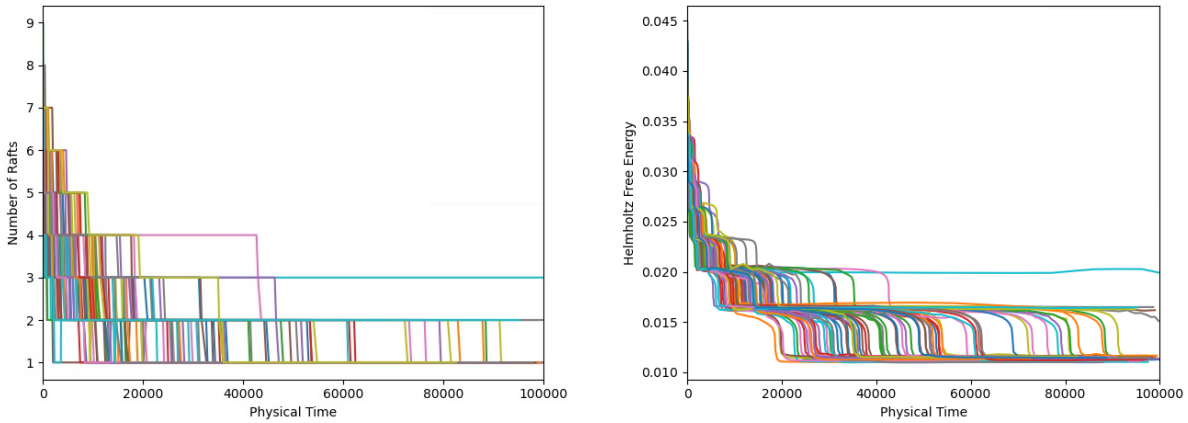

Figure 22: Results of $f(c)$ and the number of rafts over time for the initial condition (287) from 80 numerical experiments.

(22),

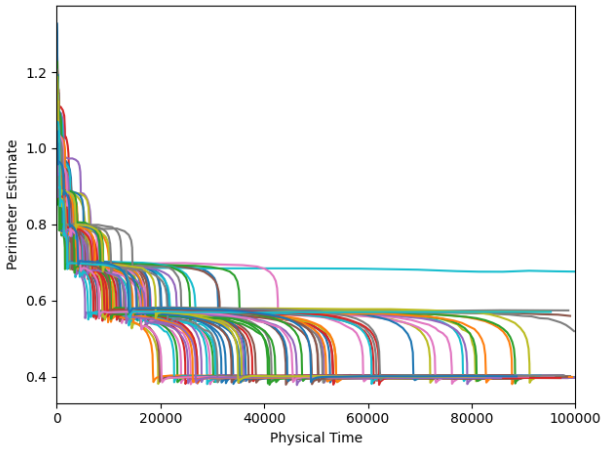

Figure 23: Results of p_{raft} over time for the initial condition (287) from 80 numerical experiments.

For the sake of simplicity, we denote the perimeter curve from experiment $No.1$ as $\{u(t), t \in \{0, 1, ..., N\}\}$, see Figure 24. Consider a smoothed curve generated by averaging $u(t)$, denote it as

$u_s(t)$:

$$u_s(t) := \frac{1}{min\{n,t\}} \sum_{max\{0,t-n\}}^{t} u(t) \tag{302}$$

where n is the width of the averaging window. We denote the remainder as $u_o(t)$,

$$u_o(t) := u(t) - u_s(t). \tag{303}$$

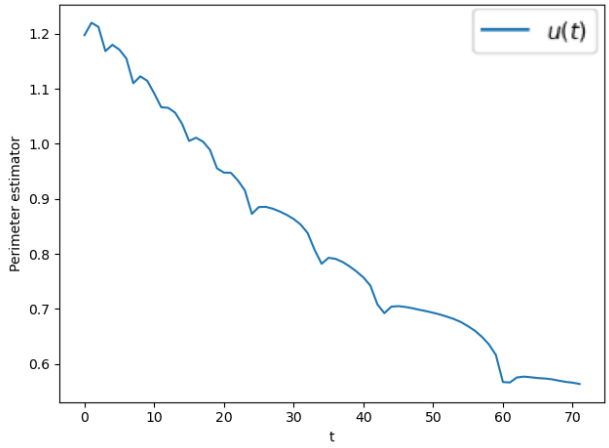

Figure 24: $u(t)$ from experiment $NO.1$ with respect to the number of time steps.

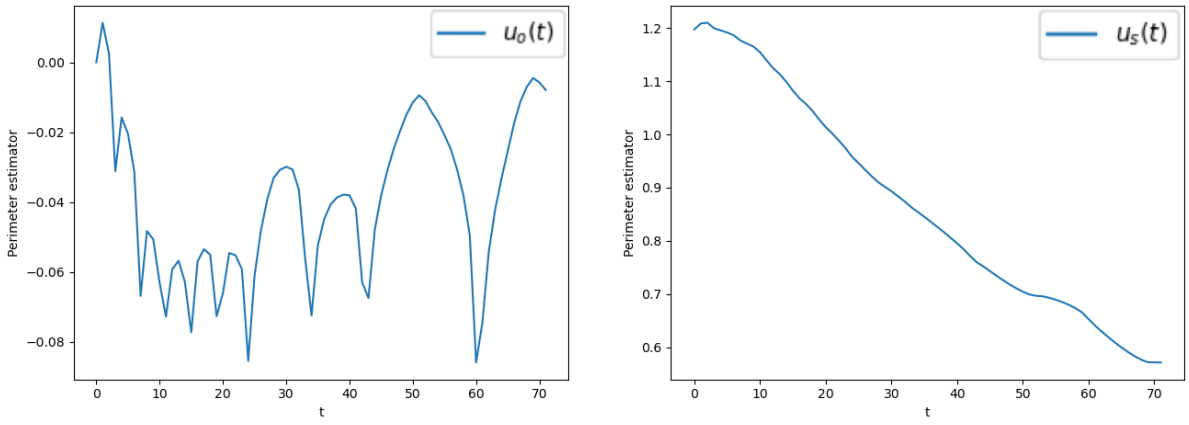

Figure 25: $u_o(t)$ (left), $u_s(t)$ (right) from experiment $NO.1$ with respect to the number of time steps.

Similarly, we process the Helmholtz free energy, the number of rafts. We denote the corresponding smooth and oscillating part by $h_s(t), h_o(t), w_s(t), w_o(t)$. We train two neural networks separately to predict the smoothed curve and the oscillating curve. Define training time series $I_s(t), I_o(t)$:

$$I_s(t) := \begin{bmatrix} u_s(t) \\ h_s(t) \\ w_s(t) \\ sin(\frac{2\pi t}{N}) \end{bmatrix}, \qquad I_o(t) := \begin{bmatrix} u_o(t) \\ h_o(t) \\ w_o(t) \\ sin(\frac{2\pi t}{N}) \end{bmatrix}, \tag{304}$$

where N is the maximum number of time steps from 80 numerical experiments. We concatenate numerical results to construct $I_s(t)$ and $I_o(t)$. Then we train the ESN with $I_s(t), I_o(t)$ for $t \in \{1, ..., 30030\}$, and the LSTM with $I_s(t), I_o(t)$ for $t \in \{1, ..., 500040\}$. Furthermore, we would want the machine to know that the period of the numerical results is N. We can use the $sin(\frac{2\pi t}{N})$ functions. The length of I_s, I_o for training each network are chosen by the post-training performance.

4.4 Prediction of trajectories with different initial distributions

The aim of the prediction results collected in this section is to provide a predicting performance comparison of proposed LSTM and ESN. We restrict our attention to prediction of the total perimeter of rafts over time. To evaluate the overall performance of each network in the testing data set, we define an averaged relative L_1 error,

$$e(t) = \left[\frac{\|I_{true}(t) - I_{pred}(t)\|_1}{\|I_{true}(t)\|_1} \right], \tag{305}$$

where $[\cdot]$ indicates the averaging over 10 experiments with different initial distributions. The input to LSTM is a time-delay-embeded matrix of $\mathbf{I}(t)$ with dimension $q \times D$ [54]. To gain the best predicting performance from LSTM, one needs to input the previous q steps of $\mathbf{I}(t)$, i.e. $\{\mathbf{I}(t-(q-1)\delta t), ..., \mathbf{I}(t)\}$ to predict $\mathbf{I}(t+\delta t)$. The input of ESN only requires $\mathbf{I}(t)$ and inner state $\mathbf{x}(t)$ to predict $\mathbf{I}(t+\delta t)$. Predicting results and an averaged error are presented in Figure 26-31. Only the LSTM result for oscillating trajectories is reported, as the ESN does not perform very well in predicting oscillating trajectories. The hyper parameters in (289)-(290) are chosen as: reservoir size $D = 10$, input radius $w_{in} = 0.35$, sparsity parameter $\alpha = 0.05$, and spectral radius of W_{res} $\rho = 0.35$.

For the LSTM parameters in (294)-(301), we set $q = 3,\ D_h = 50,\ D_i = (4 \times q)$. The prediction skills of the two neural networks for the same training/testing sets are compared in Figures 26-31.

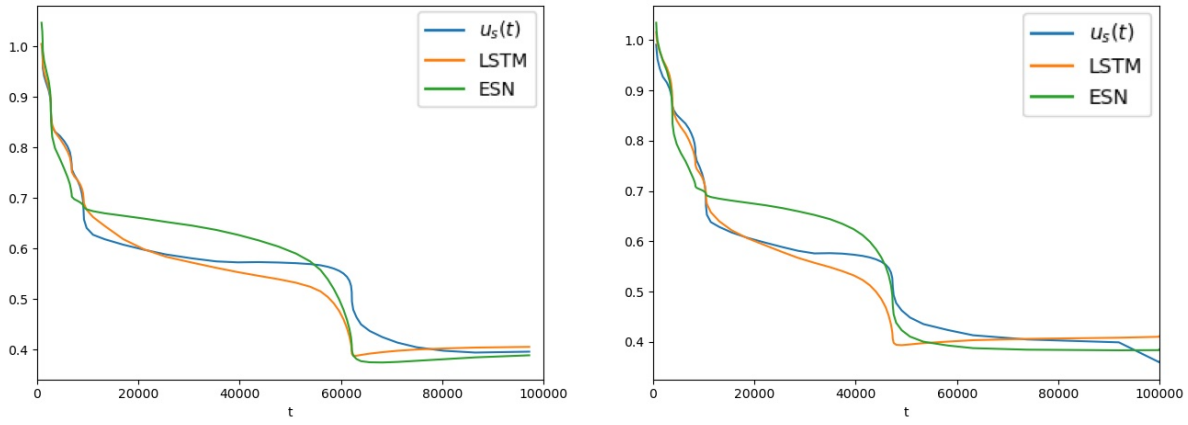

Figure 26: Comparison of the prediction skills over $u_s(t)$ among the two deep learning methods. The lines show ground truth (blue), LSTM (orange), ESN (green). Left and right plots show examples where ESN and LSTM yields respectively the best and the worst prediction with respect to the relative L_1 error.

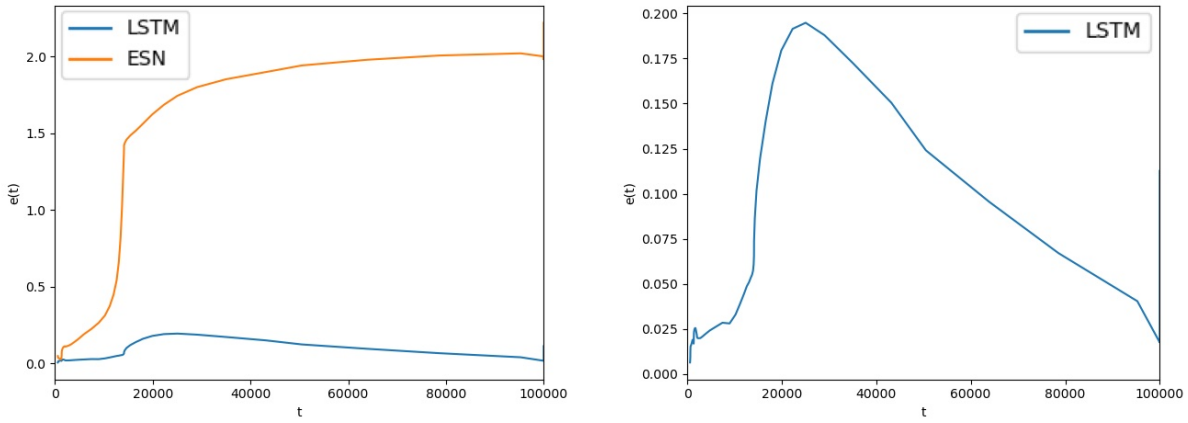

Figure 27: Average relative L_1 error of LSTM (blue) and ESN (orange) over 10 trajectories in the testing set (left), averaged relative L_1 error of LSTM over 10 trajectories in the testing set (right).

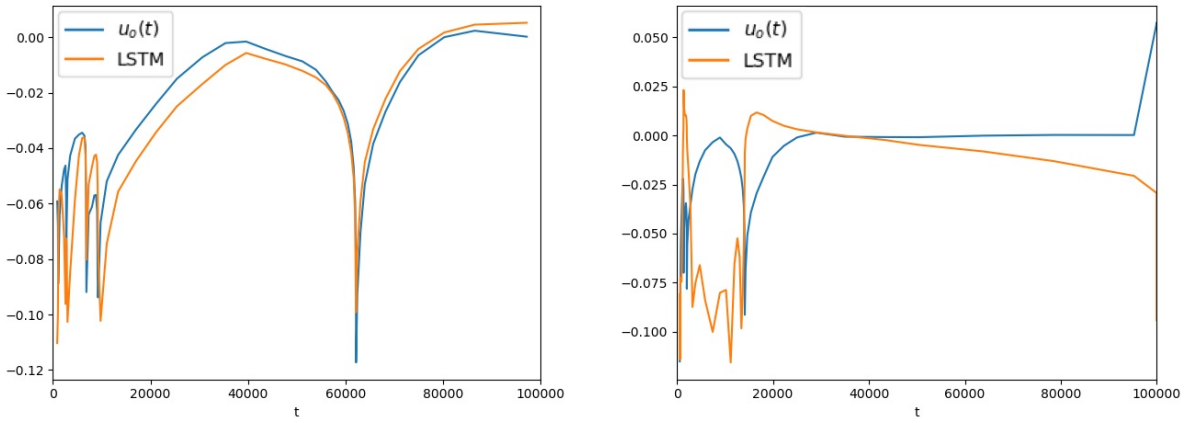

Figure 28: LSTM prediction of $u_o(t)$. The lines show ground truth (blue), LSTM (orange). left and right plots show examples where the LSTM yields respectively the best and the worst prediction with respect to the relative L_1 error.

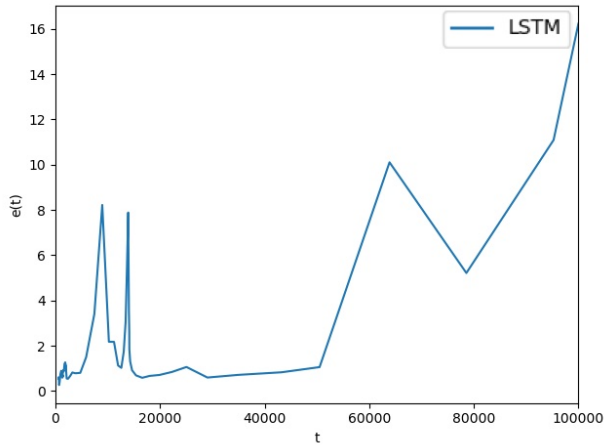

Figure 29: Averaged relative L_1 error over 10 trajectories in testing set.

We combine the prediction from LSTM for the oscillating curves and the prediction from ESN, LSTM for the smoothed curves.

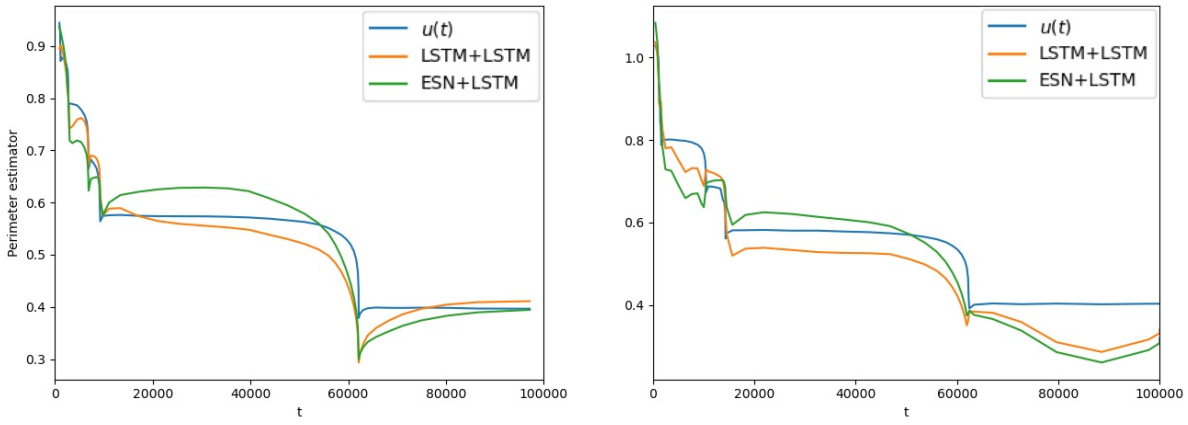

Figure 30: Left and right plots show examples where ESN+LSTM and LSTM+LSTM yield respectively the best and the worst prediction with respect to the relative L_1 error.

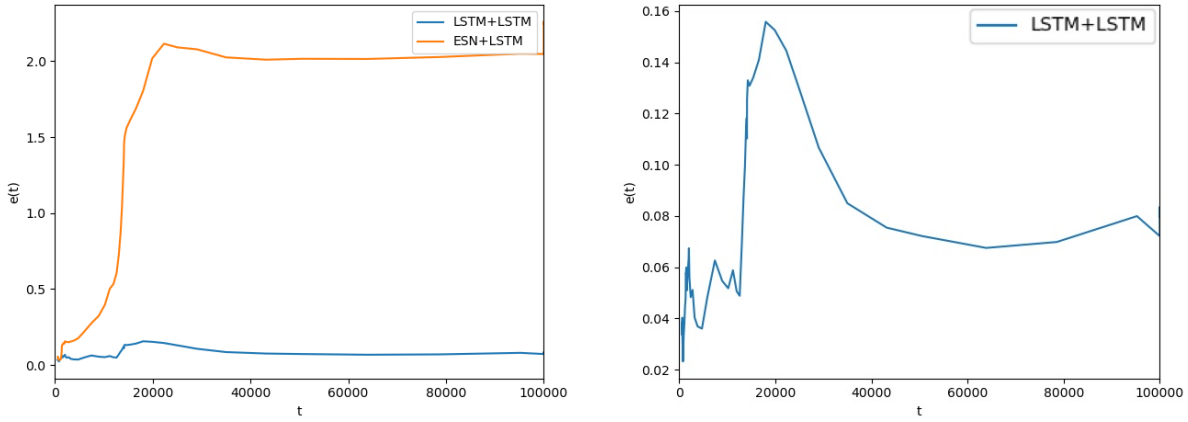

Figure 31: Averaged relative L_1 error of LSTM+LSTM (blue) and ESN+LSTM (orange) over 10 trajectories in testing set (left), averaged relative L_1 error of LSTM+LSTM over 10 trajectories in testing set (right).

From Figures 26 - 31, we conclude that LSTM+LSTM significantly outperformed ESN+LSTM with higher prediction accuracy averaged $e(t) < 0.16, t \in [0, 100000]$. Figure 31 (right) further demonstrates the capabilities of LSTM for short-term spatio-temporal predictions, with averaged $e(t) < 0.08$, for $t \in [0, 13000]$.

In this chapter, we investigated the application of the ESN and LSTM to learning and predicting

total perimeter of rafts over time which characterizes the dynamics governed by the Cahn-Hilliard equations. Our training dataset consists of numerical solutions with different initial distributions. We demonstrated in this chapter that the plain LSTM+LSTM has a high utility of prediction for solutions consistent with the training data, i.e. for solutions with the same initial statistical distributions.

Bibliography

[1] Adjerid, S., Chaabane, N., Lin, T.: An immersed discontinuous finite element method for Stokes interface problems. Computer Methods in Applied Mechanics and Engineering **293**, 170 – 190 (2015). DOI https://doi.org/10.1016/j.cma.2015.04.006. URL http://www.sciencedirect.com/science/article/pii/S004578251500153X

[2] Anderson, D.M., McFadden, G.B., Wheeler, A.A.: Diffuse-interface methods in fluid mechanics. Annual Review of Fluid Mechanics **30**(1), 139–165 (1998)

[3] Basting, S., Quaini, A., Canic, S., Glowinski, R.: Extended ALE method for fluid-structure interaction problems with large structural displacements. Journal of Computational Physics **331**, 312 – 336 (2017). DOI https://doi.org/10.1016/j.jcp.2016.11.043. URL http://www.sciencedirect.com/science/article/pii/S0021999116306350

[4] Basting, S., Weismann, M.: A hybrid level set/front tracking approach for finite element simulations of two-phase flows. Journal of Computational and Applied Mathematics **270**, 471–483 (2014). DOI http://dx.doi.org/10.1016/j.cam.2013.12.014. URL http://www.sciencedirect.com/science/article/pii/S0377042713006870

[5] Bercovier, M., Pironneau, O.: Error estimates for finite element method solution of the Stokes problem in the primitive variables. Numerische Mathematik **33**(2), 211–224 (1979)

[6] Bernardi, C., Canuto, C., Maday, Y.: Generalized inf-sup conditions for Chebyshev spectral approximation of the Stokes problem. SIAM Journal on Numerical Analysis **25**(6), 1237–1271 (1988)

[7] Bocquet, L., Barrat, J.L.: Flow boundary conditions from nano-to micro-scales. Soft matter **3**(6), 685–693 (2007)

[8] Bogovskii, M.E.: Solution of the first boundary value problem for the equation of continuity of an incompressible medium. In: Doklady Akademii Nauk, vol. 248, pp. 1037–1040. Russian Academy of Sciences (1979)

[9] Bolton, T., Zanna, L.: Applications of deep learning to ocean data inference and subgrid parameterisation. Journal of Advances in Modeling Earth Systems **11** (2019). DOI 10.1029/2018MS001472

[10] Bootland, N., Bentley, A., Kees, C., Wathen, A.: Preconditioners for two-phase incompressible Navier –Stokes flow. SIAM Journal on Scientific Computing **41**(4), B843–B869 (2019)

[11] Bordas, S., Burman, E., Larson, M., M. A. Olshanskii, e.: Geometrically Unfitted Finite Element Methods and Applications, vol. Lecture Notes in Computational Science and Engineering 121. Springer, Berlin (2018)

[12] Brenner, S.C.: Korn's inequalities for piecewise H1 vector fields. Mathematics of Computation pp. 1067–1087 (2004)

[13] Brunton, S.L., Kutz, J.N.: Data-Driven Science and Engineering: Machine Learning, Dynamical Systems, and Control. Cambridge University Press (2019). DOI 10.1017/9781108380690

[14] Burman, E.: Ghost penalty. C. R. Math. Acad. Sci. Paris **348**(21-22), 1217–1220 (2010). URL https://doi.org/10.1016/j.crma.2010.10.006

[15] Burman, E., Claus, S., Hansbo, P., Larson, M.G., Massing, A.: Cutfem: Discretizing geometry and partial differential equations. International Journal for Numerical Methods in Engineering **104**(7), 472–501 (2015)

[16] Burman, E., Delay, G., Ern, A.: An unfitted hybrid high-order method for the Stokes interface problem. hal-02519896v3 (2020)

[17] Cáceres, E., Guzmán, J., Olshanskii, M.: New stability estimates for an unfitted finite element method for two-phase Stokes problem. SIAM Journal on Numerical Analysis **58**(4), 2165–2192 (2020)

[18] Cahn, J.W.: On spinodal decomposition. Acta metallurgica **9**(9), 795–801 (1961)

[19] Cahn, J.W., Hilliard, J.E.: Free energy of a nonuniform system. i. interfacial free energy. The Journal of chemical physics **28**(2), 258–267 (1958)

[20] Chattopadhyay, A., Hassanzadeh, P., Subramanian, D.: Data-driven predictions of a multiscale lorenz 96 chaotic system using machine-learning methods: reservoir computing, artificial neural network, and long short-term memory network. Nonlinear Processes in Geophysics **27**(3), 373–389 (2020). DOI 10.5194/npg-27-373-2020. URL https://npg.copernicus.org/articles/27/373/2020/

[21] Chessa, J., Belytschko, T.: An extended finite element method for two-phase fluids. ASME Journal of Applied Mechanics **70**, 10–17 (2003)

[22] Claus, S., Kerfriden, P.: A cutfem method for two-phase flow problems. Computer Methods in Applied Mechanics and Engineering **348**, 185 – 206 (2019). DOI https://doi.org/10.1016/j.cma.2019.01.009. URL http://www.sciencedirect.com/science/article/pii/S0045782519300131

[23] Cooley, M., O'neill, M.: On the slow motion generated in a viscous fluid by the approach of a sphere to a plane wall or stationary sphere. Mathematika **16**(1), 37–49 (1969)

[24] Donea, J., Huerta, A., Ponthot, J.P., Rodríguez-Ferran, A.: Arbitrary Lagrangian–Eulerian Methods, chap. 14. John Wiley & Sons Ltd., (2004)

[25] Dueben, P.D., Bauer, P.: Challenges and design choices for global weather and climate models based on machine learning. Geoscientific Model Development **11**(10), 3999–4009 (2018)

[26] Duraisamy, K., Iaccarino, G., Xiao, H.: Turbulence modeling in the age of data. Annual Review of Fluid Mechanics **51**(1), 357–377 (2019). DOI 10.1146/annurev-fluid-010518-040547. URL https://doi.org/10.1146/annurev-fluid-010518-040547

[27] Ern, A., Guermond, J.L.: Theory and practice of finite elements, vol. 159. Springer, New York (2013)

[28] Frachon, T., Zahedi, S.: A cut finite element method for incompressible two-phase Navier –Stokes flows. Journal of Computational Physics **384**, 77 – 98 (2019). DOI https://doi.org/10.1016/j.jcp.2019.01.028. URL http://www.sciencedirect.com/science/article/pii/S0021999119300798

[29] Fries, T.P.: The intrinsic XFEM for two-fluid flows. International Journal for Numerical Methods in Fluids **60**(4), 437–471 (2009)

[30] Gagne, D.J., Christensen, H.M., Subramanian, A.C., Monahan, A.H.: Machine learning for stochastic parameterization: Generative adversarial networks in the lorenz '96 model. Journal of Advances in Modeling Earth Systems **12**(3) (2020). DOI 10.1029/2019ms001896. URL http://dx.doi.org/10.1029/2019MS001896

[31] Ganesan, S., Matthies, G., Tobiska, L.: On spurious velocities in incompressible flow problems with interfaces. Preprint 05-35, Department of Mathematics, University of Magdeburg (2005)

[32] Gentine, P., Pritchard, M., Rasp, S., Reinaudi, G., Yacalis, G.: Could machine learning break the convection parameterization deadlock? Geophysical Research Letters **45**(11), 5742–5751 (2018). DOI https://doi.org/10.1029/2018GL078202. URL https://agupubs.onlinelibrary.wiley.com/doi/abs/10.1029/2018GL078202

[33] Gérard-Varet, D., Hillairet, M., Wang, C.: The influence of boundary conditions on the contact problem in a 3d navier –stokes flow. Journal de Mathématiques Pures et Appliquées **103**(1), 1–38 (2015)

[34] Goodfellow, I., Bengio, Y., Courville, A.: Deep learning. MIT press (2016)

[35] Grande, J., Lehrenfeld, C., Reusken, A.: Analysis of a high-order trace finite element method for pdes on level set surfaces. SIAM Journal on Numerical Analysis **56**(1), 228–255 (2018)

[36] Groß, S., Reichelt, V., Reusken, A.: A finite element based level set method for two-phase incompressible flows. Comp. Visual. Sci. **9**, 239–257 (2006)

[37] Gross, S., Reusken, A.: Numerical methods for two-phase incompressible flows, vol. 40. Springer Science & Business Media (2011)

[38] Gurtin, M.E., Murdoch, A.I.: A continuum theory of elastic material surfaces. Archive for Rational Mechanics and Analysis **57**(4), 291–323 (1975)

[39] Guzmán, J., Olshanskii, M.: Inf-sup stability of geometrically unfitted Stokes finite elements. Mathematics of Computation **87**(313), 2091–2112 (2018)

[40] Gómez, H., Calo, V.M., Bazilevs, Y., Hughes, T.J.: Isogeometric analysis of the cahn–hilliard phase-field model. Computer Methods in Applied Mechanics and Engineering **197**(49), 4333–4352 (2008). DOI https://doi.org/10.1016/j.cma.2008.05.003. URL https://www.sciencedirect.com/science/article/pii/S0045782508001953

[41] Hansbo, A., Hansbo, P.: An unfitted finite element method, based on Nitsche's method, for elliptic interface problems. Comput. Methods Appl. Mech. Engrg. **191**, 5537–5552 (2002)

[42] Hansbo, P., Larson, M., Massing, A.: A stabilized cut finite element method for the darcy problem on surfaces. Computer Methods in Applied Mechanics and Engineering **326**, 298 – 318 (2017). DOI https://doi.org/10.1016/j.cma.2017.08.007. URL http://www.sciencedirect.com/science/article/pii/S0045782517301548

[43] Hansbo, P., Larson, M.G., Larsson, K.: Analysis of finite element methods for vector laplacians on surfaces. IMA Journal of Numerical Analysis **40**(3), 1652–1701 (2020)

[44] Hansbo, P., Larson, M.G., Zahedi, S.: A cut finite element method for a Stokes interface problem. Applied Numerical Mathematics **85**, 90 – 114 (2014). DOI https://doi.org/10.1016/j.apnum.2014.06.009. URL http://www.sciencedirect.com/science/article/pii/S0168927414001184

[45] Hapanowicz, J.: Slip between the phases in two-phase water–oil flow in a horizontal pipe. International Journal of Multiphase Flow **34**(6), 559 – 566 (2008). DOI https://doi.org/10.1016/j.ijmultiphaseflow.2007.12.002. URL http://www.sciencedirect.com/science/article/pii/S0301932208000062

[46] Hashemi, M.R., Ryzhakov, P.B., Rossi, R.: An enriched finite element/level-set method for simulating two-phase incompressible fluid flows with surface tension. Computer Methods in Applied Mechanics and Engineering **370**, 113,277 (2020). DOI https://doi.org/10.1016/j.cma.2020.113277. URL http://www.sciencedirect.com/science/article/pii/S004578252030462X

[47] He, X., Song, F., Deng, W.: Stabilized nonconforming Nitsche's extended finite element method for Stokes interface problems. https://arxiv.org/abs/1905.04844 (2019)

[48] Hochreiter, S., Schmidhuber, J.: Long Short-Term Memory. Neural Computation **9**(8), 1735–1780 (1997). DOI 10.1162/neco.1997.9.8.1735. URL https://doi.org/10.1162/neco.1997.9.8.1735

[49] Hocking, L.M.: The effect of slip on the motion of a sphere close to a wall and of two adjacent spheres. Journal of Engineering Mathematics **7**(3), 207–221 (1973)

[50] Jacqmin, D.: Calculation of Two-Phase Navier -Stokes Flows Using Phase-Field Modeling. Journal of Computational Physics **155**(1), 96–127 (1999). DOI 10.1006/jcph.1999.6332

[51] Jankuhn, T., Olshanskii, M.A., Reusken, A.: Incompressible fluid problems on embedded surfaces: Modeling and variational formulations. Interfaces and Free Boundaries **20**(3), 353–377 (2018)

[52] Jankuhn, T., Olshanskii, M.A., Reusken, A., Zhiliakov, A.: Error analysis of higher order trace finite element methods for the surface Stokes equation. Journal of Numerical Mathematics (ahead-of-print) (2021). DOI 10.1515/jnma-2020-0017

[53] John, V.: Slip with friction and penetration with resistance boundary conditions for the Navier –Stokes equations—numerical tests and aspects of the implementation. Journal of Computational and Applied Mathematics **147**(2), 287–300 (2002)

[54] Kim, H., Eykholt, R., Salas, J.: Nonlinear dynamics, delay times, and embedding windows. Physica D: Nonlinear Phenomena **127**(1), 48–60 (1999). DOI https://doi.org/10.1016/S0167-2789(98)00240-1. URL https://www.sciencedirect.com/science/article/pii/S0167278998002401

[55] Kirchhart, M., Gross, S., Reusken, A.: Analysis of an XFEM discretization for Stokes interface problems. SIAM Journal on Scientific Computing **38**(2), A1019–A1043 (2016)

[56] Kutz, J.N.: Deep learning in fluid dynamics. Journal of Fluid Mechanics **814**, 1–4 (2017). DOI 10.1017/jfm.2016.803

[57] Lauga, E., Brenner, M., Stone, H.: Microfluidics: The no-slip boundary condition. In: Springer Handbooks, pp. 1219–1240. Springer (2007)

[58] Lehrenfeld, C.: High order unfitted finite element methods on level set domains using isoparametric mappings. Computer Methods in Applied Mechanics and Engineering **300**, 716–733 (2016)

[59] Lehrenfeld, C.: A higher order isoparametric fictitious domain method for level set domains. In: S.P.A. Bordas, E. Burman, M.G. Larson, M.A. Olshanskii (eds.) Geometrically Unfitted Finite Element Methods and Applications, pp. 65–92. Springer International Publishing, Cham (2017)

[60] Lehrenfeld, C., Olshanskii, M.: An Eulerian finite element method for PDEs in time-dependent domains. ESAIM: Mathematical Modelling and Numerical Analysis **53**(2), 585–614 (2019)

[61] Lehrenfeld, C., Reusken, A.: Analysis of a high-order unfitted finite element method for elliptic interface problems. IMA Journal of Numerical Analysis **38**(3), 1351–1387 (2018)

[62] Ling, J., Kurzawski, A., Templeton, J.: Reynolds averaged turbulence modelling using deep neural networks with embedded invariance. Journal of Fluid Mechanics **807** (2016). DOI 10.1017/jfm.2016.615

[63] Lukoševičius, M., Jaeger, H.: Reservoir computing approaches to recurrent neural network training. Computer Science Review **3**(3), 127–149 (2009). DOI https://doi.org/10.1016/j.cosrev.2009.03.005. URL https://www.sciencedirect.com/science/article/pii/S1574013709000173

[64] Maass, W., Natschläger, T., Markram, H.: Real-Time Computing Without Stable States: A New Framework for Neural Computation Based on Perturbations. Neural Computation **14**(11), 2531–2560 (2002). DOI 10.1162/089976602760407955. URL https://doi.org/10.1162/089976602760407955

[65] Massing, A., Larson, M., Logg, A., Rognes, M.: A stabilized Nitsche overlapping mesh method for the Stokes problem. Numer. Math. **128**, 73 – 101 (2014)

[66] McDermott, P.L., Wikle, C.K.: An ensemble quadratic echo state network for non-linear spatio-temporal forecasting. Stat **6**(1), 315–330 (2017). DOI https://doi.org/10.1002/sta4.160. URL https://onlinelibrary.wiley.com/doi/abs/10.1002/sta4.160

[67] Medsker, L.R., Jain, L.: Recurrent neural networks. Design and Applications **5**, 64–67 (2001)

[68] Miura, T.H.: On singular limit equations for incompressible fluids in moving thin domains. Quarterly of Applied Mathematics **76**(2), 215–251 (2018)

[69] Mohan, A., Daniel, D., Chertkov, M., Livescu, D.: Compressed convolutional lstm: An efficient deep learning framework to model high fidelity 3d turbulence (2019)

[70] Moosavi, A., Attia, A., Sandu, A.: A machine learning approach to adaptive covariance localization (2018)

[71] Moës, N., Dolbow, J., Belytschko, T.: A finite element method for crack growth without remeshing. International Journal for Numerical Methods in Engineering **46**(1), 131–150 (1999)

[72] Navier, C.: Mémoire sur les lois du mouvement des fluides. Mémoires de l'Académie Royale des Sciences de l'Institut de France **6**(1823), 389–440 (1823)

[73] Nicolaides, R.A.: Existence, uniqueness and approximation for generalized saddle point problems. SIAM Journal on Numerical Analysis **19**(2), 349–357 (1982)

[74] Olshanskii, M., Quaini, A., Reusken, A., Yushutin, V.: A finite element method for the surface Stokes problem. SIAM Journal on Scientific Computing **40**(4), A2492–A2518 (2018)

[75] Olshanskii, M., Quaini, A., Sun, Q.: An unfitted finite element method for two-phase Stokes problems with slip between phases. arXiv preprint arXiv:2101.09627 (2021)

[76] Olshanskii, M., Quaini, A., Sun, Q.: A finite element method for two-phase flow with material viscous interface. Computational Methods in Applied Mathematics **22**(2), 443–464 (2022). DOI doi:10.1515/cmam-2021-0185. URL https://doi.org/10.1515/cmam-2021-0185

[77] Olshanskii, M., Reusken, A., Zhiliakov, A.: Inf-sup stability of the trace $\mathbf{P}_2$–P_1 taylor–hood elements for surface pdes. Mathematics of Computation (2021). DOI 10.1090/mcom/3551

[78] Olshanskii, M.A., Reusken, A.: Analysis of a Stokes interface problem. Numerische Mathematik **103**, 129–149 (2006)

[79] Olshanskii, M.A., Reusken, A.: Trace finite element methods for PDEs on surfaces. In: Geometrically Unfitted Finite Element Methods and Applications, pp. 211–258. Springer (2017)

[80] Olshanskii, M.A., Safin, D.: Numerical integration over implicitly defined domains for higher order unfitted finite element methods. Lobachevskii Journal of Mathematics **37**, 582–596 (2016)

[81] Olsson, E., Kreiss, G.: A conservative level set method for two phase flow. Journal of Computational Physics **210**(1), 225 – 246 (2005). DOI https://doi.org/10.1016/j.jcp.2005.04.007. URL http://www.sciencedirect.com/science/article/pii/S0021999105002184

[82] Pathak, J., Hunt, B., Girvan, M., Lu, Z., Ott, E.: Model-free prediction of large spatiotemporally chaotic systems from data: A reservoir computing approach. Phys. Rev. Lett. **120**, 024,102 (2018). DOI 10.1103/PhysRevLett.120.024102. URL https://link.aps.org/doi/10.1103/PhysRevLett.120.024102

[83] Pathak, J., Hunt, B., Girvan, M., Lu, Z., Ott, E.: Model-free prediction of large spatiotemporally chaotic systems from data: A reservoir computing approach. Physical Review Letters **120** (2018). DOI 10.1103/PhysRevLett.120.024102

[84] Preuß, J.: Higher order unfitted isoparametric space-time FEM on moving domains. Master's thesis, NAM, University of Göttingen (2018)

[85] Quarteroni, A., Valli, A.: Domain Decomposition Methods for Partial Differential Equations. Oxford Science Publications (1999)

[86] Rasp, S., Pritchard, M.S., Gentine, P.: Deep learning to represent sub-grid processes in climate models (2018)

[87] Rasp, S., Pritchard, M.S., Gentine, P.: Deep learning to represent subgrid processes in climate models. Proceedings of the National Academy of Sciences **115**(39), 9684–9689 (2018). DOI 10.1073/pnas.1810286115. URL https://www.pnas.org/content/115/39/9684

[88] Reichstein, M., Camps-Valls, G., Stevens, B., Jung, M., Denzler, J., Carvalhais, N., Prabhat, M.: Deep learning and process understanding for data-driven earth system science. Nature **566**, 195 (2019). DOI 10.1038/s41586-019-0912-1

[89] Reuther, S., Voigt, A.: Solving the incompressible surface Navier -Stokes equation by surface finite elements. Physics of Fluids **30**(1), 012,107 (2018)

[90] Salbreux, G., Jülicher, F.: Mechanics of active surfaces. Physical Review E **96**(3), 032,404 (2017)

[91] Sauerland, H., Fries, T.P.: The stable XFEM for two-phase flows. Computers & Fluids **87**, 41 – 49 (2013). DOI https://doi.org/10.1016/j.compfluid.2012.10.017. URL http://www.sciencedirect.com/science/article/pii/S0045793012004148. USNCCM Moving Boundaries

[92] Scher, S., Messori, G.: Generalization properties of feed-forward neural networks trained on lorenz systems. Nonlinear Processes in Geophysics **26**, 381–399 (2019). DOI 10.5194/npg-26-381-2019

[93] Schneider, T., Lan, S., Stuart, A., Teixeira, J.: Earth system modeling 2.0: A blueprint for models that learn from observations and targeted high-resolution simulations. Geophysical Research Letters **44**(24), 12,396–12,417 (2017). DOI https://doi.org/10.1002/2017GL076101. URL https://agupubs.onlinelibrary.wiley.com/doi/abs/10.1002/2017GL076101

[94] Shen, J., Yang, X.: Numerical approximations of allen-cahn and cahn-hilliard equations. Discrete & Continuous Dynamical Systems **28**(4), 1669–1691 (2010)

[95] Simons, K., Ikonen, E.: Functional rafts in cell membranes. Nature **387**, 569–72 (1997). DOI 10.1038/42408

[96] Stein, E.M.: Singular integrals and differentiability properties of functions, vol. 2. Princeton university press (1970)

[97] Sussman, M., Smereka, P., Osher, S.: A level set approach for computing solutions to incompressible two-phase flow. Journal of Computational Physics **114**(1), 146 – 159 (1994). DOI https://doi.org/10.1006/jcph.1994.1155. URL http://www.sciencedirect.com/science/article/pii/S0021999184711557

[98] Tanaka, G., Yamane, T., Héroux, J.B., Nakane, R., Kanazawa, N., Takeda, S., Numata, H., Nakano, D., Hirose, A.: Recent advances in physical reservoir computing: A review. Neural Networks **115**, 100–123 (2019). DOI https://doi.org/10.1016/j.neunet.2019.03.005. URL https://www.sciencedirect.com/science/article/pii/S0893608019300784

[99] Toms, B.A., Kashinath, K., Prabhat, Yang, D.: Deep learning for scientific inference from geophysical data: The madden-julian oscillation as a test case. arXiv: Atmospheric and Oceanic Physics (2019)

[100] Unverdi, S.O., Tryggvason, G.: A front-tracking method for viscous, incompressible, multi-fluid flows. Journal of Computational Physics; (United States) **100** (1992). DOI 10.1016/0021-9991(92)90307-K

[101] Veatch, S., Keller, S.: Separation of liquid phases in giant vesicles of ternary mixtures of phospholipids and cholesterol. Biophysical journal **85**, 3074–83 (2003). DOI 10.1016/S0006-3495(03)74726-2

[102] Vlachas, P., Pathak, J., Hunt, B., Sapsis, T., Girvan, M., Ott, E., Koumoutsakos, P.: Backpropagation algorithms and reservoir computing in recurrent neural networks for the forecasting of complex spatiotemporal dynamics. Neural Networks **126**, 191–217 (2020). DOI https://doi.org/10.1016/j.neunet.2020.02.016. URL https://www.sciencedirect.com/science/article/pii/S0893608020300708

[103] Vlachas, P.R., Byeon, W., Wan, Z.Y., Sapsis, T.P., Koumoutsakos, P.: Data-driven forecasting of high-dimensional chaotic systems with long short-term memory networks. Proceedings of the Royal Society A: Mathematical, Physical and Engineering Sciences **474**(2213), 20170,844 (2018). DOI 10.1098/rspa.2017.0844. URL http://dx.doi.org/10.1098/rspa.2017.0844

[104] von Wahl, H., Richter, T., Lehrenfeld, C.: An unfitted Eulerian finite element method for the time-dependent Stokes problem on moving domains. arXiv preprint arXiv:2002.02352 (2020)

[105] Wang, N., Chen, J.: A nonconforming Nitsche's extended finite element method for Stokes interface problems. J Sci Comput **81**, 342–374 (2019)

[106] Wang, Q., Chen, J.: A new unfitted stabilized Nitsche's finite element method for Stokes interface problems. Computers & Mathematics with Applications **70**(5), 820 – 834 (2015). DOI https://doi.org/10.1016/j.camwa.2015.05.024. URL http://www.sciencedirect.com/science/article/pii/S0898122115002692

[107] Wu, J.L., Kashinath, K., Albert, A., Chirila, D., Prabhat, Xiao, H.: Enforcing statistical constraints in generative adversarial networks for modeling chaotic dynamical systems. Journal of Computational Physics **406**, 109,209 (2020). DOI 10.1016/j.jcp.2019.109209. URL http://dx.doi.org/10.1016/j.jcp.2019.109209

[108] Yegnanarayana, B.: Artificial neural networks. PHI Learning Pvt. Ltd. (2009)

[109] Yu, R., Zheng, S., Anandkumar, A., Yue, Y.: Long-term forecasting using higher order tensor rnns (2019)

[110] Yushutin, V., Quaini, A., Majd, S., Olshanskii, M.: A computational study of lateral phase separation in biological membranes. International Journal for Numerical Methods in Biomedical Engineering **35**, e3181 (2019). DOI 10.1002/cnm.3181

[111] Zimmermann, R.S., Parlitz, U.: Observing spatio-temporal dynamics of excitable media using reservoir computing. Chaos **28 4**, 043,118 (2018)